



**UNIVERSIDAD DE CONCEPCIÓN**  
**DIRECCIÓN DE POSTGRADO**  
**FACULTAD DE CIENCIAS NATURALES Y OCEANOGRÁFICAS**  
**PROGRAMA DE DOCTORADO EN OCEANOGRAFÍA**

**IMPACTO DE LA VARIABILIDAD CLIMÁTICA DURANTE LA**  
**ÚLTIMA DÉCADA SOBRE LA DINÁMICA DEL GIRO SUBTROPICAL**  
**EN EL PACÍFICO SUR ORIENTAL Y EL VOLUMEN DE AGUA**  
**INTERMEDIA DEL PACÍFICO SUR ORIENTAL**

Tesis para optar al grado de Doctor en Oceanografía

**POR: FREDDY EDINSON HERNÁNDEZ VACA**

Profesor Guía: Doctor Wolfgang Schneider

Concepción, julio 2020, Chile

Universidad de Concepción

Dirección de Postgrado

La Tesis de Doctorado en Oceanografía titulada “Impacto de la variabilidad climática durante la última década sobre la dinámica del giro subtropical en el Pacífico Sur Oriental y el volumen de Agua Intermedia del Pacífico Sur Oriental”, del Sr. Freddy Edinson Hernández Vaca y realizada bajo la Facultad de Ciencias Naturales y Oceanográficas, Universidad de Concepción, ha sido aprobada por la siguiente Comisión de Evaluación:

Dr. Wolfgang Schneider  
Profesor Guía  
Universidad de Concepción



Dr. Oscar Pizarro  
Miembro del Comité de Tesis  
Universidad de Concepción

Dr. José Garcés  
Miembro del Comité de Tesis  
Universidad Austral de Chile

Dr. Iván Pérez  
Miembro del Comité de Tesis  
Universidad de los Lagos

Dr. Boris Dewitte  
Evaluador Externo  
Centro de Estudios Avanzados en Zonas Áridas

Dra. Pamela Hidalgo  
Directora  
Programa de Doctorado en Oceanografía  
Universidad de Concepción

## AGRADECIMIENTOS

No tengo evidencia científica, esta tesis la he terminado con la ayuda de Dios, simplemente puedo sentirlo en mi corazón. Gracias a Dios y al Santo de las causas imposibles, San Judas Tadeo.

Al Profesor Wolfgang Schneider, los resultados se ven en el texto, pero hay muchos resultados que no están aquí, las experiencias compartidas, lecciones aprendidas, gratos recuerdos, solo queda decir muchas gracias Wolfgang.

A mi esposa quien decidió valientemente dejar el Ecuador y acompañarme en la travesía de del postgrado. La decisión siempre contó con el respaldo de ella y su apoyo incondicional. Ahora mis hijos son unos jóvenes entienden lo que hago, lo que pasó en su momento, ellos sólo tomaron sus juguetes y juntos hicimos que la estadía en Concepción sea placentera y lo gratificante que era volver a casa y encontrar mi hogar cálido, no sólo por el calor de la estufa, sino más bien por la calidez de la familia formada.

En Concepción, conocí gente linda, podría escribir otra tesis de las anécdotas. En diferentes etapas de la tesis siempre estuvieron compañeros y amigos con los cuales guardo recuerdos especiales por el apoyo permanente e incondicional y gratos momentos compartidos.

En Ecuador mucha familia siempre pendiente y preocupados, les digo ¡Familia hemos culminado. Muchas gracias a todos.

El desarrollo de esta Tesis Doctoral fue posible gracias al contrato de beca No 20090315 entre la Secretaría de Educación Superior, Ciencia, Tecnología e Innovación del Gobierno de la República del Ecuador y el Instituto Oceanográfico de la Armada del Ecuador.

En Ecuador siempre agradecido a las autoridades y colegas del Instituto Oceanográfico y Antártico de la Armada.

## CURRICULUM VITAE

Freddy Edinson Hernández Vaca

Nacido el 16 de julio 1973, en Guayaquil, Ecuador

1991-2006: Oceanógrafo, Escuela Superior Politécnica del Litoral, Ecuador.

2010-2020: Doctor en Oceanografía, Universidad de Concepción, Chile.

### PUBLICACIONES

Schneider W., Pérez-Santos I., Ross L., Bravo L., Seguel R., **Hernández F.**, 2014. On the hydrography of Puyuhuapi Channel, Chilean Patagonia. *Progress in Oceanography* 129: 8-18

**Hernández-Vaca F.**, Schneider W., Garcés-Vargas J., 2017. Contribution of Ekman pumping to the changes in properties and volume of the Eastern South Pacific Intermediate Water. *Gayana* 81(2): 52-63.

Meerhoff E., Yannicelli B., Dewitte B., Díaz-Cabrera E., Vega-Retter C., Ramos M., 5; Bravo L., Concha E., **Hernández-Vaca F.**, y Véliz D., 2018. Asymmetric connectivity of the lobster *Panulirus pascuensis* in remote islands of the southern Pacific: importance for its management and conservation. *Bulletin of Marine Science*, Volume 94, Number 3 pp. 753-774 (22).

**Freddy Hernandez-Vaca** and Wolfgang Schneider, 2020. ENSO Effects on the Humboldt Current System's Physical Oceanographic Conditions. *Hydrology* Submitted: 2020-01-30. Status: Decision pending. Manuscript ID: hydrology-721767.

Meerhoff E, Defeo O, Combes V, Franco B, Matano R, Piola A, **Hernández-Vaca F.**, Celentano E. 2020. Larval connectivity of the mole crab *Emerita brasiliensis* in the Uruguayan sandy coast. *Estuarine Coastal and shelf Science*. Submitted: 2020-04-15. Status: Decision pending.

### ÁREAS DE INVESTIGACIÓN

Principal: Oceanografía Física, Secundaria: Variabilidad Climática

## EXPERIENCIA DOCENTE

Año 2008: Matlab en Escuela de Hidrografía, Instituto Oceanográfico de la Armada del Ecuador.

Año 2008: Oceanografía Física para Biología Marina de la Pontificia Universidad Católica del Ecuador Sede Manabí.

## CRUCEROS OCEANOGRÁFICOS

Crucero Regional 2002, Instituto Oceanográfico de la Armada, Ecuador, septiembre 2002.

Crucero Regional 2009, Instituto Oceanográfico de la Armada, Ecuador, septiembre-octubre 2009.

Crucero Regional 2018, Instituto Oceanográfico de la Armada, Ecuador, septiembre -octubre 2018.

## ESTADÍAS DE INVESTIGACIÓN O ENTRENAMIENTO

Septiembre 2006, pasantía Universidad de Concepción. Chile. Manejo de información oceanográfica con el Dr. Wolfgang Schneider.

Mayo 2012- 31 mayo 2014, Profesional de la línea I+D: 3 COPAS Sur-Austral.

## OCUPACIÓN ACTUAL

Investigador Oceanográfico II, febrero 2003 - fecha actual.

División El Niño y Clima Oceánico, Instituto Oceanográfico de la Armada del Ecuador.

## CONTENIDO

Índice de figuras.....	xi
Índice de tablas.....	xii
Resumen.....	xiii
Abstract.....	xv

### **1 INTRODUCCIÓN..... 15**

1.1 Variabilidad climática y el Pacífico Sur oriental.....	15
1.2 El Niño Oscilación del Sur.....	17
1.3 Variabilidad climática en el Océano Pacífico.....	18
1.4 Variabilidad Climática en el Pacífico Sur Oriental.....	19
1.4.1 Agua Intermedia del Pacífico Sur Oriental.....	22

### **2 HIPÓTESIS Y OBJETIVOS ESPECÍFICOS..... 24**

2.1 Objetivo General.....	24
2.2 Objetivos específicos.....	24
2.2.1 Agua Intermedia del Pacífico Sur Oriental.....	24
2.2.2 El Niño y el Sistema de Corriente de Humboldt.....	24
2.2.3 Los Giros Subtropicales del Océano Pacífico.....	25

### **3 MATERIALES Y MÉTODOS..... 26**

3.1 Metodología del Capítulo 1: Agua intermedia del Pacífico Sur Oriental.....	26
3.1.1 Datos.....	26
3.1.2 Núcleo del AIPSO, propiedades y cambios temporales.....	26
3.1.3 Bombeo de Ekman.....	27
3.2 Metodología del Capítulo 2: El Niño y el Sistema de Corriente de Humboldt.....	27
3.2.1 Datos.....	27
3.2.2 Cálculos.....	28
3.3 Metodología del Capítulo 3: Giros Subtropicales del Océano Pacífico.....	29
3.3.1 Información.....	29
3.3.2 Variabilidad temporal del nivel del mar y su volumen asociado.....	29

### **4 RESULTADOS..... 31**

4.1	Capítulo 1: Contribución del bombeo de Ekman a los cambios en las propiedades y volumen del Agua Intermedia del Pacífico Sur Oriental.....	31
4.2	Capítulo 2: Efectos de ENOS sobre las condiciones oceanográficas físicas en el Sistema de Corrientes de Humboldt.....	44
4.3	Capítulo 3: Fortalecimiento de los Giros Subtropicales: Variabilidad y Tendencias (1993-2018) (Manuscrito en Preparación) .....	61
<b>5</b>	<b><u>DISCUSIÓN .....</u></b>	<b>84</b>
<b>6</b>	<b><u>CONCLUSIONES .....</u></b>	<b>86</b>
<b>7</b>	<b><u>REFERENCIAS.....</u></b>	<b>88</b>



## **LISTA DE FIGURAS**

Figura 1-1 Esquema de los cambios en la variabilidad climática. a) cambio en el promedio, b) cambio en la varianza y c) cambio en el promedio y varianza. (Fuente: Meehl et al., 2000). 15

Figura 3-1 a) Perfil de salinidad. Propiedades del AIPSO: LS Límite Superior y LI Límite Inferior. AIA Agua Intermedia Antártica. b) Diagrama TS. AIPSO está en rango 25,75 y 26,25 ( $\text{Kg/m}^3$ ) de  $\sigma_t$ . Información correspondiente a Perfil Código 3900347 US Argo Project 6-julio-2009, ubicación Longitud 80,838°O y Latitud 29,469°S..... 27

## **LISTA DE TABLAS**

Tabla 1-1 Modos de Variabilidad Climática. Adaptada de Talley et al. 2011..... 16





## RESUMEN

Impacto de la variabilidad climática durante la última década sobre la dinámica del giro subtropical en el Pacífico Sur Oriental y el volumen de Agua Intermedia del Pacífico Sur Oriental

Freddy Edinson Hernández Vaca

Doctorado en Oceanografía

Universidad de Concepción, 2020

Dr. Wolfgang Schneider, Profesor Guía

La variabilidad climática hace referencia a cambios del sistema climático con escalas de tiempo superiores a la escala estacional. En el Pacífico Tropical la perturbación climática con mayor intensidad es El Niño-Oscilación del Sur (ENOS) la cual tiene impactos globales. En la presente tesis se investigó el impacto que tiene la variabilidad climática en los Giros Subtropicales del Océano Pacífico, particularmente en la región oriental de Giro Subtropical del Pacífico Sur, para lo cual se empleó información de altimetría satelital, cruceros oceanográficos, modelos numéricos y derivadores oceanográficos del periodo 1993-2018. En detalle, tres procesos fueron estudiados, el impacto de: 1) incremento del esfuerzo del rotor del viento en la región de formación del Agua Intermedia del Pacífico Oriental (AIPSO) 2) ENOS sobre la hidrografía en el Sistema de Corrientes de Humboldt 3) ENOS y el incremento del nivel del mar en la intensificación de la circulación de los giros subtropicales.

En primer lugar, la distribución del AIPSO fue actualizada. La actualización se llevó a cabo con información nueva de ARGO (Array for Real-Time Geostrophic Oceanography). En esta tesis se trabajó con más de 46,000 perfiles obtenidos entre 2007-2012 del área entre la costa

occidental de América del Sur y el 150°O, y entre 5 y 40°S de latitud. Además, se complementó con datos de la transecta WOCE P06 (World Ocean Circulation Experiment) realizadas en 1992 y 2010 en 32°30' S en el Océano Pacífico Sur. Al comparar la actualización de la distribución del AIPSO con la realizada con información de 1990-2001, se estableció que el volumen AIPSO ha aumentado aproximadamente un 53%. Además, el área ocupada por AIPSO en la transecta WOCE P06 2010 fue 48% mayor que en 1992. La velocidad de bombeo de Ekman, calculada a partir del viento para el tiempo y la región de formación de AIPSO, mostró un aumento significativo en el bombeo de Ekman entre 2000 y 2012. El aumento en el bombeo de Ekman desde 2000 en adelante podría explicar los cambios observados en la distribución de AIPSO (la masa de agua tiene mayor extensión zonal) y propiedades (la salinidad mostró una disminución de 0.1). Estos cambios podrían explicarse como consecuencia de la variabilidad climática atmosférico sobre el océano interior.



En segundo lugar, se determinó el impacto del ENOS sobre el Sistema de Corrientes de Humboldt (SCH). Se analizó Temperatura superficial del mar (TSM), componentes de vientos cerca de la superficie, topografía dinámica absoluta (TDA), componentes de velocidad geostrofica y energía cinética de Edies (EKE) en el periodo 1993-2016. Se realizaron mapas de las variables originales o sus respectivas anomalías para todo el periodo y El Niño o La Niña que hubieron en el periodo de análisis. De acuerdo con el Índice Niño Oceánico se identificaron un total de 7 eventos de El Niño y 7 de La Niña, independientemente de la intensidad individual, la estación y la duración. Durante los eventos El Niño la TSM y los primeros 40 m de columna de agua fue 0,6°C más cálida y el TDA fue cerca de 5 cm más alto durante los eventos La Niña. Los vientos hacia el ecuador y favorable a la surgencia se intensificaron durante La Niña pero fueron más débiles durante El Niño,

aumentando y disminuyendo el afloramiento costero en los eventos anteriores y posteriores, respectivamente. Además, la componente meridional de la velocidad geostrófica, promediado para el HCS, fue aproximadamente un 10% de mayor magnitud durante los eventos de La Niña que durante los eventos El Niño. Esto dio lugar a un aumento de EKE durante los episodios de La Niña.

En tercer lugar, se utilizaron estimaciones de altimetría satelital de TDA entre 1993 a 2018 para analizar las fluctuaciones y tendencias de la intensificación de la circulación en los giros subtropicales. El nivel del mar disminuyó en los centros/núcleos de ambos giros subtropicales, pero se amplificó en los sistemas de las corrientes de California y Humboldt, en relación con los eventos de El Niño fuertes y moderados. Lo contrario ocurrió durante los eventos de La Niña. La intensidad en los Giros Subtropicales (Strength of the Subtropical Gyres, SoS) fue estimada como la diferencia del nivel del mar entre el centro del giro y su respectiva parte oriental dividido para distancia entre esos dos lugares. El SoS en ambos giros se debilitó bruscamente (moderadamente), hasta un 25% en los eventos El Niño fuertes (moderados) y aumentó en los episodios de La Niña. La circulación en el Pacífico Norte responde a El Niño dentro de uno o dos meses después de su ocurrencia, mientras, en el Pacífico Sur después de cinco a seis meses. Además, se detectó un modo interdecadal en el SoS, que aumentó (debilitó) su circulación durante la primera (segunda) mitad del período de observación. El aumento del nivel del mar, durante el período de altimetría satelital, 1993 a 2018, excedió la media de la cuenca en los centros/núcleos de los giros, pero estuvo por debajo de estos promedios en sus respectivas regiones orientales, especialmente en el Pacífico Sur. Esto produjo una aceleración de la circulación de ambos giros durante este período de 26 años.

## Abstract

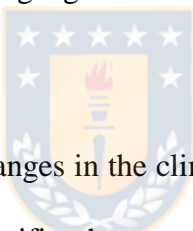
Impact of climatic variability over the last decade on the dynamics of the subtropical gyre in the South Eastern Pacific and the volume of Intermediate Water of the South Eastern Pacific

Freddy Edinson Hernández Vaca

Doctorate in Oceanography

Universidad de Concepción, 2020

Dr. Wolfgang Schneider, Advisor



Climate variability, here, refers to changes in the climate system with time scales longer than the seasonal scale. In the Tropical Pacific, the most intense climatic disturbance is El Niño-Southern Oscillation (ENSO), which in addition has global impacts. In the present thesis, the impact of climate variability on the Subtropical Gyres of the Pacific Ocean was investigated, particularly in the eastern region of the Subtropical Gyre of the South Pacific, using information from satellite altimetry, oceanographic cruises, numerical models and oceanographic drifters for the period 1993-2018. Here, three processes were studied, the impact: (1) increased wind stress curl had on the formation of Eastern South Pacific Intermediate Water; (2) ENSO had on the hydrography of the Humboldt Current System; and (3) ENSO and sea level rise had on the strength of the circulation of the subtropical gyres.

First, the Eastern South Pacific Intermediate Water (ESPIW) distribution was revisited. An update on the geometry of ESPIW has been possible based on new ARGO (Array for Real-Time Geostrophic Oceanography) data. This study comprised over 46,000 profiles obtained during 2007-2012 from an area between the western coast of South America and 150°W, and 5° and 40°S. This information was complemented with data from the World Ocean Circulation Experiment (WOCE) P06 transects conducted in 1992 and 2010 at 32°30'S in the South Pacific Ocean. Based on a comparison of this update and data from 1990-2001, it was established that the ESPIW volume has increased by approximately 53%. Moreover, the area occupied by ESPIW in the 2010 WOCE P06 transect was 48% higher than in 1992. Ekman pumping velocity, calculated from the wind for the time and region of ESPIW formation, showed a significant increase in Ekman pumping between 2000 and 2012. The increase in Ekman pumping from 2000 onward could explain the observed changes in ESPIW distribution (the water mass had extended zonally) and properties (salinity showed a decrease of 0.1). These changes could be explained as the consequence of atmospheric climate variability over the interior ocean.

Second, the impact of ENSO on the Humboldt Current System (HCS) was determined. Sea surface temperature (SST), near surface wind components, absolute dynamic topography (ADT), geostrophic velocity components, and eddy kinetic energy (EKE) were examined for the HCS, for the period 1993–2016. Composite maps of the original or derived ocean surface variables or their respective anomalies were constructed for the whole time series and separately for El Niño and La Niña episodes that fell into this time window. A total of 7 El Niño and 7 La Niña events, independent of individual strength, season and duration, were identified according to the Oceanic Niño Index. During El Niño events, SST and the upper 40 m of the water column were 0.6°C warmer and ADT was about 5 cm higher than during La

Niña events. Equatorward and upwelling favorable winds intensified during La Niña events but were weaker during El Niño events, thus increasing and decreasing coastal upwelling in the former and latter events, respectively. Further, the mean meridional component of geostrophic velocity, averaged for the HCS, was about 10% stronger during La Niña events than during El Niño events. This resulted in increased EKE during La Niña episodes.

Third, Satellite-born altimetry estimates of absolute dynamic topography from 1993 to 2018 were employed to shed light on fluctuations and trends of the strength of the circulation of the subtropical gyres. Sea level dropped in the centers/cores of both subtropical gyres but amplified in the boundary systems of the California and the Humboldt currents, related to strong and moderate El Niño events. The opposite occurred during La Niña events. The Strength of the Subtropical Gyres was estimated as the difference in sea level between the centers of the Gyres and its respective eastern boundaries, divided by the distance between these two locations. As a consequence of this anti-cyclical behavior the Strength of the Subtropical Gyres in both gyres weakened sharply (moderately), up to 25% during strong (moderate) El Niño events and increased in La Niña episodes. The circulation in the North Pacific responded to El Niño within one to two months of its occurrence, while in the South Pacific it did so after five to six months. Further, an inter-decadal mode was detected in the Strength of the Subtropical Gyres, which enhanced (weakened) their circulation during the first (second) half of the observational period. Sea level rise, during the satellite altimetry period, 1993 to 2018, exceeded the basin's mean in the centers/cores of the gyres but was below these means in its eastern boundaries, especially in the South Pacific. This yielded in an acceleration of the circulation of both gyres during this 26-year period.

# 1 INTRODUCCIÓN

## 1.1 Variabilidad climática y el Pacífico Sur oriental

El término Variabilidad Climática (VC) se refiere a las variaciones, del estado promedio y otras estadísticas del clima (e.g. varianza), en todas las escalas espaciales y temporales mayores a las estacionales (National Research Council, 1998; OMM, 2018). En la figura 1-1, se presenta un esquema de VC de una variable ambiental, tomando como ejemplo la temperatura máxima del aire (Meehl et al., 2000). De acuerdo con este esquema hay tres formas de variabilidad: a) cambio en el promedio, b) cambio en la varianza y c) cambios en el promedio y la varianza. Un cambio en el promedio podría interpretarse como un incremento en la frecuencia de eventos extremos y la disminución de otros, por ejemplo, los incrementos en el número de días cálidos y el descenso de número de días fríos. Por otro lado, el cambio en la varianza puede provocar cambios en ambos lados de la distribución de frecuencias, una disminución de los días cálidos y días fríos; por último, los cambios en la varianza y el promedio, pueden interpretarse como alteraciones en la ocurrencia de eventos extremos en diferentes formas como por ejemplo incremento de días cálidos y regularidad en los días fríos.

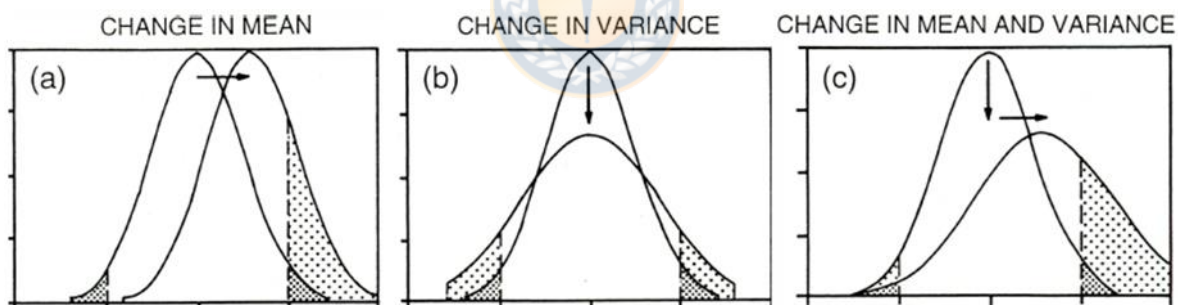


Figura 1-1 Esquema de los cambios en la variabilidad climática. a) cambio en el promedio, b) cambio en la varianza y c) cambio en el promedio y varianza. (Fuente: Meehl et al., 2000).

La VC se debe a condiciones naturales, interacciones internas entre los componentes del sistema climático (océano, atmósfera, tierra, hielo marino, glaciales, biogeoquímica) o forzamiento externo antropogénico. Sin embargo, actualmente el término VC se refiere a la variabilidad climática natural y el cambio climático al forzamiento antropogénico. Existen diferentes escalas temporales de la VC, interanual (mayor a un año y menor a 8 años), decadal (una a varias décadas), siglos, milenios o superiores. Los tipos de VC con mayor energía en escalas interanuales y decadales se describen en la tabla 1-1, cada uno está

asociado a un índice, el mismo que da pautas de su inicio, duración e intensidad. El Niño o El Niño Oscilación del Sur (ENOS) es la VC más intensa a escala interanual, con impactos globales.

**Tabla 1-1 Modos de Variabilidad Climática. Adaptada de Talley et al. 2011**

Nombre en inglés:	Acrónimo en inglés	Escala espacial	Escala temporal	Referencia:
Atlantic Meridional Mode	AMM	Cuenca	Interanual	Servain, 1991.
Atlantic Niño	AN	Regional	Interanual	Wang, 2002.
Artic Oscillation (Northern Annular Mode) relacionada a North Atlantic Oscillation	AO, (NAM) NAO	Global	Decadal	Hurrell et al., 2003; Visbeck et al., 2003.
East Atlantic Pattern	EAP	Cuenca	Decadal	Barnston y Livezey, 1987; Josey y Marsh, 2005
Atlantic Multidecadal Oscillation	AMO	Regional	Multidecadal	Enfield et al., 2001.
El Niño-Southern Oscillation	ENSO	Global	Interanual	Troup, A. J.1965
Pacific Decadal Oscillation	PDO	Cuenca-Regional	Decadal	Mantua et al., 1997.
North Pacific Gyre Oscillation	NPGO	Regional	Decadal	Di Lorenzo et al., 2008.
Indian Ocean Dipole Mode	IOD	Regional	Interanual	Saji et al., 1999.
Antartic Oscillation (también nombrada Southern Annular Mode)	AO SAM	Regional	Decadal	Thompson y Wallace, 2000.



## 1.2 El Niño Oscilación del Sur

El ENOS es el modo de VC que domina el Pacífico Tropical y es el más energético a nivel mundial (Trenberth et al., 2002; Larkin y Harrison, 2005 a,b; Brönnimann, 2007; Ng et al., 2017). Este tiene una alternancia casi periódica entre una fase cálida o El Niño y una fría o La Niña, ejerciendo influencias climáticas significativas en muchas regiones del mundo (Trenberth, 1997; Talley et al., 2011), mediante teleconexiones atmosféricas (McPhaden et al., 2006; Stan et al., 2017) y oceánicas (England y Huang, 2005, McPhaden et al., 2006).

Existen dos prerrequisitos para que se desarrolle un evento El Niño, acumulación en exceso de agua cálida en el Pacífico ecuatorial occidental (ej., Wyrski, 1985; Chen et al., 2016) y la presencia anomalías de vientos del oeste (ej. Luther et al., 1983; McPhaden et al., 1992; Chen et al., 2015). Cuando tales condiciones coinciden, el exceso de agua cálida puede ser transportado rápidamente hacia el este por corrientes oceánicas anómalas (ej. Wyrski, 1975; Miller et al., 1988; Huang et al., 2001), provocando un calentamiento en el Pacífico central y oriental.

Los prerrequisitos mencionados, son básicos e principales. Sin embargo, la complejidad del desarrollo de un evento El Niño va en conjunto con estructuras termohalinas en el Pacífico Ecuatorial, ejemplo el gradiente zonal de la termoclina juega un papel importante en la propagación de ondas Kelvin, (Mosquera et al., 2014). Al mismo tiempo la estructura de las isotermas depende de los cambios de los vientos alisios del sur,

El término El Niño ha evolucionado desde sus primeros reportes hasta la actualidad, diferentes investigadores han contribuido adicionando un "apellido" a su nombre de acuerdo al impacto del proceso, mecanismos de origen y sus tele conexiones ej., El Niño Central (Kao y Yu, 2009), El Niño Modoki (Ashok et al., 2007; Weng et al., 2009), El Niño Línea de Cambio de Fecha (Larkin y Harrison, 2005a, 2005b), El Niño Oriental (Capontodi et al. 2015); lo común de las definiciones es el seguimiento de las anomalías de la temperatura superficial del mar.

Para el caso de El Niño Oriental o Central, los eventos más fuertes han ocurrido en el Pacífico oriental, donde El Niño tiene mayor amplitud que La Niña. En el Pacífico central los eventos negativos son un poco más fuertes que los positivos, no existiendo simetría regional de la distribución de la anomalía de TSM, que representa una no linealidad en la diversidad de los eventos, Capontodi et al. 2015.

### 1.3 Variabilidad climática en el Océano Pacífico

La principal fuente de VC en el océano Pacífico es el ENOS, cuyos mayores impactos se centran en las regiones tropicales/ecuatoriales. El ENOS afecta a los ecosistemas (Glynn de Weerdt, 1991; Aronson et al, 2000), agricultura (Wilhite, et al. 1987), produce ciclones tropicales, sequías, incendios forestales, inundaciones y otros eventos climáticos extremos en todo el mundo (Philander, 1983, Cai, W. et al 2012).

En el contexto del ENOS y analizando variabilidad interdecadal en el Pacífico Tropical, Hu et al. 2013, establecieron dos periodos diferentes entre 2000-11 la variabilidad interanual fue significativamente débil que entre el periodo 1979-99. La diferencia entre estos periodos se debió a que en el más reciente se tuvo una combinación de vientos alisios fortalecidos y una mayor inclinación en la termoclina.

En el Pacífico Tropical Occidental, existió una tendencia en el aumento del nivel del mar de hasta 3 veces el promedio global, tendencia que está asociada con eventos ENSO y con el fortalecimiento del esfuerzo del viento, (Stammer et al. 2011, Merrifield y Maltrud, 2011, Qiu y Chen, 2012), así como con la variabilidad climática decadal, (Zhang y Church, 2012). De manera más amplia, el cambio del nivel del mar no es regular en todo el mundo, sino que ha mostrado fluctuaciones interanuales y decadales regionales que por lo general esconden las tendencias a largo plazo (Church y White 2011). Estas mismas pueden ser más importante que la variabilidad promedio global, como ha sido expuesto en estudios basados en altimetría satelital (ej Cazenave y Llovel 2010).

En los giros subtropicales la VC ha sido descrita como cambios del rotor del esfuerzo del viento (Roemmich y Cornuelle, 1990; Morris et al., 1996), cambios en la circulación (Roemmich y Cornuelle, 1990), cambios en el nivel del mar (Wyrcki K., 1985) y oscilaciones de 4 años entre el giro del Pacífico Sur y el del Pacífico Norte (Wyrcki y Wenzel, 1984), por dejándonos una idea clara que el impacto de la VC puede ser cuantificada en condiciones oceanográficas y meteorológicas.

En los giros subtropicales, la VC ha sido observada en las tendencias del nivel del mar, cambios en la circulación superficial y subsuperficial, y desplazamientos de los sistemas de corrientes. El giro Subtropical del Pacífico Sur ha experimentado una intensificación, que está asociada al incremento del nivel de mar al este de Nueva Zelanda, el mismo que podría estar relacionado al incremento de la circulación generada por el viento durante los 1990s, con un máximo alrededor del 2003 (Roemmich et al., 2007). La presencia de grandes

anomalías positivas del nivel del mar sobre el Pacífico central y occidental a finales de los años 90s fue confirmada por un modelo de circulación oceánico (e.g. Sasaki et al., 2008). Cai (2006) mostró que los cambios en los vientos superficiales han forzado un cambio en el flujo hacia el sur y una intensificación del giro, el cual tiene nexos con el Pacífico Subtropical y con la circulación en el Océano Indico y en el Atlántico. Por otro lado, en el giro Subtropical del Pacífico Norte, el aumento del nivel del mar varió desde la isoterma de 12°C y con el desplazamiento hacia el sur de la Contracorriente Ecuatorial del Norte, Qiu y Chen (2012).

Otro tipo de impacto de la VC en la tendencia global o regional del nivel del mar, depende de la longitud de los registros; en periodos desde el inicio de la altimetría satelital en 1993, la interpretación de la tendencia regional es compleja ya que es afectada por la VC a escala interanual o interdecadal (Zhang y Church, 2012) y en un periodo más corto 2005-2014 la tendencia del nivel del mar fue afectada por la variabilidad mensual (Chambers et al., 2017).

#### 1.4 Variabilidad Climática en el Pacífico Sur Oriental

Se conoce como el Pacífico Sur oriental (PSO) a la región comprendida entre los 25° y 45°S de latitud y desde la costa de Chile a los 100°O de longitud Figura 1.3. En esta región del Océano Pacífico ocurren procesos atmosféricos que son modulados por el Anticiclón Subtropical del Pacífico Sur, como la presencia predominante de vientos hacia el ecuador cerca de las costas norte y centro de Chile y procesos oceanográficos como la circulación superficial hacia el norte, subducción de agua, surgencia costera y remolinos de meso escala.

Los procesos oceanográficos y meteorológicos en esta área son modulados por los ciclos ENOS (Montecino et al., 2003, Montecino et al., 2007; Yu et al. 2010, Ancapichún y Garcés-Vargas, 2015, Imada et al., 2016; Su et al., 2018; Timmermann et al., 2018).

La variabilidad estacional del viento superficial a lo largo del PSO es producida por la migración estacional APS y la fricción con el continente. El régimen de vientos en el PSO, incluye los Vientos Alisios del sureste controlado por el APS, aunque Rahn y Garreaud, 2014 encontraron que a lo largo de la costa de sudamérica entre el 35°S y 45°S de latitud existe un reverso en la dirección hacia el ecuador en verano y hacia el polo en invierno. En el PSO diversos autores toman entre 35°S y 38°S las latitudes donde la componente de los vientos a lo largo de la cota se dividen en una componente predominante hacia el norte y una componente predominante hacia el sur (Sobarzo et al., 2007, Rahn y Garreaud, 2014). De

este modo, a lo largo de la costa central y norte de Chile, así como en las costas de Perú, predominan vientos favorables a la surgencia durante todo el año. Existen dos regiones de vientos máximos a lo largo de la costa centrada en la latitud 15°S y 30°S S (Shaffer et al. 1999, Thomas et al. 2001, Hormazábal et al. 2004).

Al sur de ~ 35°S, la estacionalidad del ASP origina máximos de afloramientos en verano y condiciones promedio de vientos hacia el polo en invierno; estos últimos provocan hundimiento de aguas (proceso contrario a la surgencia) que también está influenciada por las tormentas de invierno asociadas al frente polar (Shaffer et al. 1999, Rutllant et al. 2004). En un enfoque temporal más amplio, Schneider et al. (2017), utilizaron información de vientos y presión superficial entre 2002 y 2013, relacionaron el promedio de los vientos a lo largo de la costa y la ubicación del APS notando que los vientos son relativamente débiles y del norte cuando el APS se ubicó en 27°S, y que cerca de 35°S hubo inversión de los vientos con velocidades promedio de 5m/s.

El Sistema de Corrientes de Humboldt (SCH) o Sistema Perú-Chile (también conocida como Sistema de Corrientes de Perú- Chile), Chavez et al., 2008, está constituido por un flujo hacia el Ecuador en la región oriental del Giro Subtropical del Pacífico Sur, limitado al norte por el sistema de corriente ecuatorial y al sur por los vientos de la deriva del oeste. EL SCH es uno de los 4 mayores Sistemas de Corriente de Borde Oriental, caracterizado por vientos predominantes hacia el ecuador, transporte de Ekman costa afuera, afloramiento costero de aguas de menor temperatura, ricas en nutrientes y por una alta productividad pesquera, (Hill et al. 1998); además contiene flujos más pequeños hacia el sur como la Contracorriente Costera de Chile y la Corriente Costera de Perú, estas últimas influenciadas por vientos locales y la surgencia costera (Wyrтки, 1967; Strub et al., 1998; Aiken et al., 2008).

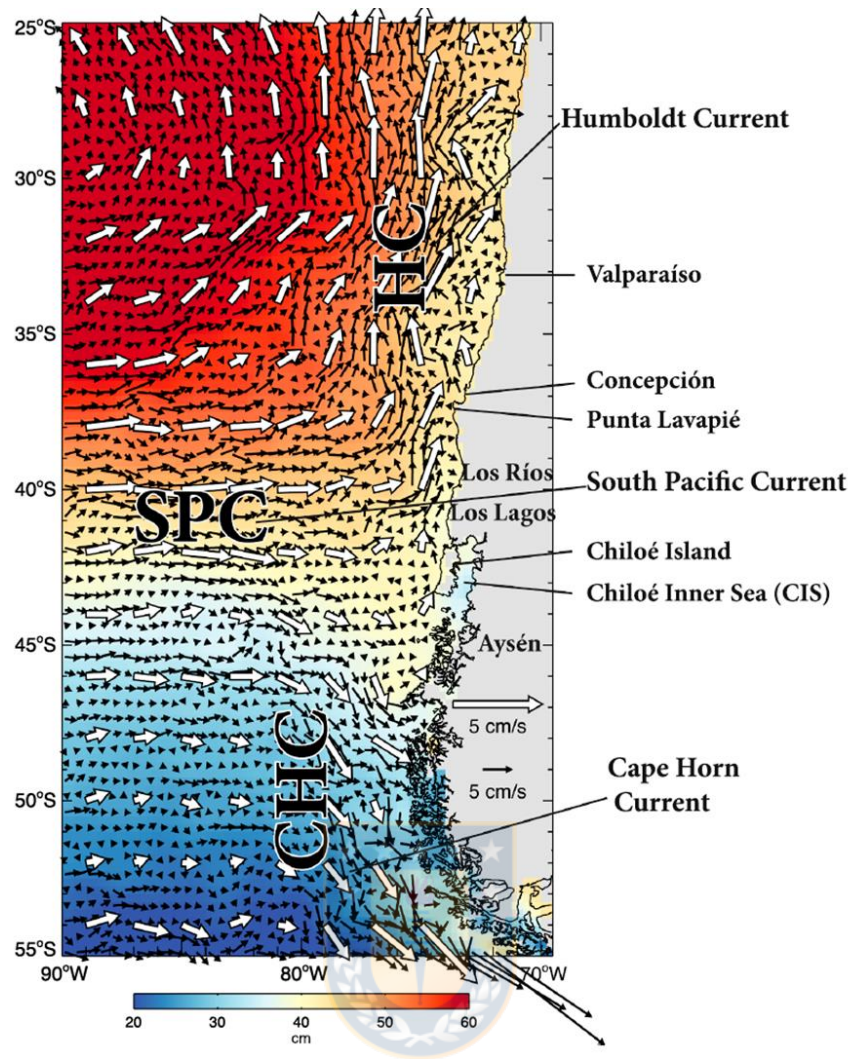
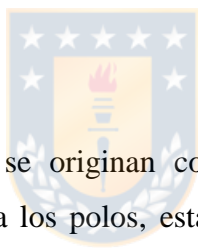


**Figura 1-2** Pacífico Sur Oriental. Los colores representan el promedio de la Topografía Dinámica. El promedio de la velocidad geostrófica cada  $1/4^\circ$  en latitud y longitud está representado por vectores de color negro, mientras que los vectores blancos muestran promedios espaciales de  $2^\circ$ . Existen diferentes escalas de vectores para los dos resultados. Fuente: Strub et al., 2019.

El flujo oceánico principal hacia el norte es la Corriente de Humboldt (CH) se extiende desde el Sur de Chile ( $45^\circ\text{S}$ ), donde los Vientos de la Deriva del Oeste llegan a la costa de Sur América, hasta el norte de Perú ( $4^\circ\text{S}$ ), donde las aguas frías de afloramiento se encuentran con agua tropical para formar, luego, el Frente Ecuatorial (Chavez y Messié, 2009). La posición del inicio de la CH en el verano es en el  $40^\circ\text{S}$  y  $70^\circ\text{O}$  y en invierno en el  $38^\circ\text{S}$  y  $76^\circ\text{O}$  y aproximadamente en  $25^\circ\text{S}$  de latitud se divide en dos ramales, uno hacia las costas peruanas y otro oceánico. La CH desde su origen en el sur hasta el punto de división, es más

estrecha y se intensifica de 2 a 3 cm/s en verano más que invierno (Figura 4 en Fuenzalida et al., 2008).

La VC debida al ENOS ha sido ampliamente estudiada en el SCH. En este sistema, durante El Niño se ha observado la propagación de anomalías positivas de temperatura, elevación del nivel del mar, termoclina más profunda, disminución o una inversión episódica del flujo costero hacia el ecuador. En contraste, durante la Niña, se ha observado la disminución de los niveles del mar costero, termoclinas con menor profundidad, anomalías negativas de temperatura superficial del mar y un flujo costero ecuatorial fortalecido. Los datos satelitales muestran que las anomalías El Niño pueden extenderse al sur de 40°S e incluso podrían incluir toda la costa de América del Sur (Carr et al. 2002, Strub y James 2002), pero las anomalías disminuyen en latitudes más al sur (Strub y James 2002, Montecinos et al. 2003, Escribano et al. 2004). Las condiciones El Niño también pueden ser impuestas por vientos locales anómalos, probablemente modulados a través de teleconexiones atmosféricas (Shaffer et al. 1999).



Las señales oceánicas ENOS que se originan como ondas Kelvin ecuatoriales que se propagan hacia el este y luego hacia los polos, esta propagación está descrita como ondas Rossby (Pizarro et al. 2002) además, Ramos et al. (2008) se refieren como conexión de la variabilidad tropical con la extratropical dada por las ondas Kelvin originadas en el ecuador.

#### **1.4.1 Agua Intermedia del Pacífico Sur Oriental**

El Agua Intermedia del Pacífico Sur Oriental (AIPSO) es de origen subantártico, está en rangos de menor profundidad y salinidad que el Agua Intermedia Antártica (AIAA). El AIPSO da origen a un mínimo de salinidad somero que se distingue del mínimo de salinidad intermedio que forma el AIAA. El AIPSO se encuentra por debajo del Agua Superficial Subtropical y sobre el Agua Ecuatorial Subsuperficial (Schneider et al., 2003; Emery y Meincke, 1986). Esta masa de agua también es conocida como Agua del Mínimo de Salinidad Somero del Pacífico Sur (Reid, 1973; Tsuchiya, 1982; Kartensen, 2004) o Agua Subantártica (Silva et al., 2009), en esta tesis nos referiremos como Agua Intermedia del Pacífico Sur Oriental (AIPSO).

EL AIPSO se forma por la subducción de agua de menor salinidad (Agua Superficial Subantártica) en las cercanías de la latitud 37°S y luego es transportada hacia el norte y oeste en el PSO del GSTPS por la corriente de Humboldt (Reid, 1973; Tsuchiya, 1982; Schneider et al., 2003; Leth et al. 2004). La subducción se define como el fluido que deja la capa de mezcla superficial de manera irreversible hacia la piconclina permanente, término que se aplicó en el GSTPN (Woods y Barkman, 1986; Huang y Qiu, 1994).

Las propiedades y extensión del AIPSO, en primera instancia, fueron inferidas a partir de la masa de agua análoga del Pacífico Norte, Agua intermedia del Pacífico Norte, Emery y Meincke, 1986; Tsuchiya y Talley, 1996, reportaron que el origen del AIPSO es al Sur de la Corriente de Humboldt habiendo encontrado su característica en la sección oceanográfica realizada a lo largo del meridiano los 135°O. Schneider et al. (2003) definen sus características y propiedades físicas con información hidrográfica entre 1991-2000 y Katernsen (2004) mencionó que el origen de agua de menor salinidad del AIPSO no necesariamente está restringido al Agua Superficial Subantártica, sino que es agua de menor salinidad proveniente del oeste con el Giro Subtropical del Pacífico Sur.

El conocimiento del AIPSO no es mayor y por ende no se tiene referencias sobre el impacto de la VC sobre su distribución y propiedades; sin embargo, se tiene referencias sobre la variabilidad interanual en las tasas de subducción en aguas de origen subtropical. Por ejemplo, en el Pacífico norte la tasa de subducción en el Modo de Agua Central tuvo gran variabilidad interanual, siendo mayor 2005 y 2010 pero casi nula en el 2009, resultados de Toyama et al. (2015) quienes trabajaron con información de boyas Argo entre 2005 y 2012.

En esta tesis se describe los impactos de la Variabilidad Climática en los patrones de del nivel del mar, circulación superficial en los giros subtropicales del Pacífico, con énfasis en la región oriental del giro del Pacífico Sur.

El Sistema de Corrientes de Humboldt en esta tesis se muestra como una gran región oceanográfica, en la misma se evaluó las características físicas dentro de dos escenarios El Niño y la Niña, además de describir los impactos dados por El Niño o La Niña, se describe el impacto de la variabilidad climática en la zona de formación del AIPSO como un forzante de los cambios encontrados en la distribución y geometría de esta masa de agua.

## 2 HIPÓTESIS Y OBJETIVOS ESPECÍFICOS

### 2.1 Objetivo General

La hipótesis y objetivo general planteado para esta tesis son:

La variabilidad climática impacta la circulación oceánica-atmosférica, propiedades físicas y masas de agua de los Giros Subtropicales del Océano Pacífico; el objetivo general es: Describir los cambios en la circulación de los Giros Subtropicales del Océano Pacífico y particularmente en la región oriental de Giro Subtropical del Pacífico Sur. Además, cuantificar los cambios en las propiedades físicas y el volumen del Agua Intermedia del Pacífico Sur Oriental.

Para cumplir el objetivo general esta tesis se plantea en tres capítulos nombrados de la siguiente manera:

Capítulo 1: Agua intermedia del Pacífico Sur Oriental.

Capítulo 2: El Niño y el Sistema de Corriente de Humboldt.

Capítulo 3: Los Giros Subtropicales del Océano Pacífico.

### 2.2 Objetivos específicos



#### 2.2.1 Agua Intermedia del Pacífico Sur Oriental.

Objetivo 1: Reevaluar la distribución del Agua intermedia del Pacífico Sur Oriental

Objetivo 2: Cuantificar los cambios temporales en la geometría del AIPSO, en la salinidad dentro del núcleo del AIPSO y del Bombeo de Ekman en la región de formación del AIPSO.

#### 2.2.2 El Niño y el Sistema de Corriente de Humboldt.

Objetivo 1: Establecer diferencias en ambas fases del ENOS de la temperatura superficial del mar, vientos cercanos a la superficies, nivel del mar, circulación geostrófica y energía cinética en la región del Sistema de Corrientes de Humboldt.

Objetivo 2: Analizar los cambios en los primeros 100 m de la columna de agua de la temperatura productos del ENOS.



### 2.2.3 Los Giros Subtropicales del Océano Pacífico.

Objetivo 1: Determinar el aumento diferencial en el nivel del mar en cada Giro Subtropical del Océano Pacífico así como evaluar la relación de cambios entre el centro de cada giro y su respectiva región oriental.

Objetivo 2: Investigar la contribución del ENOS en el fortalecimiento de la circulación de los giros subtropicales.



### 3 MATERIALES Y MÉTODOS

#### 3.1 Metodología del Capítulo 1: Agua intermedia del Pacífico Sur Oriental

##### 3.1.1 Datos

Para cumplir con los objetivos específicos del capítulo 1, se utilizaron:

- 46.000 perfiles de salinidad, del programa Array for Real-Time Geostrophic Oceanography (ARGO), 132 de la transecta P06 del World Ocean Circulation Experiment (WOCE P06) y 20 de los Cruceros de Investigación Marina (CIMAR).
- Vientos superficiales provenientes de cinco fuentes, información derivada de satélites: 1) ERS1/2 AMI, obtenidos de IFREMER /CERSAT, 2) QuikSCAT obtenido del Centre d'Exploitation et de Recherche Satellitaire d'Archivage et de Traitement (CERSAT) at the Institut Francais de Recherche pour l'Exploitation de la Mer (IFREMER); información de modelos: 3) ERA-Interim, 4) Navy Operational Global Atmospheric Prediction System (NOGAPS) model "Fleet Numerical Meteorology and Oceanography Center" (FNMOC), y 5) Datos de reanálisis del National Center for Environmental Prediction (NCEP). Detalles de las resoluciones, periodos en uso y productos se encuentran en la tabla 1 del manuscrito 3. .

##### 3.1.2 Núcleo del AIPSO, propiedades y cambios temporales

El núcleo del AIPSO se calculó en base a cada perfil de salinidad proveniente de ARGO para lo cual se utilizó la metodología de Schneider et al., (2003). Este núcleo se encuentra ubicado a una menor profundidad que la salinidad mínima del Agua Intermedia Antártica (AIA). El núcleo del AIPSO está marcado por el valor de la salinidad mínima del AIA, el cual se proyecta hacia la superficie e intercepta la zona de menor salinidad y profundidad. Estos valores de intersección demarcan el límite superior, el límite inferior y el espesor del núcleo del AIPSO. La extensión del AIPSO está representada como el promedio de salinidad en rangos de  $\sigma_t$  entre 25,75 y 26,25 kg/m<sup>3</sup>, Schneider et al. (2003). Para un mejor detalle ver, Figura 3-1 a) Perfil de salinidad. Propiedades del AIPSO: LS Límite Superior y LI Límite Inferior. AIA Agua Intermedia Antártica. b) Diagrama TS. AIPSO está en rango 25,75 y 26,25 (Kg/m<sup>3</sup>) de  $\sigma_t$ . Información correspondiente a Perfil Código 3900347 US Argo Project 6-julio-2009, ubicación Longitud 80,838°O y Latitud 29,469°S.Figura 3-1.

Los resultados de la geometría y distribución del AIPSO obtenidos con la información ARGO, 2007-2012, se compararon con los de Schneider et al. (2003) quienes usaron información del periodo 1990-2001. Para obtener la ubicación relativa que tuvo el AIPSO se compararon las transectas de salinidad de WOCE P06 (costa de Chile hasta el 110°O) realizadas en el 2010 y 1992; con los perfiles de CIMAR llevadas a cabo en 1999 y 2015 se promedió la salinidad en los rangos de  $\sigma_t$  entre 25,75 y 26,25  $\text{kg/m}^3$  para los años señalados y luego se estableció su diferencia.

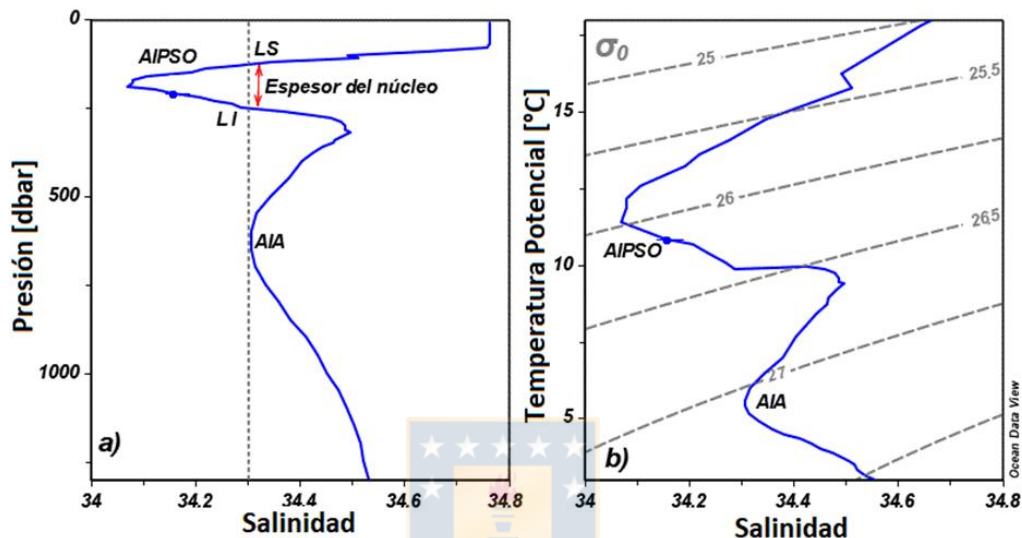


Figura 3-1 a) Perfil de salinidad. Propiedades del AIPSO: LS Límite Superior y LI Límite Inferior. AIA Agua Intermedia Antártica. b) Diagrama TS. AIPSO está en rango 25,75 y 26,25 ( $\text{Kg/m}^3$ ) de  $\sigma_t$ . Información correspondiente a Perfil Código 3900347 US Argo Project 6-julio-2009, ubicación Longitud 80,838°O y Latitud 29,469°S.

### 3.1.3 Bombeo de Ekman

El Bombeo de Ekman se calculó con los productos de vientos, de acuerdo a Tomczak y Godfrey (1994). Se realizaron series de tiempo anuales del Bombeo de Ekman en la región y tiempo de formación del AIPSO y se establecieron dos periodos de tendencia 1991-2000 y 2000-2012.

## 3.2 Metodología del Capítulo 2: El Niño y el Sistema de Corriente de Humboldt

### 3.2.1 Datos

Para cumplir los objetivos específicos de este capítulo se empleó información de: Información mensual de temperatura superficial del mar y vientos superficiales fue obtenida del European Center Medium Weather Forecast ERA (ECMWF Re-Analysis) Interim

reanalysis project, se trabajó con información entre enero de 1993 a diciembre de 2016 con resolución horizontal de  $0,4^\circ$  en latitud y longitud.

Información grillada de perfiles de temperatura del mar en base a perfiles de Array for Real-Time Geostrophic Oceanography (ARGO), Roemmich and Gilson (2009), fueron obtenidos de [sio-argo.ucsd.edu/RG\\_Climatology.html](http://sio-argo.ucsd.edu/RG_Climatology.html), se trabajó con datos de los primeros 100 m de la columna de agua.

13 perfiles de temperatura de dos cruceros de investigación CIMAR 5 y CIMAR 21; cruceros efectuados en 1999 (13 octubre a 12 noviembre) y 2015 (12 octubre a 11 noviembre) respectivamente; la información corresponde a un sector específico del crucero entre  $70,94^\circ\text{O}$  y  $86,55^\circ\text{O}$  a lo largo del  $27^\circ\text{S}$  de latitud.

Además también se empleó la información del Índice Niño Oceánico y datos diarios del Nivel del Mar (TDA) en el periodo 1993-2016

### 3.2.2 Cálculos

Con los datos mensuales de vientos se calculó el esfuerzo del viento fue calculado de acuerdo a Trenberth et al., 1990, con esa estimación se procedió a la estimación del Rotor del Esfuerzo del Viento. La energía cinética fue calculada de acuerdo a Che et al. 2009.

En cada punto de grilla y en cada variable se obtuvieron la climatología mensual y posterior su respectiva anomalía. Se presentan mapas de condiciones de anomalías de todas las variables en condiciones El Niño y La Niña. Los periodos El Niño y La Niña son tomados a con la definición operacional del Índice Niño Oceánico.

Se promedió los 13 perfiles de temperatura de cada crucero CIMAR, y se efectuó la diferencia entre CIMAR 21 - CIMAR 5, se presenta el perfil diferencia de hasta una profundidad de 100m.

Con la información ARGO se seleccionó en dos latitudes  $22,5^\circ\text{S}$  y  $32,5^\circ\text{S}$ . Con los 13 años de información (2004-2018) se calculó su promedio climatológico y en base este promedio se obtuvo sus anomalías. Las anomalías fueron promediadas desde noviembre 2014 a marzo 2016 (Condiciones EL Niño) y de junio 2010 a marzo 2012 (Condiciones La Niña). Se presenta el perfil diferencia Condiciones El Niño menos Condiciones La Niña.

### 3.3 Metodología del Capítulo 3: Giros Subtropicales del Océano Pacífico.

#### 3.3.1 Información

Nivel del mar:

Para cumplir los objetivos específicos planteados en la sección 2.2.3 se empleó información de altimetría satelital, con su variable estimada Topografía Dinámica Absoluta (TDA), del Copernicus Marine Environment Monitoring Service (CMEMS) server [ftp://my.cmems-de.eu/Core/SEALEVEL\\_GLO\\_PHY\\_L4\\_REP\\_OBSERVATIONS\\_008\\_047/dataset-duacs-rep-global-merged-allsat-phy-I4](ftp://my.cmems.de.eu/Core/SEALEVEL_GLO_PHY_L4_REP_OBSERVATIONS_008_047/dataset-duacs-rep-global-merged-allsat-phy-I4) . La información empleada es diaria del periodo 1993-2018, la misma tiene resolución horizontal de  $0,25^\circ \times 0,25^\circ$  en latitud y longitud.

Índice el Niño Oceánico:

Datos correspondientes al Índice El Niño Oceánico del periodo 1993-2018 fueron obtenidos del sitio web de la NOAA [http://origin.cpc.ncep.noaa.gov/products/analysis\\_monitoring/ensostuff/ONI\\_v5.php](http://origin.cpc.ncep.noaa.gov/products/analysis_monitoring/ensostuff/ONI_v5.php). Un valor del índice sobre (bajo) el límite  $0,5^\circ$  ( $-0,5^\circ\text{C}$ ) por al menos cinco periodos consecutivos corresponde a un evento El Niño (La Niña).

#### 3.3.2 Variabilidad temporal del nivel del mar y su volumen asociado

En cada punto de grilla, en base a los datos diarios, se estimaron los promedios mensuales y luego los promedios anuales, luego se definieron series de tiempo de promedios de regiones del centro y lado oriental de cada giro, figura 1 del manuscrito en preparación, previo al cálculo de promedio en áreas, se realizó la ponderación del promedio mensual del TDA con el área respectiva de influencia de cada punto de grilla, esto debido al hecho de que el área representada por cualquier punto de grilla de TDA depende de su latitud y la misma disminuye desde el ecuador hacia los polos. A las series de tiempo ponderadas en las regiones del giro se les retiró la estacionalidad aplicando un filtro media móvil de 12 meses de avance y retroceso.

En cada punto de grilla se calculó el volumen asociado con su valor del promedio mensual de TDA; el volumen resultó de multiplicar el TDA promedio con el área de representación de cada punto de grilla, área de acuerdo a la localización geográfica. Se obtuvieron las anomalías de volumen respecto a la climatología mensual del volumen estimado. Las series de

anomalías de volumen también fueron filtradas con la media móvil de avance y retroceso de 12 meses para retirar la variabilidad intraanual.

Cálculo de tendencias, interpretación de fortalecimiento temporal de los Giros Subtropicales se muestran en detalle en literal de resultados del artículo en preparación, sección 4.



## 4 RESULTADOS

4.1 Capítulo 1: Contribución del bombeo de Ekman a los cambios en las propiedades y volumen del Agua Intermedia del Pacífico Sur Oriental.

Manuscrito publicado en revista Gayana: <http://dx.doi.org/10.4067/S0717-65382017000200052>, Hernández-Vaca, F., Schneider, W., Garcés-Vargas, J. Contribution of Ekman pumping to the changes in properties and volume of the Eastern South Pacific Intermediate Water.



## Contribution of Ekman pumping to the changes in properties and volume of the Eastern South Pacific Intermediate Water

### Contribución del bombeo de Ekman a los cambios en las propiedades y volumen del Agua Intermedia del Pacífico Sur Oriental

FREDDY HERNÁNDEZ-VACA<sup>\*1,2,3</sup>, WOLFGANG SCHNEIDER<sup>3,4</sup> & JOSÉ GARCÉS-VARGAS<sup>5,6</sup>

<sup>1</sup>Programa de Postgrado en Oceanografía, Facultad de Ciencias Naturales y Oceanográficas, Universidad de Concepción, Casilla 160-C, Concepción, Chile.

<sup>2</sup>Dirección Oceanografía Naval, Instituto Oceanográfico de la Armada. Apartado postal: 5940 Guayaquil, Ecuador.

<sup>3</sup>Instituto Milenio de Oceanografía (IMO), Universidad de Concepción. Proyecto IC 120019

<sup>4</sup>Departamento de Oceanografía, Universidad de Concepción, Campus Concepción, Víctor Lamas 1290, Casilla 160-C, código postal: 4070043, Concepción, Chile.

<sup>5</sup>Instituto de Ciencias Marinas y Limnológicas, Facultad de Ciencias, Universidad Austral de Chile, código postal: 5090000, Valdivia, Chile.

<sup>6</sup>Centro FONDAP de Investigación en Dinámica de Ecosistemas Marinos de Altas Latitudes (IDEAL)

\* freddyhernandez@udec.cl

#### ABSTRACT

An update on the Eastern South Pacific Intermediate Water (ESPIW) distribution has been possible based on ARGO (Array for Real-Time Geostrophic Oceanography) data. This study comprised over 46,000 profiles obtained during 2007-2012 from an area between the western coast of South America and 150°W, and 5° and 40°S. This information was complemented with data from the World Ocean Circulation Experiment (WOCE) P06 transects conducted in 1992 and 2010 at 32°30'S in the South Pacific Ocean. Based on a comparison of this update and data from 1990-2001, it was established that the ESPIW volume has increased by approximately 53%. Moreover, the area occupied by ESPIW in the 2010 WOCE P06 transect was 48% higher than in 1992. Ekman pumping velocity, calculated from the wind for the time and region of ESPIW formation, showed a significant increase in Ekman pumping between 2000 and 2012. The increase in Ekman pumping from 2000 onward could explain the observed changes in ESPIW distribution (the water mass had extended zonally) and properties (salinity showed a decrease of 0.1). These changes could be explained as the consequence of atmospheric climate variability over the interior ocean.

**KEYWORDS:** South Pacific, wind stress curl, intermediate water, subduction.

#### RESUMEN

Una actualización de la distribución del Agua Intermedia del Pacífico Sur Oriental (AIPSO) fue realizada con datos ARGO (Array for Real-Time Geostrophic Oceanography). Este estudio comprendió más de 46.000 perfiles obtenidos durante 2007-2012 del área entre la costa occidental de Sudamérica y 150° O, y 5°S y 40°S. Esta información se complementó con datos de las secciones P06 del World Ocean Circulation Experiment (WOCE) realizadas en 1992 y 2010 en 32° 30'S en el Océano Pacífico Sur. Comparando ésta actualización y los datos de 1990-2001 se estableció que el volumen del AIPSO ha aumentado aproximadamente un 53%. Además, el área ocupada por AIPSO en el transecto WOCE P06 de 2010 fue 48% más grande que en 1992. La velocidad de bombeo Ekman, calculada a partir del viento para el tiempo y la región de la formación del AIPSO, mostró un aumento significativo en el bombeo de Ekman entre 2000 y 2012. El aumento del bombeo de Ekman desde el 2000 podría explicar los cambios observados en la distribución del AIPSO (la masa de agua se extendió zonalmente) y las propiedades (la salinidad disminuyó 0.1). Estos cambios podrían explicarse como la consecuencia de la variabilidad climática atmosférica sobre el océano interior.

**Palabras clave:** Pacífico Sur, rotor del esfuerzo del viento, agua intermedia, subducción.



## INTRODUCTION

The South Pacific (SP) Ocean exhibits an anticyclonic circulation around the center of the subtropical gyre. This is limited in the north by the westward-flowing Southern Equatorial Current whereas its western Australian border, the flux moves southward as the East Australian Current. At around 35°S, the southern limit of the gyre, the SP current heads eastward, and closing the circulation cell at the eastern border it is the Humboldt Current System or the Peru-Chile Current System (Talley *et al.* 2011).

The subtropical region and mid-latitudes of the SP are influenced by positive wind stress curl, which leads to downward Ekman velocity (referred to as Ekman pumping) and subtropical convergence (STC) (Chereskin & Price 2009; Stramma *et al.* 1995). In STC, water subducted within the main thermocline advances toward the north, upwells at the equator, and returns to the subtropics through the surface layer in the western boundary current system. This circulation is known as either the Subtropical Cell (McCreary & Lu 1994) or the shallow meridional overturning circulation (Chen *et al.* 2015). Through this circulation, the properties of surface water from the subtropics are transmitted to the tropics. South of the subtropical gyre, in the Southern Ocean, there is interaction between deep and intermediate circulations, upwelling of deep waters, and freshwater-heat transfers between the ocean and the atmosphere. This transforms deep water into intermediate water and/or water within the thermocline that later forms part of the circulation managed by the wind that could return to deep convection sites (Talley 1999).

Emery and Meincke (1986) described the water masses in the SP as follows: a) upper (0-500 m), comprising East and West South Pacific Central Waters, Subantarctic Surface Water (SASW), Antarctic Surface Water, and East South Pacific Transition Water, and including Tropical and Subtropical Surface Water and Equatorial Subsurface Water; b) intermediate (500-1500 m), comprising Antarctic Intermediate Water (AAIW) and Eastern South Pacific Intermediate Water (ESPIW); and c) deep and abyssal (>1500 m), comprising Pacific Deep Water and Antarctic Bottom Water.

In the southeastern SP, the presence of surface Transition Water reflects the connection between subpolar and subtropical regions, i.e., the SASW and the East South Pacific Central Water. The physical properties of water masses such as temperature and salinity are acquired on the surface via air-sea interaction or via the mixing of two or more water masses. In the eastern SP, SASW is much fresher than in the west because of the heavy precipitation and freshwater runoff from Chilean Patagonia. Thus, this creates a low-salinity tongue that stretches from the coast of South America toward the central SP at around 45°S (Karstensen 2004).

Subduction induced by wind stress curl in subtropical regions (i.e., STC) is the origin of the central water masses. Subducted water from the base of the Ekman layer enters irreversibly into the permanent pycnocline. From there, it then moves toward the tropics following density gradients, which aids both the ventilation of the permanent thermocline over decades (Tomczak & Godfrey 1994) and the sequestration of anthropogenic CO<sub>2</sub> in the SP. According to the theories called “Mixed-layer Demon Hypothesis” (Stommel 1979) and thermocline ventilation (Luyten *et al.* 1983; Sprintall & Tomczak 1993), the temperature and salinity properties of central water are acquired only in winter.

In the Eastern SP, north of the region of STC, there is an upper minimum-salinity water mass referred to as Shallow Salinity Minimum Water (Reid 1973; Tsuchiya & Talley 1998; Karstensen 2004) or as ESPIW (Emery & Meincke 1986). A conceptual diagram, shown in Figure 1, illustrates both the subduction process at the region of STC and the formation of central water masses. The westerly winds cause an equatorward Ekman transport (red arrow, arrowhead to the right), whereas the Ekman transport produced by the southeast trade winds is poleward (red arrow, arrowhead to the left). This leads to the creation of the STC (30°-35°S) where SASW is subducted, forming ESPIW. Once subducted, ESPIW continues its northward path at depths of 120-220 m, moving between the saltier Subtropical Surface and Equatorial Subsurface Waters. Thus, ESPIW originates on the southeastern side of the subtropical gyre, between the coast of South America and 90°W (Schneider *et al.* 2003). Subsurface water with minimum salinity, corresponding to ESPIW, is surface water in the high latitudes with low salinity and high oxygen levels (Reid 1973). ESPIW specifically originates between 33°S and 38°S (Schneider *et al.* 2003) and once subducted, it continues moving toward the equator following the direction of the Humboldt Superficial Current System.

Atmospheric climate variability has an impact on the ocean. For example, intensification of coastal wind stress leads to an increase in coastal upwelling (Bakun 1990). The recent hiatus in global warming, a period during which Earth’s global average surface air temperature has remained more-or-less steady since 2001 (Liu *et al.* 2017), has been attributed to the higher intensity of the southern trade winds in the SP during the past two decades (England *et al.* 2014). In the interior ocean, strengthened Ekman pumping caused by increased wind stress curl has led to intensification of Eastern Subtropical Mode Water in the SP Subtropical Gyre during the last century (Liu & Wu, 2012). The balance between evaporation and precipitation of the SP could explain the increase in salinity in AAIW observed throughout the World Ocean Circulation Experiment (WOCE) transect at 32.5°S, conducted in 2003 and 1992 (Schneider *et al.* 2005).

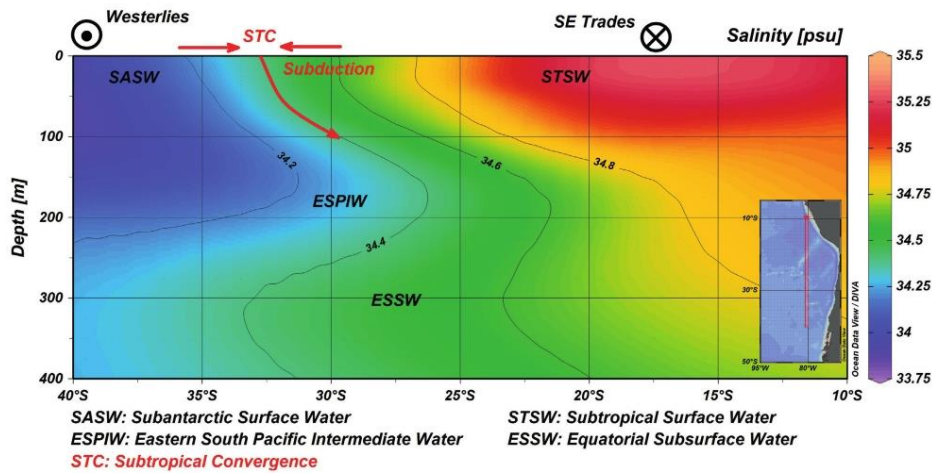


FIGURE 1. Conceptual diagram to illustrate the subduction process at the region of Subtropical Convergence (STC) and the formation of central water masses. The westerly winds cause equatorward Ekman transport (red arrows), whereas Ekman transport produced by the southeast trade winds is poleward. This leads to the creation of STC (30°-35°S) where SASW is subducted and ESPIW is formed by means of Ekman pumping. Salinity through 80°W is shown between 10°-40°S from the surface to 400-m depth. Annual mean salinity data used in this figure were derived from the World Ocean Atlas 2013 (<https://www.nodc.noaa.gov/OC5/woa13/>). / Diagrama conceptual para ilustrar el proceso de subducción en la región de la Convergencia Subtropical (CST) y la formación de masas de agua central. Los vientos del oeste causan un transporte de Ekman hacia el ecuador (flecha roja), mientras que el transporte de Ekman producido por los vientos alisios del sur-este es hacia el polo. Esto conduce al origen de la CST (30°-35°S) donde el SASW es subducida y el ESPIW se forma por medio del bombeo de Ekman. Se muestra la salinidad a lo largo del 80° O, entre 10-40°S desde la superficie a 400 m de profundidad. Para esta figura se usaron datos del promedio anual de salinidad obtenidos de World Ocean Atlas 2013 (<https://www.nodc.noaa.gov/OC5/woa13/>).

The objective of this study was to reevaluate and improve the distribution and geometry of ESPIW using newer information (2007-2012) than used by Schneider *et al.* (2003) (1990-2001). The underlying hypothesis was that intensification of winds in the eastern SP (Weller 2015; England *et al.* 2014) has triggered an increase of wind stress curl and thus ESPIW production. With this aim, this study used data obtained through the Array for Real-Time Geostrophic Oceanography (ARGO) program and its monitoring network, which constitutes a major component of the ocean observation system. The massive dataset comprised over 46,000 profiles obtained during 2007-2012 from an area between the western coast of South America and 152°W, and 5°-40°S. Temporal differences were established for the core features of ESPIW and these were compared with the results obtained by Schneider *et al.* (2003). Finally, differences in water mass properties were related to climate variability and Ekman pumping velocity. This analysis enabled an updated assessment to be made of the distribution, geometry, and salinity of ESPIW.

## MATERIALS AND METHODS

**SALINITY PROFILES OBTAINED FROM ARGO, WOCE AND CIMAR**  
 Approximately 46,000 salinity profiles from Argo were used for this study. All the profiles were obtained within the area from the coast of South America to 150°W, and between 5° and 40°S, from near the surface to 500 dbar. The period of interest was January 2007 to December 2012, and all profiles with a quality indicator of Flag A, N = 100% (all depth levels with reliable information) were employed. The vertical resolution of Argo profiles is variable; it is approximately 10 dbar from the surface to 300 dbar, then it progresses in 20-dbar intervals until 500 dbar. Thus, an updated and improved database was established to characterize the modern geometry of ESPIW compared with the historic data (1990-2001), consisting of 779 CTD profiles, compiled by Schneider *et al.* (2003).

This study also used 66 salinity profiles from the surface to 500 dbar from each WOCE P06 transect conducted in 1993 and 2010. These were obtained from the coast of

South America to 110°W, along latitude 32.5°S (vertical resolution: 2 dbar). Figure 2 shows the study area, and the Argo and WOCE salinity profile distribution. Argo data were obtained from the “USGODAE ARGO GDAC Data Browser” and the WOCE data were acquired from “CLIVAR and Carbon Hydrographic Data Office.” In addition, 10 profiles measured first in 1999 during the CIMAR 5 (Cruceros de Investigación Marina) expedition, conducted by CONA (Comité Oceanográfico Nacional), along 27°35’S between 79°35’W and 92°10’W, and repeated in 2015 (CIMAR 21), were also employed in this study. The accuracies of the temperature, salinity, and pressure sensors on the Argo floats are  $\pm 0.005^{\circ}\text{C}$ ,  $\pm 0.01$  psu, and  $\pm 5$  dbar, respectively (Argo Science Team, 2000). The accuracies of the temperature and salinity data in the WOCE datasets are better than  $0.003^{\circ}\text{C}$  and  $0.003$  psu, respectively (Robertson *et al.* 2002), similar to the CIMAR 21 datasets (Donoso *et al.* 2016).

**ESPIW CORE AND ITS PROPERTIES**

AAIW constitutes an intermediate salinity minimum at depths around 600-800 m, whereas ESPIW represents an upper or shallow salinity minimum at depths around 200 m (e.g. Figure 1 at 80° W). We define the ESPIW core as a layer of certain thickness with salinity that is fresher than AAIW. The presence and thickness of this layer was calculated based on each salinity profile. The layer is located at shallower depths than associated with the salinity minimum of AAIW (Figure 3). The AAIW minimum

salinity was projected toward the surface and it intercepted the area of lesser salinity at shallower depths corresponding to ESPIW (Figure 3). As ESPIW spreads northward ( $<20^{\circ}\text{S}$ ) and westward ( $>90^{\circ}\text{W}$ ) into the SP, its salinity increases to levels slightly higher than AAIW because of vertical isopycnal mixing. Nevertheless, ESPIW remains traceable, first as a relatively shallow salinity minimum and later as a knee-shaped curve in the T-S diagram in the sigma-t range typical of ESPIW.

**TEMPORAL CHANGES IN ESPIW**

The temporal changes in the spatial distribution (upper limit and thickness) and volume of the ESPIW’s core were obtained by comparing modern and historic results in the area between the coast of Chile and 90°W, and 20°-40°S, i.e., where the salinity of ESPIW is less than that of AAIW. The modern data of this geographic area comprised 8,700 ARGO profiles showing the core structure of ESPIW between 2007 and 2012. The historic data of Schneider *et al.* (2003) comprised 149 CTD profiles from 1990-2001. Differences in the extension and salinity of ESPIW were also established throughout the larger study area. Extension is represented by the average salinity of each profile in the density range of  $\sigma_t$  between 25.75 and 26.25  $\text{kg/m}^3$  the sigma-t range estimated for its core. Additionally, ESPIW’s difference in relative location was estimated for 1992 and 2010, represented by the 34.28 isohaline, in each section of the WOCE P06 transect along 32.5°S from the coast of Chile to 110°W.

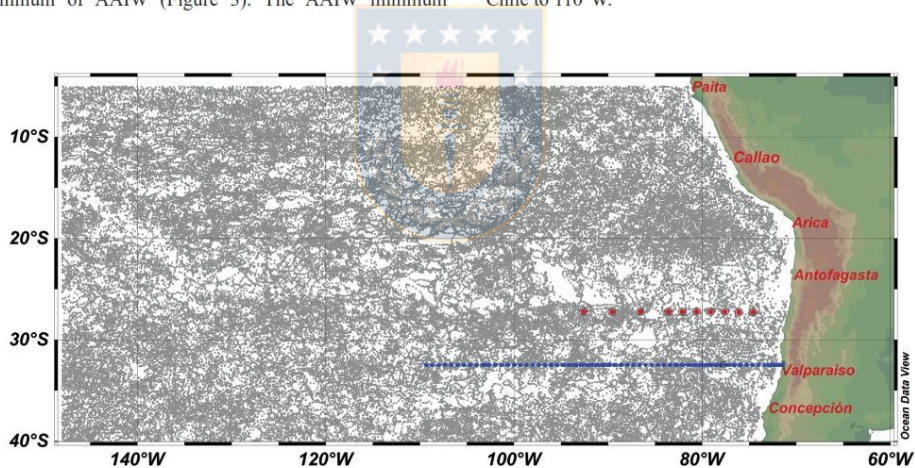


FIGURE 2. Study Area: South Pacific Ocean. Grey dots are Argo profiles obtained during 2007-2012. Blue dots throughout 32°30’S indicate WOCE P06 transect and stations used in this study (first performed in 1993 and repeated in 2010). Red dots throughout 27°S indicate CIMAR 5 transect and stations used in this study (first performed in 1999 and repeated in 2015). / Área de estudio. Océano Pacífico Sur. Puntos grises corresponden a perfiles Argo obtenidos durante 2007-2012. Los puntos azules a lo largo del 32°30’S indican la transecta WOCE P06 y las estaciones usadas en este estudio (realizada primero en 1993 y repetida en 2010). Los puntos rojos a lo largo de 27°S indican la transecta CIMAR 5 y las estaciones usadas en este estudio (realizada primero en 1999 y repetida en 2015).

EKMAN PUMPING VELOCITY

Five sources of monthly mean wind products, representing winds at 10 m above the ocean surface, were used for the computation of Ekman pumping velocity. These comprised satellite derived data: 1) ERS1/2 AMI, provided by IFREMER /CERSAT, and 2) QuikSCAT obtained from Centre d'Exploitation et de Recherche Satellitaire d'Archivage et de Traitement (CERSAT) at the Institut Francais de Recherche pour l'Exploitation de la Mer (IFREMER); and model data: 3) ERA-Interim, 4) Navy Operational Global Atmospheric Prediction System (NOGAPS) model "Fleet Numerical Meteorology and Oceanography Center" (FNMOC), and 5) Reanalysis data from the National Center for Environmental Prediction (NCEP). Details of their resolutions, available periods, and products are listed in Table 1.

Ekman pumping velocity (EP) was calculated according to Tomczak and Godfrey (1994) using the following equation:

$$EP = \frac{\text{Curl}}{\rho_{\text{sea water}} f}; \quad \text{Curl} = \frac{\partial \tau_y}{\partial x} - \frac{\partial \tau_x}{\partial y}, \quad (\text{Equation 1})$$

where  $\rho_{\text{sea water}} = 1023 \text{ kg/m}^3$ , which is the reference density of seawater,  $f$  is the Coriolis parameter ( $f=2 \Omega \sin \varnothing$ , where

$\Omega = 7.29 \times 10^{-5} \text{ (rad/s)}$  is earth's angular velocity and  $\varnothing$  is latitude, and  $\tau_y$  and  $\tau_x$  are the meridional and zonal components of wind stress, respectively. The latter two parameters are calculated from:

$$\tau_y = C_D \rho_{\text{air}} v U_{10} \quad \tau_x = C_D \rho_{\text{air}} u U_{10} \quad (\text{Equation 2})$$

where  $C_D$  is the drag coefficient (0.0013, used in NCEP and ERA Interim reanalysis), also we use wind stress data, which is computed utilising ERS-1, ERS-2 and QuikSCAT observations, and following the recommendations of Smith, (1988) to assign  $C_D$  values of  $1 \times 10^{-3}$  for wind speeds between 2-5 m/s, and  $2 \times 10^{-3}$  for wind speeds up to 24 m/s,  $\rho_{\text{air}}$  is the air density ( $1.2 \text{ kg/m}^3$ ),  $u$  and  $v$  are the zonal and meridional wind components, respectively, and  $U_{10}$  is the magnitude of the wind 10 m above the ocean surface. ERS1/2 AMI, QuikSCAT, and FNOMC already provide the wind stress curl from which the Ekman pumping velocity was calculated.

Linear trends of series of regionally and temporally averaged  $\overline{EP}$  were analyzed for two periods: 1991-2000 and 2000-2012. The first was used by Schneider et al. (2003) for their first estimation of the properties and geometry of ESPIW. Here,  $\overline{EP}$  is the EP average in the region and time

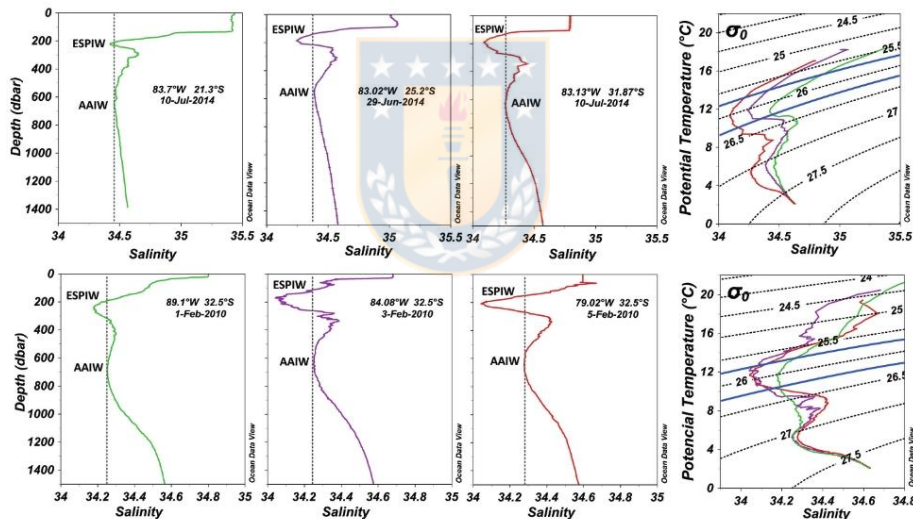


FIGURE 3. Salinity profiles and T-S diagrams. Upper panels: Argo data showing ESPIW core and depicting its meridional variation. Lower panels: WOCE P06 transect data with ESPIW core and depicting its zonal variation. Blue dotted lines in T-S diagrams show ESPIW core limits:  $\sigma_t$  between 25.75 and 26.25  $\text{kg/m}^3$ . / Perfiles de salinidad y diagramas T-S. Panel superior: Datos Argo mostrando el núcleo del ESPIW que representa su variación meridional. Panel inferior: Datos de la transecta WOCE con el núcleo del ESPIW que representa su variación zonal. La línea punteada azul en los diagramas T-S muestra los límites del núcleo del ESPIW:  $\sigma_t$  entre 25,75 y 26,25  $\text{kg/m}^3$ .

of formation of ESPIW, i.e., 82.5°-76°W and 30°-39°S, and August-September, respectively (Karstensen 2004; Luyten et al. 1983; Schneider *et al.* 2003). For each average, 70, 240, 12, 60, and 112 grid points from FNMOC, QuikSCAT, NCEP, ERS, and ERA-Interim, respectively, were used owing to the different horizontal resolutions of the five

databases. The coastal zone was disregarded for favoring upwelling (Letelier *et al.* 2009) and the southern and northern limits were established in relation to the minimum surface salinity values indicating the outcrop region of ESPIW.

TABLE 1. Characteristics of wind products. / Características de los productos de vientos.

SOURCE	PERIOD	RESOLUTION (Longitude × Latitude)	DOWNLOAD SITE	AVAILABLE PRODUCTS
ERS 1/2-AMI	1991-2000	1° × 1°	Ifremer/CERSAT	Zonal and meridional wind components Wind stress
QuikSCAT	2000-2009	0.5° × 0.5°	Centre ERS d'Archivage et de Traitement (CERSAT) ( <a href="http://www.ifremer.fr/cersat/en/index.htm">http://www.ifremer.fr/cersat/en/index.htm</a> )	Zonal and meridional wind components Wind stress and wind stress curl
FNMOC	2000-2012	1° × 1°	<a href="http://coastwatch.pfeg.noaa.gov/erddap/search/index.html?searchFor=erdlasFnWind">http://coastwatch.pfeg.noaa.gov/erddap/search/index.html?searchFor=erdlasFnWind</a>	Zonal and meridional wind components Wind stress and wind stress curl
ERA-Interim	1991-2012	0.75° × 0.75°	<a href="http://apps.ecmwf.int/datasets/data/interim-full-daily/levtype=sfc/">http://apps.ecmwf.int/datasets/data/interim-full-daily/levtype=sfc/</a>	Zonal and meridional wind components
NCEP	1991-2012	2.5° × 2.5°	<a href="https://www.esrl.noaa.gov/psd/data/gridded/data.ncep.reanalysis.htm">https://www.esrl.noaa.gov/psd/data/gridded/data.ncep.reanalysis.htm</a>	Zonal and meridional wind

## RESULTS

### MODERN EXTENSION OF ESPIW AND SALINITY DECREASE

The core of ESPIW, with salinity less than that of AAIW, inhabits the eastern portion of the SP subtropical gyre north of the region of STC and it occupies the depth range of 100-300 m; therefore, it becomes part of the general gyre circulation. Once part of this circulation, ESPIW mixes gradually with overlying Subtropical and underlying Equatorial Subsurface Water, both of which are saltier; thus, it starts to lose its signature feature of being less saline than AAIW (Schneider *et al.* 2003). Nevertheless, it sustains a traceable relative upper salinity minimum in its typical sigma-t density range of 25.75-26.25 kg/m<sup>3</sup>. Figure 3, as an example, shows salinity profiles and T-S diagrams from Argo (above) and WOCE P06 (below), and the spatial variability of the ESPIW core is highlighted in the meridional (above) direction as well as in the zonal (below) direction. In the upper row (meridional from north to south), the profile core thickness of ESPIW diminishes northward from 146 m at 31.87°S to 25 m at 21.33°S, while its upper limit deepens from 130 to 210 m at the same latitudes. The lower row profiles (zonal from west to east) show the ESPIW core thickness varies between 119 and 155 m, and

its upper limit varies between depths of 105 and 191 m. In the T-S diagrams of both rows, the minimum salinities at the lesser depths (ESPIW core) have values in the  $\sigma_t$  range of 25.75-26.25 kg/m<sup>3</sup>.

The geographic pattern of average salinity within this specific density range allows the extension of ESPIW to be traced and the limit of its influence in communicating SASW to intermediate depths of the tropical SP to be determined. This new geographic pattern of average salinity within the ESPIW density range together with the historic pattern is presented in Figure 4. The westward extension of ESPIW is evident in the historic pattern established using the 779 CTD profiles (Schneider *et al.* 2003); however, it is defined with much more reliability in the modern by the incorporation of the 46,000 ARGO profiles. ESPIW can be traced up to 150°W in the tropical SP. Salinity changes in ESPIW were established by comparing the geographic positions of the modern salinity isolines with their historic counterparts. For example, the modern 34.7 isohaline coincides with the historic 34.8 isohaline, and the modern 34.9 isohaline is found overlying the historic 35.0 isohaline. This suggests that a decrease of 0.1 in salinity has occurred over the entire domain (Figure 4). A repeated hydrographic transect, October 1999 and October 2015 (CIMAR 5 and

21), between the coastal Chilean city of Caldera and Easter Island along latitude 27°S crossed ESPIW and showed the very same drop of 0.1 in salinity in the density range of this water mass based on the averages obtained for 2015 and 1999, with standard deviations 0.281 and 0.305 respectively.

TEMPORAL CHANGES IN GEOMETRY OF ESPIW'S CORE

The modern Argo database (2007-2012) allowed an update to the geometry of the ESPIW core, with salinity less than that of the deeper AAIW, in more detail and for a much larger geographic region than in Schneider *et al.* (2003). The newly computed origin of the ESPIW core is represented by the blue line (0-m depth of its upper limit) in Figure 5a. This line represents where subduction begins, i.e., between 100°W and the coast of Chile, and south of 35°S at its western side, and it follows a northeasterly direction toward the coast of South America (30°S). From the origin of subduction, the upper limit of this water mass generally deepens toward the northwest until 325 m, where the core becomes indistinguishable equatorward of 25°S (Figure 5a). In other words, the salinity of ESPIW is higher than AAIW but ESPIW maintains the properties of a relative upper minimum salinity at a shallower depth than AAIW (see Figure 3). Once SASW has been subducted to form ESPIW, it joins the subtropical gyre circulation.

The thickness of the ESPIW core, based on Argo data, varies between 25 and 250 m (Figure 5b). From the subduction line of ESPIW toward the north, its core thickness varies meridionally, diminishing toward the north and fading

at around 15°S, where thicknesses of <25 m were measured. This meridional gradient is more abrupt in the west (100°W) than to the east of 85°W. The core has a thickness of >50 m up to 23°S in the eastern portion; however, the equivalent is only up to 32°S to the west of 85°W. Thus, in the western extreme, the thickness of the core decreases from 250 to 50 m over approximately 3° latitude, whereas it changes from 250 to 100 m over 6° latitude at 85°W. South of the subduction line, by definition, there is no subsurface upper salinity minimum but the surface water nevertheless shows salinities less than AAIW. This is considered not to be ESPIW but SASW instead (Figure 5b inset).

Temporal changes in the upper base, thickness, and volume were analyzed regarding the distribution of the ESPIW core by comparison of the modern results with those obtained by Schneider *et al.* (2003), who used data gathered between the coast of Chile and 90°W, and 20°-38°S from 1990-2000 (red box in Figure 5b). The modern geographic distribution of the core's upper depth, indicated by the contour lines in Figure 5a, was compared with the distribution of the historic upper depth of the core presented by Schneider *et al.* (2003). The modern upper depth of the ESPIW core maintains its distribution in relation to historic recordings (Figure 5a). However, the geographic patterns of the thickness of the core present non-homogenous temporal changes, i.e., a differential increase in thickness illustrated by the movement of the 50 and 100 m contour lines (Figure 5b). Specifically, the 50-m contour is displaced toward the north by about 6° at its western

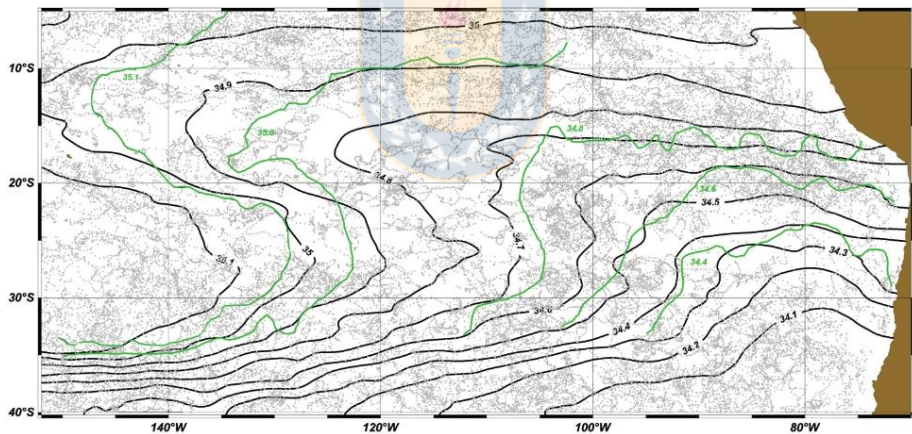


FIGURE 4. ESPIW extension. Contours of average salinity in the  $\sigma_t$  range between 25.75 and 26.25  $\text{kg/m}^3$ . Modern results: black contour lines. Historic results: green contour lines. Approximately 46,000 Argo profiles obtained during 2007-2012 were considered (gray dots). / Extensión del ESPIW. Contornos del promedio de salinidad en el rango de  $\sigma_t$  entre 25,75 y 26,25  $\text{kg/m}^3$ . Resultados actuales: líneas de contornos color negro. Resultados históricos: líneas de contornos de color verde. Se consideraron aproximadamente 46.000 perfiles Argo durante 2007-2012 (puntos grises).

end and by less than 1° at 79°W, whereas further east, the modern 50-m contour coincides with its historic counterpart (Figure 5b). Furthermore, the 100-m thickness contour is displaced toward the north by approximately 3°. The core of ESPIW, with thickness of >25 m, is also present at more equatorward latitudes (≤20°S) not reported by Schneider *et al.* (2003). This indicates an expansion of this water mass toward the north. Variations of the core's geometry have led to a 53% increase in occupied volume. A similar increase was observed in the temporal change of the area occupied by ESPIW (isohaline of 34.28) in repeated hydrographic transects at 32.5°S in January-February 2010 and May 1992. Salinity from the coast to 110°W and from the surface to the depth of 500 m is depicted in Figure 6. The upper salinity limit of ESPIW is characterized by the 34.28 isohaline that delimits the lower salinities that correspond to ESPIW. In 2010, it was deeper by 100 m and it extended almost 10° further west than in 1992, comprising an increase in area of 48%; however, the absolute minimal salinity within the core remained unchanged (Figure 6).

EVOLUTION OF EKMAN PUMPING VELOCITY 1991-2012

Here, we concentrate on establishing the atmospheric variability by means of deduced from the five wind products

analyzed for the historic and modern periods over the ESPIW formation region (30°-39°S, 82.5°-76°W; Figure 5a) during austral winter. During 1991-2000, a decrease in magnitude was observed, as deduced from NCEP, ERA-Interim, and ERS wind products, which was unfavorable for subduction (Figure 7). Conversely, magnitude increased during 2000-2012, favoring subduction (as deduced from NCEP, ERA-Interim, QuikSCAT, and FNMOC wind products) (Figure 7). For NCEP, ERA-Interim, and ERS products, the linear trends of Ekman pumping velocity in the historic period were 0.8, 2.6, and 2.7 m/year per year, respectively, i.e., decreasing by half (please note that Ekman velocity is negative). Most of the historic data used to estimate the geometry of ESPIW were from 1995-2000. In this latter episode, Ekman pumping velocity was about -25 m/year when combining the three wind products. From 2000 onward, Ekman pumping intensified and the 1991 levels were reestablished by 2012; deduced from NCEP, ERA-Interim, QuikSCAT, and FNMOC products, the gains were -1.1, -1.2, -2.7, and -1.0 m/year per year, respectively. The modern dataset for ESPIW analysis consisted of data from 2007-2012. In this period, the mean Ekman pumping velocity amounted to around -35 m/year, i.e., 10 m/year faster than during 1995-2000.

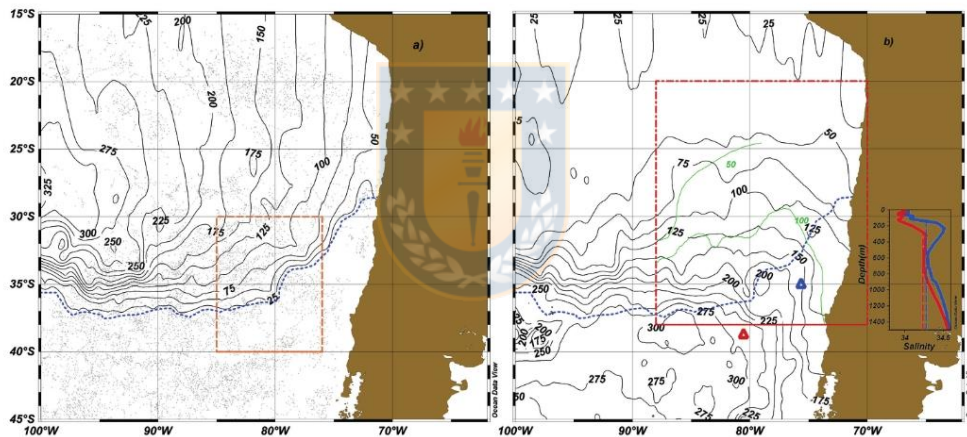


FIGURE 5. Geometry of ESPIW core. a) Depth of upper limit of ESPIW core (m). Gray dots indicate Argo profile positions. Brown rectangle marks ESPIW formation region considered for EP calculation. Dotted blue line shows ESPIW core upper limit 0, where lower salinity water is ready for subduction. b) ESPIW core thickness (m). Modern results (black contour lines) and historic results (green contour lines). Salinity profiles at red and blue triangles (south of the limit of ESPIW) display SASW with less salinity than AAIW, which later forms part of ESPIW; inset in b). / Geometría del núcleo del ESPIW. a) Profundidad del límite superior del ESPIW (m). Los puntos grises indican la posición de los perfiles Argo. El rectángulo café marca la región de formación del ESPIW considerada en el cálculo del EP. La línea punteada azul muestra el límite superior 0 del núcleo del ESPIW, donde el agua de menor salinidad está lista para la subducción. b) Espesor del núcleo del ESPIW (m). Resultados actuales (líneas de color negro) y resultados históricos (líneas de color verde). Perfiles de salinidad en triángulos azul y rojo (al sur del límite del ESPIW) muestra el SASW con menor salinidad que el AAIW, la cual luego forma parte del ESPIW; recuadro en b).

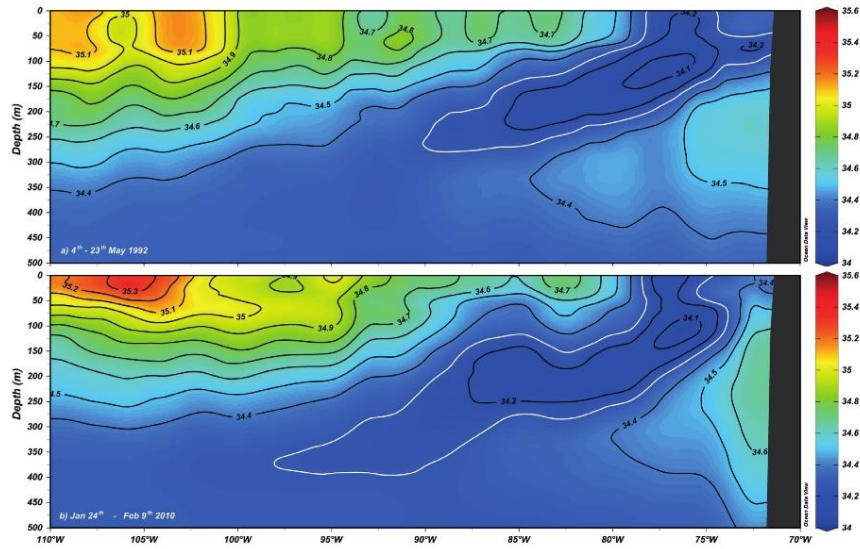


FIGURE 6. Salinity section throughout WOCE P06 transect at 32.5°S: a) 1993 and b) 2010. White contour is 34.28 isohaline, which is the upper limit of the ESPIW core. / Sección de salinidad a lo largo de la transecta WOCE P06 en 32,5°S: a) 1993 y b) 2010. El contorno blanco es la isolinéa de 34,28, la cual es el límite superior del núcleo de ESPIW.

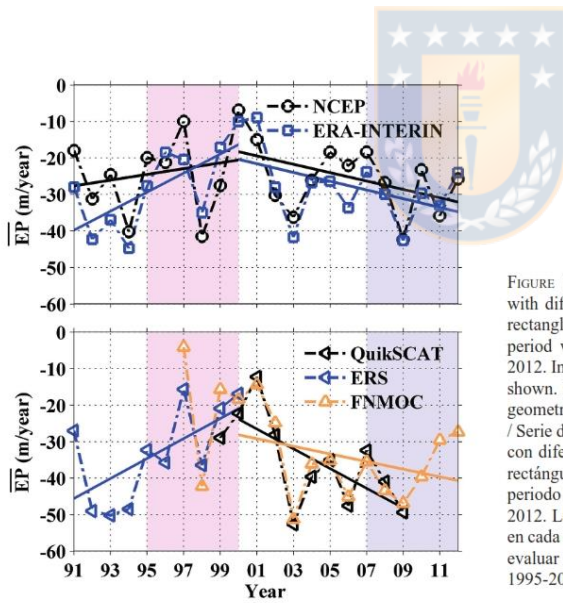


FIGURE 7.  $\overline{EP}$  time series. Based on ESPIW formation region with different wind products within the region (Figure 5, brown rectangle) and formation time (August-September). The total period was divided into two subperiods: 1991-2000 and 2000-2012. In the  $\overline{EP}$  time series of each wind product the linear trend is shown. Most of the data used to evaluate the historic and modern geometry of ESPIW were obtained from 1995-2000 and 2007-2012. / Serie de tiempo  $\overline{EP}$ . Basado en la región de formación del ESPIW con diferentes productos de viento dentro de la región (Figura 5, rectángulo café) y tiempo de formación (agosto-septiembre). El periodo total fue dividido en dos sub-periodos: 1991:2000 y 2000-2012. La tendencia lineal de cada producto de viento es mostrada en cada serie de tiempo de  $\overline{EP}$ . La mayoría de los datos usados para evaluar la geometría del ESPIW fueron obtenidos de los periodos 1995-2000 y 2007-2012.



## DISCUSSION

The ESPIW reduction in salinity could be explained by an increase in the precipitation-evaporation (P-E) balance and/or the presence of less saline water in the region of ESPIW formation, i.e., SASW. Analysis of the P-E balance using ERA-Interim data for the region 42.5°-48.0°S, 76°-85°W (SASW before being subducted) during 2000-2012 revealed only a small nonsignificant positive statistical trend. Analysis based on differences between early Argo and 1990s hydrographic data and changes in sea surface height suggested the circulation of the SP subtropical gyre increased during 1993-2004 (Roemmich *et al.* 2007). This intensification of the gyre circulation reduced salinity in the upper 200 m of the water column in the eastern SP, along 32°30'S by 0.1, via amplified transport of fresher SASW from higher to middle latitudes (Schneider *et al.* 2007). Equatorward transport in the eastern portion of the SP gyre continued to increase through 2014 (Roemmich *et al.* 2016); thus, the supply of fresher SASW toward the region of ESPIW formation could have contributed to the observed drop in ESPIW salinity. General freshening (1950-2008) in the outcrop regions of Pacific Central Water was deduced by Durack and Wijffels (2010), which could explain the freshening of subsurface central water. The ESPIW upper limit of the core maintained the distribution and ranges proposed by Schneider *et al.* (2003), and indicated that the position of the subtropical gyre was sustained despite the strengthening of its circulation during the last two decades (Roemmich *et al.* 2016).

Differences were found in the magnitude and the gain of derived from the five wind products for both 1991-2000 and 2000-2012; however, the patterns (variability and slopes) of their time series were consistent throughout both periods. We attribute the differences in magnitude to the nature of the data (either from models or from satellite-borne scatterometer measurements), validation procedures against different observational data, and to the different horizontal resolutions of the five wind products used.

Change in the Coriolis parameter with latitude and principally, spatio-temporal variations in wind stress affect EP. Our results agree with Ancapichún and Garcés-Vargas (2015), who demonstrated intensification of the Southeast Pacific anticyclone from 2000 onward, which was accompanied by an increase in Ekman pumping along the northern and central coast of Chile. Additionally, the trend of change from 2000 onward matches the beginning of a decade of deceleration in sea surface warming on the global scale, most likely due to an increase of the SP trade winds (England *et al.* 2014). An acceleration of downward EP velocity is favorable for amplified ESPIW formation (Karstensen 2004; Schneider *et al.* 2003; Tsuchiya and Talley 1998), and the  $\overline{EP}$  trend from 2000 onward leads us to the explanation of the increase in volume and area

of ESPIW, which in turn contributed to the ventilation of areas of the SP of intermediate depth. Similarly, Pérez *et al.* (2000) associated variable wind stress curl with variability in the ventilation of North East Atlantic Central Water, while Waugh (2014) associated it with the descent in age of Subantarctic and Subtropical Mode Waters.

This study focused on ESPIW formation and it did not consider interactions proposed by Reid (1973) to explain the occasional presence of ESPIW north of 12°S. Characteristics such as lateral exchanges between water masses brought by the south equatorial current, equatorial countercurrent, and interaction of surface low salinity water north of the equator and high salinity southwest of the equator will be left for future investigations.

## CONCLUSIONS

This study revealed the greater thickness and volume, reduced salinity, and extended area and depth of ESPIW. This could contribute to intermediate depth ventilation, and to increases in the temperature and the sequestration of anthropogenic CO<sub>2</sub> of the interior ocean at the scale of climatic variability. The detected changes were produced during a decade of accelerated trade winds over the Pacific Ocean and a halt of global ocean surface warming initiated in 2000. The findings demonstrate how climate variability immediately affects the formation of oceanic water masses.

## ACKNOWLEDGMENTS

Freddy Hernández thanks the Secretaria de Educación Superior, Ciencia, Tecnología e Innovación (SENESCYT) and the Instituto Oceanográfico de la Armada (INOCAR) del Ecuador for scholarship contract No 20090315. Argo data were collected and made freely available by the International Argo Program and the national programs that contribute to it (<http://www.argo.ucsd.edu>, <http://argo.jcommops.org>). The Argo Program is part of the Global Ocean Observing System. WOCE data were obtained from the CLIVAR and Carbon Hydrographic Data Office (<https://cchdo.ucsd.edu/>). In addition, profiles measured during the CIMAR 5 and 21 (Cruceros de Investigación Marina) expeditions conducted by CONA (Comité Oceanográfico Nacional) were employed in this study.

## REFERENCES

- ANCAPICHÚN, S., GARCÉS-VARGAS, J. 2015. Variability of the Southeast Pacific Subtropical Anticyclone and its impact on sea surface temperature off north-central Chile.

- Ciencias Marinas 41: 1-20. doi: <http://dx.doi.org/10.7773/cm.v41i1.2338>.
- ARGO SCIENCE TEAM 2000. Report of the Argo Science Team Second Meeting. Proc. Argo Science Team Second Meeting, Southampton Oceanography Centre, Southampton, U.K., 35 pp.
- BAKUN, A. 1990. Global climate change and intensification of coastal ocean upwelling. *Science* 247(4939): 198-201. doi: 10.1126/science.247.4939.198.
- CARBON HYDROGRAPHIC DATA OFFICE. 2015. URL: <https://cchdo.ucsd.edu/> (Accessed: January 15, 2015).
- CHEN, H.C., SUI, C.H., TSENG, Y.H., HUANG, B.H. 2015. An analysis of the linkage of Pacific subtropical cells with the recharge-discharge processes in ENSO evolution. *Journal of Climate* 28: 3786-3805.
- CHERESKIN, T.K., PRICE, J.F. 2009. Ekman transport and pumping. In: Steele, J., Thorpe, S., Turekian, K. (Eds) *Encyclopedia of Ocean Sciences*. Academic Press.
- DONOSO, D., HERNANDEZ, F., NAVARRO, E., SCHNEIDER, W. 2016. Cambio de las propiedades hidrográficas en la columna de agua entre Caldera e Isla de Pascua (2015-1999). Taller de resultados preliminares Crucero CIMAR 21 "Islas Océánicas" 22 de noviembre de 2016 Valparaiso, Chile.
- DURACK, P.J., WUFFELS, S.E. 2010. Fifty-year trends in global ocean salinities and their relationship to broad-scale warming. *Journal of Climate* 23: 4342-4362. doi: 10.1175/2010JCLI3377.1.
- EMERY, W.J., MEINCKE, J. 1986. Global water masses: summary and review. *Oceanologica Acta* 9: 383-391.
- ENGLAND, M.H., MCGREGOR, S., SPENCE, P., MEEHL, G.A., TIMMERMANN, A., CAI, W., GUPTA, A.S., MCPHADEN, M.J., PURICH, A., SANTOSO, A. 2014. Recent intensification of wind-driven circulation in the Pacific and the ongoing warming hiatus. *Nature Climate Change* 4: 222-227. doi: 10.1038/nclimate2106.
- KARSTENSEN, J. 2004. Formation of the South Pacific shallow salinity minimum: A Southern Ocean pathway to the tropical Pacific. *Journal of Physical Oceanography* 34: 2398-2412.
- LETELIER, J., PIZARRO, O., NUÑEZ, S. 2009. Seasonal variability of coastal upwelling and the upwelling front of central Chile. *Journal of Geophysical Research* 114. doi: 10.1029/2008JC005171.
- LIU, C.Y., WANG, Z.M., LI, B.R., CHENG, C., XIA, R.B. 2017. On the response of subduction in the South Pacific to an intensification of westerlies and heat flux in an eddy permitting ocean model. *Advances in Atmospheric Sciences* 34: 521-531.
- LIU, L.L., HUANG, R.X. 2012. The global subduction/obduction rates: Their interannual and decadal variability. *Journal of Climate* 25: 1096-1115. doi: 10.1175/2011JCLI4228.1.
- LUYTEN, J.R., PEDLOSKY, J., STOMMEL, H. 1983. The ventilated thermocline. *Journal of Physical Oceanography* 13: 292-309.
- MCCREARY JR., J.P., LU, P. (1994). Interaction between the subtropical and equatorial ocean circulations: The subtropical cell. *Journal of Physical Oceanography* 24(2): 466-497.
- PÉREZ, F.F., POLLARD, R.T., READ, J.F., VALENCIA, V., CABANAS, J.M. 2000. Climatological coupling of the thermohaline decadal changes in Central Water of the Eastern North Atlantic. *Scientia Marina* 64(3): 347-353.
- REID, J.L. 1973. The shallow salinity minima of the Pacific Ocean. *Deep Sea Research and Oceanographic Abstracts* 20: 51-68.
- ROBERTSON, R., VISBECK, M., GORDON, A., FAHRBACH, E. 2002. Long-term temperature trends in the deep waters of the Weddell Sea. *Deep Sea Research Part II* 49: 4791-4806.
- ROEMMICH, D., GILSON, J., DAVIS, R., SUTTON, P., WUFFELS, S., RISER, S. 2007. Decadal spinup of the South Pacific subtropical gyre. *Journal of Physical Oceanography* 37: 162-173. doi: 10.1175/JPO3004.1.
- ROEMMICH, D., GILSON, J., SUTTON, P., ZILBERMAN, N. 2016. Multidecadal change of the South Pacific Gyre circulation. *Journal of Physical Oceanography* 46: 1871-1883. doi: 10.1175/JPO-D-15-0237.1.
- SCHNEIDER, W., FUENZALIDA, R., RODRÍGUEZ-RUBIO, E. 2003. Characteristics and formation of Eastern South Pacific Intermediate Water. *Geophysical Research Letters* 30(11): 1581.
- SCHNEIDER, W., FUKASAWA, M., GARCÉS-VARGAS, J., BRAVO, L., UCHIDA, H., KAWANO, T., FUENZALIDA, R. 2007. Spin-up of South Pacific subtropical gyre freshens and cools the upper layer of the eastern South Pacific Ocean. *Geophysical Research Letters* 34: L24606. doi:10.1029/2007/GL031933.
- SCHNEIDER, W., FUKASAWA, M., UCHIDA, H., KAWANO, T., KANEKO, I., FUENZALIDA, R. (2005). Observed property changes in eastern South Pacific Antarctic Intermediate Water. *Geophysical Research Letters* 32: 1-4. doi: 10.1029/2005GL022801.
- SMITH, S.D. 1988. Coefficients for sea surface wind stress, heat flux, and wind profiles as a function of wind speed and temperature. *Journal of Geophysical Research: Oceans* 93(C12): 15467-15472.
- SPRINTALL, J., TOMCZAK, M. 1993. On the formation of central water and thermocline ventilation in the southern hemisphere. *Deep Sea Research, Part I-Oceanographic Research Papers* 40: 827-848.
- STOMMEL, H. 1979. Determination of water mass properties of water pumped down from the Ekman layer to the geostrophic flow below. *Proceedings of the National Academy of Sciences of the United States of America* 76(7): 3051-3055.
- STRAMMA, L., PETERSON, R.G., TOMCZAK, M. 1995. The South Pacific Current. *Journal of Physical Oceanography* 25(1): 77-91.
- TALLEY, L.D. 1999. Some aspects of ocean heat transport by the shallow, intermediate, and deep overturning circulations. Mechanisms of global climate change at millennial time scales. En: Clark, P.U., Webb, R.S., Keigwin, L.D. (Eds) *American Geophysical Union, Washington, D.C.* doi: 10.1029/GM112p0001.
- TALLEY, L.D., PICKARD, G., EMERY, W.J., SWIFT, J.H. 2011. *Physical Oceanography: An Introduction*. Elsevier Science & Technology, UK.
- TOMCZAK, M., GODFREY, J.S. 1994. *Regional Oceanography: An Introduction*, Pergamon, UK. 422 pp.
- TSUCHIYA, M., TALLEY, L.D. 1998. A Pacific hydrographic section at 88°W: Water-property distribution. *Journal of Geophysical*

- Research 103: 12,899-12,918.
- USGODAE Argo GDAC Data Browser. URL [http://www.usgodae.org/cgi-bin/argo\\_select.pl](http://www.usgodae.org/cgi-bin/argo_select.pl) (Accessed: May 5, 2015).
- WAUGH, D.W. 2014. Changes in the ventilation of the southern oceans. *Philosophical Transactions of the Royal Society of London A: Mathematical, Physical and Engineering Sciences* 372(2019): 20130269.
- WELLER, R.A. 2015. Variability and trends in surface meteorology and air-sea fluxes at a site off northern Chile. *Journal of Climate* 28: 3004-3023. doi: 10.1175/JCLI-D-14-00591.1.



4.2 Capítulo 2: Efectos de ENOS sobre las condiciones oceanográficas físicas en el Sistema de Corrientes de Humboldt.

Hydrology Submitted: 2020-01-30. Status: Decision pending. Manuscript ID: hydrology-721767

ENSO Effects on the Humboldt Current System's Physical Oceanographic Conditions

Freddy Hernandez Vaca<sup>1,2,3</sup> and Wolfgang Schneider<sup>3,4\*</sup>

<sup>1</sup> Programa de Postgrado en Oceanografía, Facultad de Ciencias Naturales y Oceanográficas, Universidad de Concepción, Casilla 160-C, Concepción, Chile

<sup>2</sup> Dirección Oceanografía Naval, Instituto Oceanográfico de la Armada. 5940 Guayaquil, Ecuador

<sup>3</sup> Instituto Milenio de Oceanografía (IMO), Universidad de Concepción. Casilla 1313, Concepción, Chile

<sup>4</sup> Departamento de Oceanografía, Universidad de Concepción, Concepción, Víctor Lamas 1290, 4070043 Concepción, Chile

\* Correspondence: [wshneid@udec.cl](mailto:wshneid@udec.cl); Tel.: +56-41-2661235



1 Article

## 2 ENSO Effects on the Humboldt Current System's 3 Physical Oceanographic Conditions

4 Freddy Hernández-Vaca <sup>1,2,3</sup> and Wolfgang Schneider <sup>3,4\*</sup>

5 <sup>1</sup> Programa de Postgrado en Oceanografía, Facultad de Ciencias Naturales y Oceanográficas, Universidad  
6 de Concepción, Casilla 160-C, Concepción, Chile

7 <sup>2</sup> Dirección Oceanografía Naval, Instituto Oceanográfico de la Armada. 5940 Guayaquil, Ecuador

8 <sup>3</sup> Instituto Milenio de Oceanografía (IMO), Universidad de Concepción. Casilla 1313, Concepción, Chile

9 <sup>4</sup> Departamento de Oceanografía, Universidad de Concepción, Concepción, Víctor Lamas 1290, 4070043  
10 Concepción, Chile

11 \* Correspondence: wschneid@udec.cl; Tel.: +56-41-2661235

12 Received: date; Accepted: date; Published: date

13  
14 **Abstract:** This study determined the impact of ENSO on the Humboldt Current System (HCS). Sea  
15 surface temperature (SST), near surface wind components, absolute dynamic topography (ADT),  
16 geostrophic velocity components, and eddy kinetic energy (EKE) were examined for the HCS, for  
17 the period 1993–2016. Composite maps of the original or derived ocean surface variables or their  
18 respective anomalies were constructed for the whole time series and separately for El Niño and La  
19 Niña episodes that fell into this time window. A total of 7 El Niño and 7 La Niña events,  
20 independent of individual strength, season and duration, were identified according to the Oceanic  
21 Niño Index. During El Niño events, SST and the upper 40 m of the water column were 0.6°C  
22 warmer and ADT was about 5 cm higher than during La Niña events. Equatorward and upwelling  
23 favorable winds intensified during La Niña events but were weaker during El Niño events, thus  
24 increasing and decreasing coastal upwelling in the former and latter events, respectively. Further,  
25 the mean meridional component of geostrophic velocity, averaged for the HCS, was about 20%  
26 stronger during La Niña events than during El Niño events. This resulted in increased EKE during  
27 La Niña episodes.

28 **Keywords:** ENSO, Humboldt Current System, Eastern Boundary Upwelling System, ARGO,  
29 CIMAR  
30

### 31 1. Introduction

32 The **El Niño Southern Oscillation** (ENSO) is one of the most prominent natural fluctuations  
33 modifying the climate of the equatorial Pacific on a timescale of several years, consisting of  
34 anomalously warm (El Niño) and cold (La Niña) phases (e.g. [1]). ENSO events manifest themselves  
35 in anomalies of sea surface temperature (SST) and upper ocean temperature in the central and  
36 eastern tropical Pacific. Positive anomalies are forced by westerly wind bursts, allowing eastward  
37 displacement of the Indonesian warm water pool by means of equatorial trapped Kelvin waves,  
38 whereas cold events are attributed to enhanced equatorial upwelling caused by stronger than  
39 normal trade winds [2]. El Niño and La Niña are linked to major changes in the atmosphere known  
40 as the Southern Oscillation, “a global-scale seesaw in atmospheric sea level pressure involving  
41 exchanges of air between eastern and western hemispheres centered in tropical and subtropical  
42 latitudes with centers of action located over Indonesia and the tropical South Pacific Ocean (near  
43 Tahiti)” [3]. The Southern Oscillation Index, which uses the difference in air pressure anomalies

44 between Tahiti and Darwin, measures the strength of the Southern Oscillation; a positive (negative)  
45 index indicates La Niña (El Niño) conditions [3].

46 Both, the warm and cold phases of ENSO are accompanied, among others, by changes in the  
47 positions of the Intertropical and the South Pacific Convergence zones [4], which imply  
48 modifications of the usual rainfall patterns. El Niño episodes typically reduce or even bring  
49 precipitation to a halt in countries bordering the western tropical Pacific and subtropical South  
50 Pacific, whereas their eastern counterparts experience enhanced rainfall [5]. During La Niña events,  
51 this pattern is basically reversed, but the change in tropical Pacific rainfall is both more intense and  
52 more expansive for a unit change in warm SST forcing than that in cold SST forcing [6]. Extensive  
53 areas of the contiguous U.S. experienced extreme seasonal anomalies in precipitation and  
54 temperature during the 1997/98 El Niño [7]. Furthermore ENSO events influence SST outside the  
55 tropical Pacific: "SSTs in the tropical North Atlantic, South China Sea, and Indian Ocean are warmer  
56 (cooler) than normal approximately 3–6 months after the peak warming (cooling) of SSTs in the  
57 central equatorial Pacific" [8].

58 El Niño events are also known to affect zooplankton communities. During the last six decades,  
59 total mesozooplankton carbon biomass was only modestly affected during El Niño episodes in the  
60 southern sector of the California Current System; however, the community composition changed  
61 substantially, although zooplankton responses differed from event to event [9]. Both total  
62 zooplankton and krill abundance dramatically declined in the summer of 1997 in Monterey Bay,  
63 California, when SSTs rapidly increased in response to the strong 1997/98 El Niño event [10]. At the  
64 end of this event, the anchovy biomass in Peruvian waters, estimated at 1.2 million tons in  
65 September 1998, was the lowest throughout the 1990s, whereas the sardine biomass increased [11].  
66 The growth of juvenile and adult anchovy slowed during the 1982/83 El Niño in the northern  
67 anchovy habitat off southern California, but the stock seemingly recovered in 1985 [12].

68 The Humboldt Current is observed inside the geographic region of the southern hemisphere,  
69 where El Niño and La Niña events originate. The equatorward flowing Humboldt Current (HC)  
70 constitutes the eastern boundary current of the South Pacific subtropical gyre, and is sometimes also  
71 referred to as the Peru/Chile Current, Peru Current, or Chile-Peru Current [2,13–16]. This current  
72 initiates at around 38–40°S owing to the northward branch of a bifurcation of the eastward flowing  
73 South Pacific Current when approaching the coast of Chile [17–19]. The current has a mean flow in  
74 the order of 6 cm s<sup>-1</sup>, with a narrow jet-like stream of about 250 km width exceeding 15 cm s<sup>-1</sup> [16,19].  
75 It is located less than 200 km offshore at its southern origin (76°W) from where it streams northward,  
76 deflecting a few degrees to the west (79°W), and thus, increasing its distance from the Chilean coast  
77 [19]. A bifurcation occurs at 23°S, thereby creating a more coastal branch heading towards the coast  
78 of southern Peru (15°S) and an oceanic branch, continuing in a northwesterly direction, which is well  
79 defined beyond 20°S and 85°W [19].

80 The generation of this current can be attributed to the regional wind stress and wind stress curl  
81 [20]. The wind regime in the subtropical eastern South Pacific Ocean is mainly controlled by the  
82 seasonally and meridionally meandering South Pacific High, a permanent, counter-clockwise  
83 spinning atmospheric pressure system centered in the eastern South Pacific at 26–30°S and 85–95°W  
84 during late austral fall and winter, and at 33–36°S and 100–108°W during austral spring and summer  
85 [15,21,22]. Winds east of the South Pacific High and along the entire coast of Chile are equatorward,  
86 parallel to the coast, and therefore favorable for wind driven coastal upwelling [15,19,23].  
87 Furthermore, they lead to the formation of one of the major eastern boundary upwelling systems  
88 (EBUS), namely the Humboldt upwelling system [24] which, like all EBUS, is among the most  
89 productive oceanic areas in the world [25,26]. Wind driven upwelling of colder water from below  
90 enriches the sunlit upper water column with nutrients, thus stimulating primary and higher level  
91 biological productions [27]. Coastal upwelling in conjunction with the Humboldt Current is  
92 associated with the formation of filaments, density fronts, and eddies [20]. These colder and  
93 nutrient-enriched eddies have a typical diameter of 30 km or more and travel seaward [28] up to 500  
94 km offshore [29], thus conveying coastal ecosystems offshore and inserting them into the Humboldt  
95 Current. Dynamics of coastal upwelling and those of the Humboldt Current are therefore

96 linked/coupled to each other and have to be considered as a whole. We adopt the terminology  
 97 introduced by Escribano and Morales [30], among others, and refer to the geographic region  
 98 between 20–40°S and the coast of Chile and the 85<sup>th</sup> meridional West to the Chilean portion of the  
 99 **Humboldt Current System** (HCS, Figure 1); the northern sub-region of the HCS is composed by the  
 100 Peru portion (5–18°S). The HCS off central Chile, furthermore, plays an important role in the  
 101 country's total fish landings including horse mackerel, anchovy, sardines, and Chilean hake [30–32].  
 102 For the purpose of convenience, hereinafter, the Chilean portion of the HCS is simply referred to as  
 103 HCS.

104 Seasonal and inter-annual variability of the wind field over the HCS alter the dynamics of the  
 105 Humboldt Current and coastal upwelling as well. Increased wind stress and wind stress curl during  
 106 austral summers intensified the Humboldt Current by 3 cm s<sup>-1</sup> [19]. Significantly intensified  
 107 upwelling favorable winds reduced diatom abundance and primary production rates in the  
 108 southern HCS during early spring (October–November) in 2009–2013, although a sustained fresh  
 109 water river discharge also contributed to the reduction [26]. The wind field over the HCS is also  
 110 altered during ENSO events by means of air pressure modulations.

111 Harrison and Larkin [7] and Larkin and Harrison [33], among others, investigated ENSO's  
 112 impact on SST and near surface wind outside the equatorial Pacific on a near global scale for the  
 113 years 1946–1995. The authors showed that significantly warm SST anomalies occurred along the  
 114 Pacific coast of South America from the equator to 12°S during the peak of El Niño composites and  
 115 travelled further south. Almost no significant anomalies of alongshore wind could be found. The  
 116 data set available at this time, COADS (Comprehensive Ocean-Atmosphere Data Set), had a course  
 117 resolution of 2° × 2° in latitude and longitude, the accuracy of the SST (wind) signals was in the order  
 118 of magnitude of 0.5 °C (0.5 m s<sup>-1</sup>), and data coverage was sparse; the tropics and southern  
 119 hemisphere typically had extremely limited data. With advanced remote sensing techniques, new  
 120 ocean profilers, increased in-situ ocean observations, and modeling efforts, high-resolution (in space  
 121 and time) global data sets of sea surface variables together with hydrographic data have been made  
 122 available for re-assessing the impact of ENSO events on the HCS since 1993. This study investigated  
 123 SST, absolute dynamic topography (ADT) of the ocean, wind, geostrophic velocity, and eddy kinetic  
 124 energy, and analyzed the temperature of the upper water column. Our analysis showed that the  
 125 values of these variables were significantly different during the warm and cold phases of ENSO.

## 126 2. Data and Methods

127 The data used in this study were acquired from several sources. The **Oceanic Niño Index (ONI)**  
 128 is a 3 month running mean of Extended Reconstructed Sea Surface Temperature (ERSST.v5)  
 129 anomalies in the Niño 3.4 region (5°N–5°S, 120°–170°W), based on centered 30-year base periods  
 130 updated every 5 years. An ONI value of above (below) the +0.5 °C (- 0.5°C) threshold for at least 5  
 131 consecutive months corresponds to an El Niño (La Niña) event (National Oceanic and Atmospheric  
 132 Administration, NOAA). ONI data from 1993 to 2016 were extracted from the NOAA website  
 133 [http://origin.cpc.ncep.noaa.gov/products/analysis\\_monitoring/ensostuff/ONI\\_v5.php](http://origin.cpc.ncep.noaa.gov/products/analysis_monitoring/ensostuff/ONI_v5.php) (accessed 16th  
 134 May 2018). The main contributions to ERSST stem from the International Comprehensive  
 135 Ocean-Atmosphere Data Set (ICOADS) and include measurements made from ships as well as  
 136 moored and drifting buoys, among others.

137 **SST and near surface winds** above the ocean were obtained from the website of the European  
 138 Center Medium Weather Forecast ERA (ECMWF Re-Analysis) Interim reanalysis project, a global  
 139 atmospheric reanalysis since 1979 that has been continuously updated in real time [34]:  
 140 <https://www.ecmwf.int/en/forecasts/datasets/archive-datasets/reanalysis-datasets/era-interim>.  
 141 Monthly means from January 1993 to December 2016 with a horizontal resolution of 0.4° Longitude  
 142 and 0.4° Latitude were employed.

143 The meridional and zonal components of the wind stress,  $\tau_y, \tau_x$ , respectively, were computed  
 144 according to [35]

$$145 \tau_y = C_D \rho_{air} v U_{10} \quad (1)$$

$$146 \tau_x = C_D \rho_{air} u U_{10} \quad (2)$$

147 where  $C_D$  is a constant drag coefficient (0.0013),  $\rho_{air}$  is air density (1.2 kg/m<sup>3</sup>),  $u$  and  $v$  are the  
 148 zonal and meridional wind components 10 m above the ocean, and  $U_{10}$  is the corresponding wind  
 149 magnitude. The wind stress curl is given by  
 150

$$151 \text{ Rotor} = \frac{\partial \tau_y}{\partial x} - \frac{\partial \tau_x}{\partial y} \quad (3)$$

152 ADT and **geostrophic velocities** for the global ocean were obtained via the website of the  
 153 Copernicus Marine Environmental Monitoring Service (CMEMS): <http://marine.copernicus.eu>.  
 154 These products are built upon multi-mission sea surface height measurements including altimeter  
 155 missions Jason-3, Sentinel-3A, HY-2A, Saral/AltiKa, Cryosat-2, Jason-2, Jason-1, T/P, ENVISAT,  
 156 GFO, and ERS1/2. The underlying methodology for generating the merged gridded products relies  
 157 on the optimal interpolation technique; for details please refer to [36]. Daily means from January  
 158 1993 to December 2016 with a horizontal resolution of 0.25° Longitude and 0.25° Latitude were  
 159 employed.

160 Daily means of **eddy kinetic energy (EKE)**, per unit of mass, were calculated according to  
 161 equation (4) (Ref):

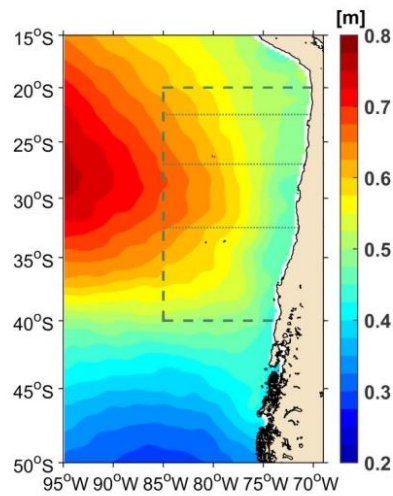
$$162 \text{ EKE} = \frac{1}{2} \times (u'^2 + v'^2) \quad (4)$$

163 where  $u' = u - \bar{u}$ , and  $v' = v - \bar{v}$ , with  $u, v$ , being the daily means of the zonal and  
 164 meridional geostrophic velocity components of the current day, and  $\bar{u}, \bar{v}$ , correspond to the  
 165 climatological monthly mean, with respect to the 1993–2016 period.  
 166

167 **Ocean temperature** and salinity of the upper 2000 m of the water column is routinely  
 168 monitored by the international Argo program based on nearly 3800 free-drifting profiling floats  
 169 deployed in the world ocean since the early 2000s ([www.argo.ucsd.edu](http://www.argo.ucsd.edu)). Temperature and salinity  
 170 measured by Argo floats were first compiled to a monthly mean 1° × 1° gridded global data set by  
 171 [37]. The new version of the Roemmich-Gilson Argo Climatology extended this analysis through  
 172 2017. The data are freely available at [sio-argo.ucsd.edu/RG\\_Climatology.html](http://sio-argo.ucsd.edu/RG_Climatology.html); ocean temperature  
 173 data of the upper 100 m of the water column were used in this study. Upper ocean temperature from  
 174 two research cruises, CIMAR 5 (Cruceros de Investigación Científica Marina en Áreas Remotas) and  
 175 CIMAR 21, in 1999 (13 October–12 November) and 2015 (12 October–11 November), respectively,  
 176 both along 27° S, from near the coast of Chile to Easter Island, comprising 13 hydrographic casts  
 177 between 70.94° W (close to the coast) and 86.55° W (about 1500 km into the open ocean), were also  
 178 incorporated in this study.  
 179

180 In this study, SST, near surface wind components, ADT, geostrophic velocity components, and  
 181 eddy kinetic energy were examined for the HCS, the eastern boundary current system belonging to  
 182 the South Pacific subtropical gyre [19], for the years 1993 to 2016 with respect to the warm and cold  
 183 ENSO phases [33]. The equatorward flowing Humboldt Current was geographically defined  
 184 through visual inspection of the gradients, especially the zonal ones, in the pattern of long-term  
 185 ADT, and confined by the 20<sup>th</sup> and 40<sup>th</sup> southern parallels in the coast of Chile and the 85<sup>th</sup> meridional  
 186 West. The pattern of ADT for the eastern South Pacific Ocean is shown in Figure 1; sharper zonal  
 187 gradients refer to stronger meridional currents. Composite maps of the above introduced original or  
 188 derived ocean surface variables or their respective anomalies derived from 1993–2016 climatological  
 189 monthly means were constructed for the entire time series, and separately for El Niño and La Niña  
 190 episodes that fell into this time window. A total of 7 El Niño and 7 La Niña events, independent of  
 191 individual strength, season, and duration, were identified according to ONI and are listed in Table 1.  
 192 The composite El Niño and La Niña periods were 70 and 83 months, respectively.  
 193





194  
195

196 **Figure 1.** Mean (1993–2016) absolute dynamic topography for the eastern South Pacific. ADT is color  
197 coded according to the colorbar displayed on the right hand side (in meters). The dashed rectangle  
198 marks the Humboldt Current region as defined in this paper. The top and lower, from north to south,  
199 dotted zonal lines mark the location of upper ocean temperature data used in this study from the  
200 Roemmich-Gilson gridded Argo data set and the middle line the track of the CIMAR 5 and 21  
201 hydrographic transects employed here.

202 **Table 1.** El Niño and La Niña periods for which composites of hydrographic variables were  
203 computed. Strength of ENSO events (NOAA): W = weak (0.5 to 0.9°C positive or negative SST  
204 anomaly), M = moderate (1.0 to 1.4°C), S = strong (1.5 to 1.9°C), VS = very strong ( $\geq 2.0^\circ\text{C}$ )

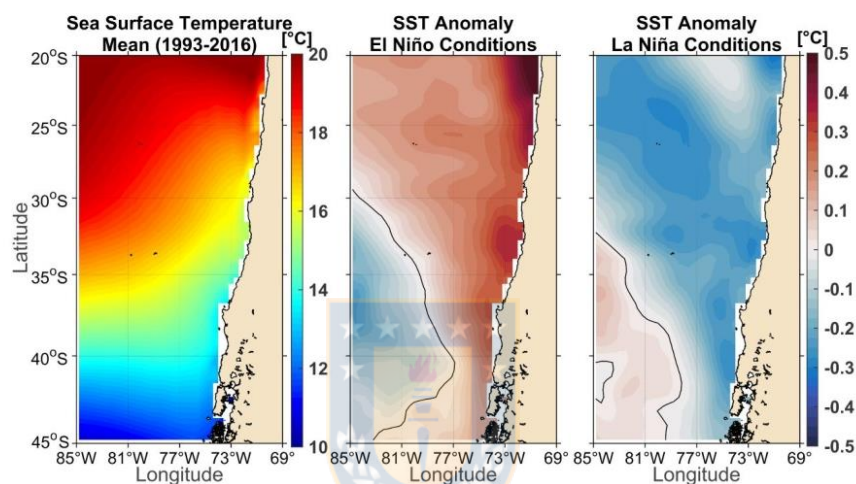
205

El Niño			La Niña		
Month/Year	Month/Year	Duration	Month/Year	Month/Year	Duration
Start	End	Month (Strength)	Start	End	Month (Strength)
Sep/1994	Mar/1995	7 (W)	Aug/1995	Mar/1996	8 (W)
May/1997	May/1998	13 (VS)	Jul/1998	Feb/2001	32 (M-S)
Jun/2002	Feb/2003	9 (M)	Nov/2005	Mar/2006	5 (W)
Jul/2004	Feb/2005	8 (W)	Jul/2007	Jun/2008	12 (M)
Sep/2006	Jan/2007	5 (W)	Jun/2010	May/2011	12 (S)
Jul/2009	Mar/2010	9 (M)	Jul/2011	Mar/2012	9 (W-M)
Nov/2014	May/2016	19 (VS)	Aug/2016	Dec/2016	5 (W)

206

### 207 3. Results and Discussion

208 Long-term mean (1993–2016) SST for the region occupied by the HCS was in general  
 209 characterized by a gradual increase in temperature from the sub polar (12°C) to the tropical zone  
 210 (20°C) with colder temperatures extending farther north along the coast of Chile and about 400 nm  
 211 offshore, thereby also introducing a zonal gradient north of 40° S (Figure 2, left panel). These waters  
 212 were earlier labeled Eastern South Pacific Transition Water by Emery and Meincke [38] and  
 213 consisted of warmer Subtropical Water (STW) in the north and colder Subantarctic Water (SAAW) in  
 214 the south with differential temperatures owing to greater solar radiation occurring in the subtropical  
 215 zone [39]. These two climatic zones were connected by the Humboldt Current, which transported  
 216 SAAW equatorward [18]. The current's influence was more pronounced in the coastal transition  
 217 zone, thus acting as one of the two drivers responsible for the observed zonal SST gradients. The  
 218 second driver that contributed to the cross-shore SST gradients was coastal upwelling offshore  
 219 central-south Chile, which generated upwelling fronts that separated colder coastal waters from  
 220 warmer offshore subtropical waters [40].



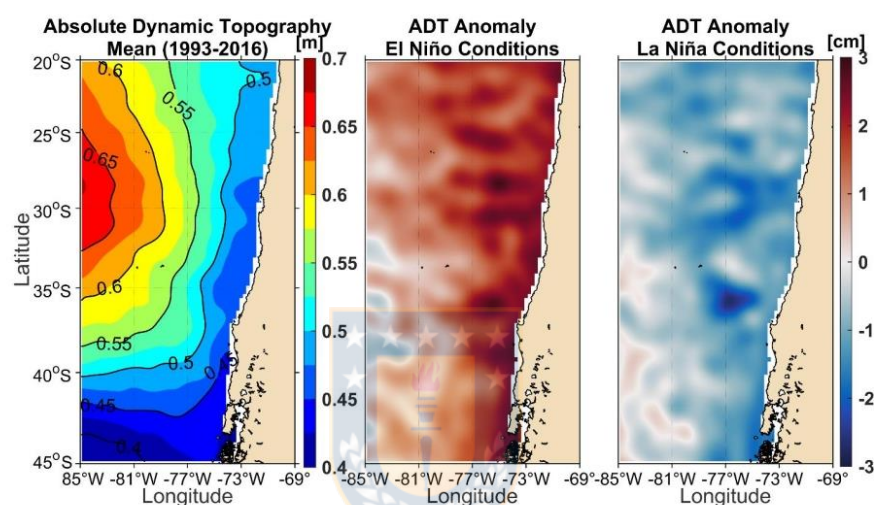
221

222 **Figure 2.** Left panel) Color contoured long-term mean SST; Center panel) Color contoured composite  
 223 of SST anomalies for El Niño scenarios and right panel) for La Niña scenarios. The color bar on the  
 224 right hand side of the figure applies to the center and right panels.

225 SST was up to 0.5°C warmer in most of the HCS region during **El Niño conditions**, except for  
 226 its southwestern corner (SST 0.0–0.2°C cooler than on average, Figure 2 center panel), where the gyre  
 227 circulation was mostly zonal, towards the coast of Chile, before turning north and feeding the  
 228 Humboldt Current. Warm SST anomalies were more pronounced along the coast and were the  
 229 highest in the tropical sector off northern Chile, thus reducing the zonal SST gradients and the  
 230 magnitude of these temperature fronts in the coastal transition zone off Chile (from the coast to  
 231 about 800 km offshore [41]). SST anomalies were predominantly slightly negative (0.2–0.3°C) when  
 232 **La Niña conditions** prevailed, except in the lower left corner of the study area, where the anomalies  
 233 were reversed as during El Niño events, and the SST anomalies were positive in the order of 0.1°C  
 234 (Figure 2 right panel). Negative SST anomalies appeared primarily along the coast, somewhat  
 235 increasing cross-shore fronts, and these negative anomalies followed the path of the Humboldt  
 236 Current (Figure 1).

237 The contours of mean (1993–2016) ADT in the HCS were mainly oriented towards the  
 238 south–north direction, from which the equatorward flowing Humboldt Current could be inferred;  
 239 the denser the contours, the stronger the current (Figure 3 left panel). The current initiated

240 somewhat south of 40°S as a product of the northward bifurcation branch of the South Pacific  
 241 Current as reported earlier. A persisting (24 year mean) meandering of the current could be  
 242 observed, for instance, close to the Juan Fernández Ridge (located around 33.5°S and 600–800 km  
 243 off-shore) where, as model studies show, mesoscale eddies frequently interact with the ridge [42,43].  
 244 Another persistent mesoscale anti-cyclonic intrathermocline eddy offshore Punta Lavapié (37°S) [44]  
 245 was observed in the averaged altimetry data. The position of the jet within the main current was  
 246 between 76–79°W, very similar to the findings of [19], and likewise its bending was northwestward  
 247 north of 25°S. The lowest observed ADT stretched along the coast of Chile and was related to the  
 248 well-known upwelling of colder and denser seawater. According to altimetry assessment, the  
 249 strength of coastal upwelling was slightly more pronounced in the waters of central-south Chile,  
 250 although it is characterized only by a seasonal upwelling pattern compared to the mostly continuous  
 251 but localized upwelling pattern in northern Chile [31]. Cross-shore SST fronts were mirrored by  
 252 ADT fronts.



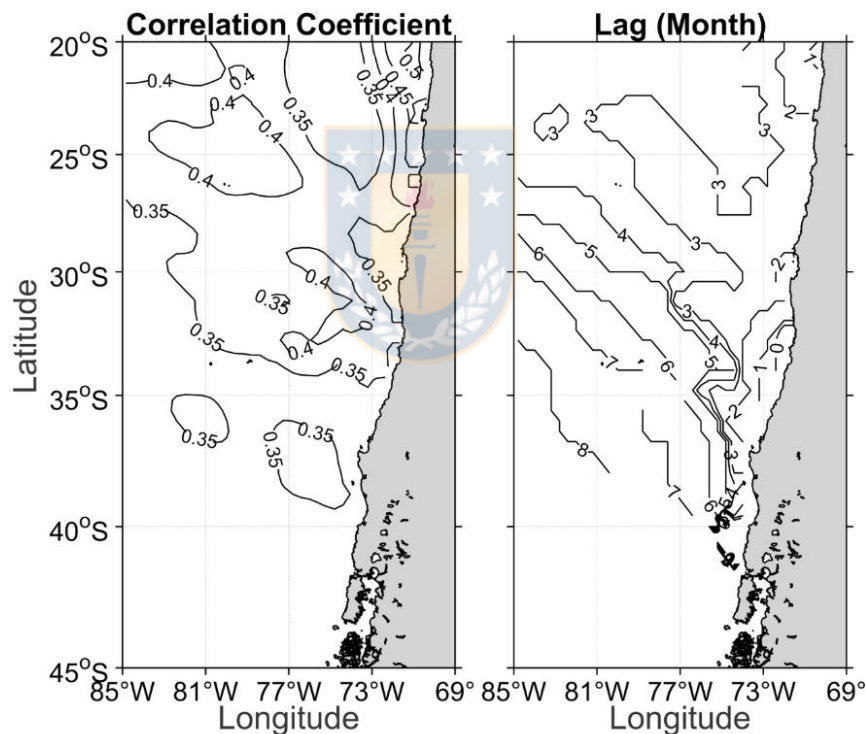
253

254 **Figure 3.** Left panel) Color contoured long-term mean absolute dynamic topography; Center panel)  
 255 Color contoured composite of ADT anomalies for El Niño scenarios and right panel) for La Niña  
 256 scenarios. The color bar on the right hand side of the figure applies to the center and right panels.

257 Composites of anomalies of ADT for El Niño and La Niña conditions, in general, followed SST  
 258 as expected. Due to thermal expansion, positive and negative ADT anomalies occurred during El  
 259 Niño and La Niña events, respectively (Figure 3, center and right). The positive anomalies during El  
 260 Niño episodes accounted for a 2–3 cm rise in sea level in the coastal transition zone off Chile but  
 261 waned towards the open ocean. Sea level rise was not homogenous, but displayed fronts, filaments,  
 262 bulges, and zonal bands. Among others, the anticyclonic mesoscale eddy off-shore Punta Lavapié  
 263 intensified, and quasi-zonal jets or striations could be identified, a common feature in altimetry  
 264 imagery off-shore Chile [45]. Positive anomalies changed to negative ones in La Niña episodes.  
 265 Cross-shore gradients were reduced (enhanced) in warmer (colder) ENSO periods.

266 During the 1997/98 El Niño event, the surface temperature of coastal waters of northern Chile  
 267 (23°S) was noticeably higher than during non-El Niño conditions [46], similar to the SST anomalies  
 268 for El Niño conditions (Figure 2, center panel). This warm anomaly was attributed to poleward  
 269 propagating, coastal trapped Kelvin waves along the west coast of the Americas, which  
 270 communicated the tropical Pacific El Niño signal to mid latitudes ([46–49]. The amplitudes of coastal  
 271 trapped waves decay exponentially toward the open ocean, limiting the wave's impact to the first

272 100 km offshore in subtropical latitudes. The coastal perturbations, and coastal pycnocline  
 273 anomalies, in turn, have the potential to trigger westward propagating Rossby waves across the  
 274 coastal transition zone well into the HCS and beyond [48,49] thereby disseminating warm (cold)  
 275 anomalies seaward as observed in Figure 2 (center and right panels). Deepening of the thermocline  
 276 in northern Chile, however, was already initiated in early 1997 [46], months ahead of the appearance  
 277 of positive SST anomalies in the central equatorial Pacific, which were registered to have started in  
 278 May 1997 (<https://origin.cpc.ncep.noaa.gov>). A cross correlation analysis between time series of SST  
 279 for the HCS and ONI revealed an overall weak, although statistically significant, correlation with  
 280 positive lags (Supplement 1), denoting that warm as well as cold SST anomalies occurred somewhat  
 281 before they appeared in the central equatorial Pacific. Maximum correlation coefficients ( $r = 0.5$ )  
 282 were observed in the northeastern corner of the HCS close to the coast but decreased in the  
 283 southwest direction ( $r < 0.3$ ). The associated time lags increased following the same track from 1  
 284 month to more than 8 months with the exception of the coastal zone (lag = 0 – 2 months), which was  
 285 dominated by coastal upwelling. SST analysis for the second half of last century exposed a  
 286 well-defined dipole whereby warm (cold) conditions along the equator corresponded to cold  
 287 (warm) conditions in a band near 30°S in the central south Pacific [47], a remnant of which was  
 288 obvious in our analysis of the last 24 years (Figure 2, center and right) and coincided with larger time  
 289 lags in the cross correlation analysis between SST and ONI. Coastal trapped waves along the coast of  
 290 Chile, related to ENSO events, appeared to compete with the imprint of coastal upwelling.



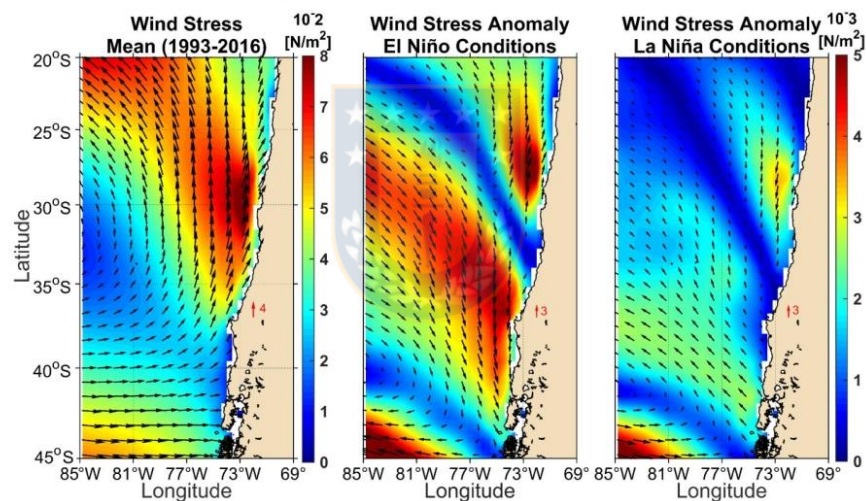
291

292 **Supplement 1.** Left panel) Cross correlation coefficient SST versus ONI and right panel) the  
 293 corresponding lag (in months). Correlation coefficients less than 0.3 were suppressed together with  
 294 the corresponding lags.

295

296 The fields of mean near-surface **wind** and mean **wind stress** over the HCS were controlled by  
 297 the South Pacific High, the permanent anticyclonic subtropical high atmospheric pressure system,  
 298 which is centered in the eastern South Pacific (Figure 4, left panel [50]). Westerly winds/wind stress  
 299 dominated the region poleward of 40°S, but otherwise the wind blew equatorward (favorable of  
 300 coastal upwelling), displaying highest magnitudes offshore central Chile. Our fields of mean wind  
 301 and mean wind stress were consistent with those of Rahn and Garreaud [50] who employed CFSR  
 302 (Climate Forecast System Reanalysis, 1979–2010) and QuickScat (1999–2009) winds, both products  
 303 having a slightly better horizontal resolution than the ERA Interim products used here. Wind stress  
 304 is mainly responsible for setting up currents and generating eddies and filaments in the coastal  
 305 ocean of Chile [20]. Wind stress over the Humboldt Current was weaker (stronger) during El Niño  
 306 (La Niña) scenarios (Figure 4, center and right) in agreement with a less (more) intense SPH and  
 307 associated alongshore pressure gradient [50]. In this region, and in the coastal upwelling zone of  
 308 central-south Chile, wind stress during the cold events surpassed the warm conditions, on average,  
 309 by about 0.006 N/m<sup>2</sup> or by 10%, which resulted in more favorable conditions for upwelling during La  
 310 Niña than El Niño events. This was reflected in colder SST and lower sea level in the former events.  
 311 Likewise winds were stronger in La Niña scenarios in the band predominated by the westerlies  
 312 south of 40°S. Nevertheless, the situation was reversed in the coastal transition zone north of 30°S  
 313 being more favorable for coastal upwelling during El Niño events. The weaker winds over the  
 314 Humboldt Current were separated by a northwest elongated band (dark blue colors in Figure 4,  
 315 center and right) from the stronger ones in northern Chile.

316



317

318

319

320

**Figure 4.** Left panel) Mean wind stress (black arrows) and color contoured long-term mean wind stress magnitude; Center panel) Anomalous wind stress (black arrows) and color contoured wind stress magnitude for El Niño conditions, and right panel) similar to the center but for La Niña conditions. The color bar on the right hand side of the figure applies to the center and right panels.

321

322

323

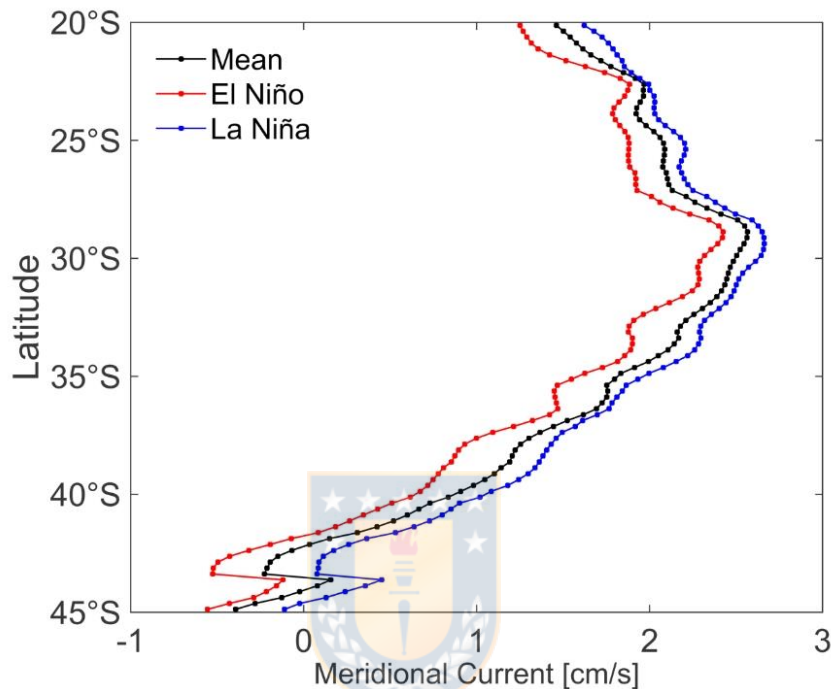
324

325

326

All sub-tropical gyres, similar to the South Pacific, are wind-driven [51] and changes in their intensity are related to changes in the forcing wind fields. The HC is much weaker than for instance the Kuroshio Current in the North Pacific. For the HCS as a whole (or the far eastern boundary of the sub-tropical gyre), the mean **meridional geostrophic velocity** was only in the order of 2 cm s<sup>-1</sup> (Figure 5, black dots), as calculated from the CMEMS geostrophic velocity product, but it corresponded to a meridional volume transport of about 2.5 Sv. Meridional transport increased from

327 40°S, where the HC initiated, and reached its maximum transport offshore central Chile around the  
 328 30<sup>th</sup> parallel in agreement with the occurrence of the strongest wind stress curl. The equatorward  
 329 volume transport was significantly larger during La Niña conditions than during El Niño ones, an  
 330 artifact of the intensified winds during the former episodes. The volume transport during the cold  
 331 ENSO phases surpassed the warmer phases by more than 10%, and the average speed of the HC  
 332 followed suit.

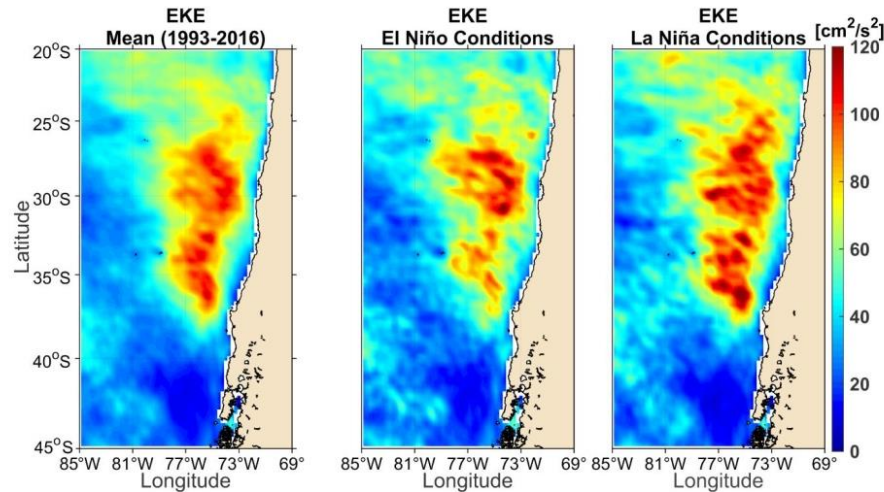


333

334 **Figure 5.** Zonal means of meridional velocity components within the HCS. Black) the 1993–2016  
 335 mean; Red) the mean for El Niño events that occurred during 1993–2016; Blue) the mean for La Niña  
 336 events that occurred during 1993–2016.

337 The distribution of EKE within the HCS was strongly related to the position and intensity of the  
 338 HC, especially with the jet therein (Figure 6, left panel [19]). Long term mean values of EKE  
 339 exceeded  $100 \text{ cm}^2 \text{ s}^{-2}$  and were observed around 200–400 km offshore between 37–25°S the region,  
 340 which also was occupied by the core of the HC. The range of EKE was consistent with that published  
 341 by Hormazabal [41]. However, the pattern differed perhaps owing to the employment of a much  
 342 shorter time scale of (1992–2001) sea level anomaly data set and the differing formulation of the  
 343 reference mean velocity components in the calculation of EKE. In their study, maximum mean  
 344 values of EKE were only obtained south of 30°S with a zonal extension similar to our estimation,  
 345 leaving a less energetic northern HCS. The CMEMS data set, on the other hand, disclosed a much  
 346 more energetic HC for La Niña events than for El Niño events north of 37°S and up to 23°S with  
 347 maximum values for EKE clearly exceeding  $100 \text{ cm}^2 \text{ s}^{-2}$  (Figure 6, center and right panel). For El Niño  
 348 periods, in contrast, the intensity declined in the southern part of the HC (south of 32°S), similar to  
 349 that equatorward of 26°S. Stronger currents and winds both appear to be responsible for the elevated  
 350 EKE during La Niña phases. Eddy kinetic energy related to the HC, however, was much less than

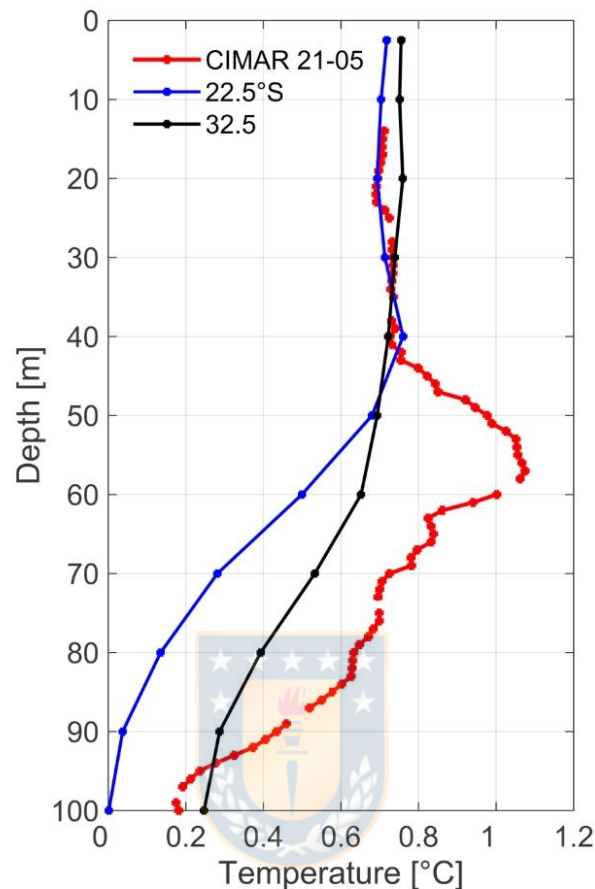
351 that reported on maximum values for the Gulf Stream system, which exceeded  $5000 \text{ cm}^2 \text{ s}^{-2}$  in some  
 352 places, thus highlighting the dynamical difference between the eastern (HCS) and western (Gulf  
 353 Stream system) boundaries of the sub-tropical gyres [52].



354

355 **Figure 6.** Eddy Kinetic energy. Left) 1993–2016 mean eddy kinetic energy; Center) mean eddy  
 356 kinetic energy for El Niño events that occurred during 1993–2016; Right) mean eddy kinetic energy  
 357 for La Niña events that occurred during 1993–2016.

358 Composites of relevant variables for characterizing El Niño and La Niña conditions were  
 359 restricted to surface or near-surface environments. We analyzed the mechanism of changes in the  
 360 **temperature of the upper water column** (100 m) across 3 different latitudes of the HCS  
 361 (approximately 1500 km wide) during selected warm and cold phases of ENSO. The differences of  
 362 weighted (horizontal and vertical) zonal means of the upper 100 m temperature between El Niño  
 363 and La Niña events along  $22.5^\circ\text{S}$ ,  $27^\circ\text{S}$ , and  $32.5^\circ\text{S}$  are presented in Figure 7. The data along  $27^\circ\text{S}$  are  
 364 based on two Chilean research cruises, namely CIMAR 5, October 1999, and CIMAR 21, October  
 365 2015. CIMAR 5 was conducted in the middle of the long La Niña event from July 1998 to February  
 366 2001 and CIMAR 21 was carried out in the middle of the strong El Niño event from November 2014  
 367 to March 2016. For the latitudinal sections along  $22.5^\circ\text{S}$  and  $32.5^\circ\text{S}$ , data from the Roemmich-Gilson  
 368 Argo monthly database were employed. From the 13-year long record, we computed a monthly  
 369 climatology, which then was subtracted from the actual temperature data to generate a new dataset  
 370 consisting of temperature anomalies. These anomalies were averaged over the El Niño period  
 371 November 2014 to March 2016 and the La Niña period from June 2010 to March 2012, respectively.  
 372 The El Niño minus La Niña differences for all three computations yielded a  $0.7^\circ \text{C}$  surplus in the  
 373 upper 40 m of the water column in favor of El Niño.



374

375 **Figure 7.** Upper water column (100 m) temperature differences between El Niño and La Niña events.  
 376 The red vertical profile stands for the overall temperature difference between the CIMAR-21 and  
 377 CIMAR-5 cruises along 27° S from the coast of Chile to 86.55° W (about 1500 km), obtained during  
 378 Oct 2015 and Oct 1999, respectively. The blue (along 22.5° S) and black (along 32.5° S) profiles were  
 379 computed employing the Roemmich-Gilson Argo monthly Climatology. The difference in  
 380 temperature is for the area from the coast of Chile to 85° W averaged for the El Niño period Nov/2014  
 381 to Mar/2016 versus the La Niña period Jun/2010 to Mar/2012.

382 In terms of statistical difference during El Niño and La Niña episodes, all hydrographic and  
 383 meteorological variables analyzed, SST, ADT, wind stress, geostrophic velocity, EKE, and upper  
 384 surface ocean temperature passed the Z-test based at the 99% significance level or alpha equal to  
 385 0.01. These El Niño and La Niña composites represent mean conditions of the respective scenarios  
 386 independent of strength and duration, although stronger and longer lasting events contributed  
 387 more. The total length of El Niño periods from 1993 to 2016 was 70 months with 7 events and is  
 388 comparable to the total length of La Niña periods, which was 83 months also comprising 7 events.  
 389 Global SST rose by about 0.4°C during the time span considered in this study (NOAA 2019), which



390 does not affect our results since SST anomalies were studied and warm and cold events were  
391 distributed almost equally through time; this is also applicable to ADT and the other variables.

392 Differences in SST between mean El Niño and La Niña conditions were more than 0.6°C in  
393 some areas, especially close to the coast. Mean upper ocean temperature differences were in the  
394 same order in the entire northern portion of the HCS when comparing October 2015 El Niño data  
395 with the La Niña ones from October 1999 (Figure 7). However, temperature differences were also  
396 larger closer to the coast; here a very strong El Niño month was compared to a moderate La Niña  
397 month. The duration of ENSO events is also of importance: upper ocean temperature in the HCS was  
398 significantly warmer in the very same order (>0.6°C) during the 2015/16 El Niño event that lasted for  
399 more than a year and the equally long 2010/11 La Niña event (Figure 7). Warming of the oceanic  
400 environment has been shown to decrease the biomass of microzooplankton. From the 1950s to the  
401 beginning of the 1990s, oceanic warming on the order of 1.0°C was found to decrease  
402 microzooplankton biomass by 80% in the coastal upwelling zone off southern California [53].  
403 Temperature fluctuations may also modify the dominant species of fish encountered. “Phases with  
404 mainly negative temperature anomalies paralleled anchovy regimes (1950–1970; 1985–2000) and the  
405 rather warm period from 1970 to 1985 was characterized by sardine dominance” offshore Peru and  
406 Chile [54]. Further, Oey *et al.* [55] showed that fish catch was related to transport fluctuations of the  
407 Kuroshio Current, and Contreras-Catala *et al.* [56] suggested correlations between geostrophic  
408 kinetic energy and the abundance of mesopelagic fish larvae, suggesting that areas with low kinetic  
409 energy are more favorable for feeding and development.

410 Hence, the observed different mean conditions for El Niño compared to La Niña scenarios,  
411 namely, warmer SST, higher sea level, weaker winds, a weaker HC, and a less turbulent  
412 environment (EKE) potentially impact on the marine ecosystems of the Chilean portion of the  
413 Humboldt current System. affect

#### 414 4. Conclusions

415 Physical conditions in the Chilean portion of the HCS were significantly different during El  
416 Niño and La Niña episodes when taking the full evolution of the ENSO events into account, i.e. once  
417 the +/- 0.5°C threshold applied.

418 Wind stress increased by about 10% during La Niña conditions compared to El Niño.

419 The upper water column was warmer by approximately 0.5°C during el Niño than during La  
420 Niña events.

421 ADT increased by 2-3 cm from La Niña to El Niño scenarios.

422 The Humboldt Current was stronger during La Niña than El Niño.

423 Consequently, EKE also was more intense during La Niña episodes than during El Niño  
424 episodes.

425

#### 426 5. Patents

427 This section is not mandatory, but may be added if there are patents resulting from the work  
428 reported in this manuscript.

429 **Supplementary Materials:** The following are available online at [www.mdpi.com/xxx/s1](http://www.mdpi.com/xxx/s1), Figure S1: title, Table  
430 S1: title, Video S1: title.

431 **Author Contributions:** Conceptualization, FHV and WS; methodology, FHV and WS; investigation, FHV;  
432 writing—original draft preparation, WS; visualization, FHV.; supervision, WS; funding acquisition CIMAR  
433 21, WS. All authors have read and agreed to the published version of the manuscript.”

434 **Funding:** This research was partly funded by CONA (Comité Oceanográfico Nacional de Chile)  
435 through the CIMAR 21 Islas expedition, 2015.

436 Freddy Hernández-Vaca thanks the sponsorship of the scholarship contract No 20090315 between  
 437 Secretaría de Educación Superior, Ciencia, Tecnología e Innovación (SENESCYT), Instituto  
 438 Oceanográfico de la Armada (INOCAR); as well as the resolution INOCAR-RHU-2016-040-O.

439

440 **Acknowledgments:** The Oceanic Niño Index was obtained from NOAA Climate Prediction Center  
 441 ([http://www.cpc.ncep.noaa.gov/products/analysis\\_monitoring/ensostuff/ensoyears.shtml](http://www.cpc.ncep.noaa.gov/products/analysis_monitoring/ensostuff/ensoyears.shtml)).  
 442 ERA- Interim data used in this manuscript (SST and wind products) have been provided by ECMWF  
 443 (European Center for Medium Weather Forecast data server  
 444 <http://apps.ecmwf.int/datasets/data/interim-full-moda/>). ADT and geostrophic velocity data were  
 445 downloaded from the E.U. Copernicus Marine Service Information ([www.marine.copernicus.eu](http://www.marine.copernicus.eu)).  
 446 Hydrographic profiles measured during the CIMAR 5 and 21 (Cruceros de Investigación Marina)  
 447 expeditions conducted by CONA (Comité Oceanográfico Nacional de Chile) were employed in this  
 448 study. Ocean temperature and salinity of the upper 2000 m of the water column stem from the  
 449 international Argo program and were compiled to a monthly mean  $1^\circ \times 1^\circ$  gridded global data set,  
 450 the Roemmich-Gilson Argo Climatology, which was used in this study.

451

452 **Conflicts of Interest:** The authors declare no conflict of interest.

#### 453 References

- 454 1. Collins, M.; An, S.; Cai, W.; Ganachaud, A.; Guilyardi, E.; Jin, F.; Jochum, M.; Lengaigne, M.; Power, S.,  
 455 Timmermann, A.; Vecchi, G.; Wittenberg, A. The impact of global warming on the tropical Pacific Ocean  
 456 and El Niño. *Nat. Geosci.* **2010**, *3*, 391–397.
- 457 2. Tomczak, M.; Godfrey, J.S. Regional oceanography: An introduction. Pergamon Press, Oxford, England.
- 458 3. Trenberth KE, (2001), Climate: El Niño-Southern Oscillation (ENSO). In: Steele J, Thorpe S, Turekian K  
 459 (eds.). Encyclopedia of Ocean Sciences. Academic Press. 815-827.
- 460 4. Folland, C.K.; Renwick, J.A.; Salinger, M.J.; Mullan, A.B. Relative influences of the Interdecadal Pacific  
 461 Oscillation and ENSO on the South Pacific Convergence Zone. *Geophys. Res. Lett.* **2002**, *29*, 1643.  
 462 DOI:10.1029/2001GL014201.
- 463 5. McPhaden, M.; Zebiak, S.; Glantz, M. ENSO as an integrating concept in earth science. *Science* **2006**,  
 464 *314*(5806), 1740–1745. DOI:10.1126/science.1132588.
- 465 6. Hoerling, M.P.; Kumar, A.; Xu, T. Robustness of the nonlinear climate response to ENSO's extreme phases.  
 466 *J. Clim.* **2001**, *14*(6), 1277–1293.
- 467 7. Harrison, D.; Larkin, N. El Niño-Southern Oscillation sea surface temperature and wind anomalies,  
 468 1946–1993. *Rev. Geophys.* **1998**, *36*(3), 353–399.
- 469 8. Klein, S.; Soden, B.; Lau, N.; Remote sea surface temperature variations during ENSO: evidence for a  
 470 tropical atmospheric bridge. *J. Clim.* **1999**, *12*, 917–931.
- 471 9. Lilly, L.; Ohman, M. El Niño-related zooplankton variability in the southern California Current System.  
 472 *Deep Sea Res. I* **2018**, *140*, 36–51. DOI:10.1016/j.dsr.2018.07.015.
- 473 10. Marinovic, B.; Croll, D.; Gong, N.; Benson, S.; Chavez, F. Effects of the 1997–1999 El Niño and La Niña  
 474 events on zooplankton abundance and euphausiid community composition within the Monterey Bay  
 475 coastal upwelling system. *Prog. Oceanogr.* **2002**, *54*, 265–277. DOI:10.1016/S0079-6611(02)00053-8.
- 476 11. Niquen, M.; Bouchon, M. Impact of El Niño events on pelagic fisheries in Peruvian waters. *Deep Sea Res. II*  
 477 **2004**, *51*, 563–574. DOI:10.1016/j.dsr2.2004.03.001
- 478 12. Fiedler, P.; Methot, R.; Hewitt, R. Effects of California El Niño 1982–1984 on the northern anchovy. *J. Mar.*  
 479 *Res.* **1986**, *44*, 317–338.
- 480 13. Levitus, S. Climatological atlas of the world ocean. *NOAA Profess. Pap.* **1982**, *13*, 1–173.
- 481 14. Reid, J.L. On the total geostrophic of the South Pacific Ocean: Flow patterns, tracers and transports. *Prog.*  
 482 *Oceanogr.* **1986**, *16*, 1–61. DOI:10.1016/0079-6611(86)90036-4.
- 483 15. Strub, T.; Mesias, J.; Montecino, V.; Rutllant, J.; Salinas, S. Coastal ocean circulation off western South  
 484 America. In: Robinson AR, Brink KH (ed) The Sea, vol. 11, pp. 273–313, John Wiley, Hoboken, NJ.

- 485 16. Chaigneau, A.; Pizarro, O. Mean surface circulation and mesoscale turbulent flow characteristics in the  
486 eastern South Pacific from satellite tracked drifters. *J. Geophys. Res. Oceans* **2005a**, *110*(C5). DOI:10.1029/  
487 2004JC002628.
- 488 17. Wooster, W.; Reid, J. Eastern boundary currents. In: Hill M.N. (ed.) *The Sea*, vol. 2. Wiley-Interscience,  
489 Hoboken. 253–280.
- 490 18. Strub, P.T.; James, C.; Montecino, V.; Rutllant, J.A.; Blanco, J.L. Ocean circulation along the southern Chile  
491 transition region (38°–46° S): Mean, seasonal and interannual variability, with a focus on 2014–2016. *Prog.*  
492 *Oceanogr.* **2019**, *172*, 159–198. DOI:10.1016/j.pocean.2019.01.004.
- 493 19. Fuenzalida, R.; Schneider, W.; Garcés-Vargas, J.; Bravo L. Satellite altimetry data reveal jet-like dynamics  
494 of the Humboldt Current. *J. Geophys. Res.* **2008**, *113*(C7). DOI:10.1029/2007JC004684.
- 495 20. Leth, O.; Shaffer G. A numerical study of seasonal variability in the circulation off central Chile. *J. Geophys.*  
496 *Res.* **2001**, *106*(C10), 22229–22248. doi:10.1029/2000JC000627.
- 497 21. Sobarzo, M.; Bravo, L.; Donoso, D.; Garcés-Vargas, J.; Schneider, W. Coastal upwelling and seasonal cycles  
498 that influence the water column over the continental shelf off central Chile. *Prog. Oceanogr.* **2007**, *75*(3),  
499 363–382.
- 500 22. Ancapichún, S.; Garcés-Vargas, J. Variability of the Southeast Pacific Subtropical Anticyclone and its  
501 impact on sea surface temperature off north-central Chile. *Cien. Mar.* **2015**, *41*(1), 1–20.
- 502 23. Shaffer, G.; Hormazabal, S.; Pizarro, O.; Salinas, S. Seasonal and interannual variability of currents and  
503 temperature off central Chile. *J. Geophys. Res.* **1999**, *104*(C12), 29951–29961. DOI:10.1029/1999JC900253.
- 504 24. Sydeman, W.; García-Reyes, M.; Schoeman, D.; Rykaczewski, R.; Thompson, S.; Black, B.; Bograd, S.  
505 Climate change and wind intensification in coastal upwelling ecosystems. *Science* **2014**, *345*(6192), 77–80.
- 506 25. Chavez, F.P.; Messié, M. A comparison of eastern boundary upwelling ecosystems. *Prog. Oceanogr.* **2009**,  
507 *83*(1–4), 80–96.
- 508 26. Jacob, B.; Tapia, F.; Quiñones, R.; Montes, R.; Sobarzo, M.; Schneider, W.; Daneri, D.; Morales, C.; Montero,  
509 P.; González H. Major changes in diatom abundance, productivity, and net community metabolism in a  
510 windier and dryer coastal climate in the southern Humboldt Current. *Prog. Oceanogr.* **2018**, *168*, 196–209.
- 511 27. Freon, P.; Barange, M.; Aristegui, J. Eastern boundary upwelling ecosystems: integrative and comparative  
512 approaches. *Prog. Oceanogr.* **2009**, *83*, 1–14. DOI:10.1016/j.pocean.2009.08.001.
- 513 28. Chaigneau, A.; Pizarro, O. Eddy characteristics in the eastern South Pacific. *J Geophys Res. Oceans* **2005b**,  
514 *110*(C6).
- 515 29. Correa-Ramirez, M.; Hormazabal, S.; Yuras, G. Mesoscale eddies and high chlorophyll concentrations off  
516 central Chile (29°–39°S). *Geophys. Res. Lett.* **2007**, *34*(12).
- 517 30. Escribano, R.; Morales, M. Spatial and temporal scales of variability in the coastal upwelling and coastal  
518 transition zones off central-southern Chile (35–40°S). *Prog. Oceanogr.* **2012**, *92–95*, 1–7.  
519 DOI:10.1016/j.pocean.2011.07.019.
- 520 31. Thiel, M.; Macaya, E.C.; Acuna, E; et al. The Humboldt Current System of northern and central Chile:  
521 oceanographic processes, ecological interactions and socioeconomic feedback. *Oceanogr. Mar. Biol. Ann.*  
522 *Rev.* **2007**, *45*, 195–344.
- 523 32. Montecino, V.; Lange C.B. The Humboldt Current System: Ecosystem components and processes,  
524 fisheries, and sediment studies. *Prog. Oceanogr.* **2009**, *83*(1–4), 65–79.
- 525 33. Larkin, N.; Harrison, D. ENSO warm (El Niño) and cold (La Niña) event life cycles: Ocean surface  
526 anomaly patterns, their symmetries, asymmetries, and implications. *J. Clim.* **2002**, *15*(10), 1118–1140.  
527 DOI:10.1175/1520-0442(2002)015<1118:EWENO>2.0.CO;2
- 528 34. Dee, D.P.; Uppala, S.M.; Simmons, A.J.; Berrisford, P.; Poli, P.; Kobayashi, S.; Andrae, U.; Balmaseda, M.A.;  
529 Balsamo, G.; Bauer, P.; et al. The ERA-Interim reanalysis: Configuration and performance of the data  
530 assimilation system. *Quart. J. Roy. Meteor. Soc.* **2011**, *137*, 553–597.
- 531 35. Trenberth, K.; Large, W.; Olson, J. The mean annual cycle in global ocean wind stress. *J. Phys. Oceanogr.*  
532 **1990**, *20*(11), 1742–1760.
- 533 36. Pujol, M.I.; Faugère, Y.; Taburet, G.; Dupuy, S.; Pelloquin, C.; Ablain, M.; Picot, N. DUACS DT2014: the  
534 new multi-mission altimeter data set reprocessed over 20 years. *Ocean Sci.* **2016**, *12*(5).
- 535 37. Roemmich, D.; Gilson, J. The 2004–2008 mean and annual cycle of temperature, salinity, and steric height  
536 in the global ocean from the Argo Program. *Prog. Oceanogr.* **2009**, *82*(2), 81–100.  
537 DOI:10.1016/j.pocean.2009.03.004.
- 538 38. Emery, W.; Meincke, J. Global water masses: summary and review. *Oceanologica Acta* **1986**, *9*(4), 383–391.

- 539 39. Silva, N.; Rojas, N.; Fedele, A. Water masses in the Humboldt Current System: Properties, distribution,  
540 and the nitrate deficit as a chemical water mass tracer for Equatorial Subsurface Water off Chile. *Deep Sea*  
541 *Res. II* **2009**, *56*(16), 1004–1020.
- 542 40. Oerder, V.; Bento, J.; Morales, C.; Hormazabal, S.; Pizarro, O. Coastal upwelling front detection off central  
543 Chile (36.5–37° S) and spatio-temporal variability of frontal characteristics. *Remote Sens.* **2018**, *10*(5), 690.
- 544 41. Hormazabal, S.; Núñez, S.; Arcos, D.; Espindola, F.; Yuras, G. Mesoscale eddies and pelagic fishery off  
545 Central Chile (33–40 S). *Gayana (Concepción)* **2004**, *68*(2), 291–296.
- 546 42. Hormazabal, S.; Combes, V.; Morales, C.; Correa-Ramirez, M.; Di Lorenzo, E.; Nuñez, S. Intrathermocline  
547 eddies in the coastal transition zone off central Chile (31–41 S). *J. Geophys. Res. Oceans* **2013**, *118*(10),  
548 4811–4821.
- 549 43. Medel, C.; Parada, C.; Morales, C.; Pizarro, O.; Ernst, B.; Conejero, C. How biophysical interactions  
550 associated with sub-and mesoscale structures and migration behavior affect planktonic larvae of the spiny  
551 lobster in the Juan Fernández Ridge: A modeling approach. *Prog. Oceanogr.* **2018**, *162*, 98–119.
- 552 44. Morales, C.; Anabalón, V.; Bento, J.P.; Hormazabal, S.; Cornejo, M.; Correa-Ramírez, M.; Silva, N.  
553 Front-Eddy influence on water column properties, phytoplankton community structure, and cross-shelf  
554 exchange of diatom taxa in the shelf-slope area off concepción (~36–37° S). *J. Geophys. Res. Oceans* **2017**,  
555 *122*(11), 8944–8965.
- 556 45. Belmadani, A.; Concha, E.; Donoso, D.; Chaigneau, A.; Colas, F.; Maximenko, N.; Di Lorenzo, E. Striations  
557 and preferred eddy tracks triggered by topographic steering of the background flow in the eastern South  
558 Pacific. *J. Geophys. Res. Oceans* **2017**, *122*(4), 2847–2870.
- 559 46. Ulloa, O.; Escibano, N.; Hormazabal, S.; Quiñones, R.; Gonzalez, R.; Ramos, M. Evolution and biological  
560 effects of the 1997–98 El Niño in the upwelling ecosystem off northern Chile. *Geophys. Res. Lett.* **2001**, *28*(8),  
561 1591–1594.
- 562 47. Shaffer, G.; Pizarro, O.; Hormazabal, S.; Venegas, S. Imprint of El Niño/La Niña cycles on the Humboldt  
563 Current system. *Invest. Mar.* **2002**, *30*(1), 91–92.
- 564 48. Hormazabal, S.; Shaffer, G.; Pizarro, O. Tropical Pacific control of intraseasonal oscillations off Chile by  
565 way of oceanic and atmospheric pathways. *Geophys. Res. Lett.* **2002**, *29*(6), 5–1–5–4.
- 566 49. Vega, A.; du-Penhoat, Y.; Dewitte, B.; Pizarro, O. Equatorial forcing of interannual Rossby waves in the  
567 eastern South Pacific. *Geophys. Res. Lett.* **2003**, *30*(5), 1197. DOI:10.1029/2002GL015886.
- 568 50. Rahn, D.; Garreaud, R. A synoptic climatology of the near-surface wind along the west coast of South  
569 America. *Int. J. Climatol.* **2013**, *34*(3), 780–792.
- 570 51. Munk, W.H. On the wind-driven ocean circulation. *J. Meteorol.* **1950**, *7*(2), 80–93.
- 571 52. Zhai, X.; Greatbatch, R.; Kohlmann, J.-D. On the seasonal variability of eddy kinetic energy in the Gulf  
572 Stream region. *Geophys. Res. Lett.* **2008**, *35*, L24609, DOI:10.1029/2008GL036412.
- 573 53. Roemmich, D.; McGowan, J. Climatic warming and the decline of zooplankton in the California Current.  
574 *Sci. New Series* **1995**, *267*(5202), 1324–1326.
- 575 54. Alheit, J.; Niquen, M. Regime shifts in the Humboldt Current ecosystem. *Prog. Oceanogr.* **2004**, *60*, 201–222.  
576 DOI:10.1016/j.pocean.2004.02.006
- 577 55. Oey, L.; Wang, J.; Lee, M.-A. Fish catch is related to the fluctuations of a Western Boundary Current. *J.*  
578 *Phys. Oceanogr.* **2018**. doi:10.1175/JPO-D-17-0041.1
- 579 56. Contreras-Catala, F.; Sánchez-Velasco, L.; Beier, E.; Godínez, V.M.; Barton, E.D.; Santamaría-del-Angel, E.  
580 Effects of geostrophic kinetic energy on the distribution of mesopelagic fish larvae in the Southern Gulf of  
581 California in summer/fall stratified seasons. *PLoS ONE* **2016**, *11*(10), e0164900.  
582 DOI:10.1371/journal.pone.0164900.
- 583 57. NOAA. Climate at a Glance. 2019, Available in  
584 <http://www.ncdc.noaa.gov/cag/global/timeseries/globe/ocean/ytd/12/1880-2016>.
- 585



© 2020 by the authors. Submitted for possible open access publication under the terms and conditions of the Creative Commons Attribution (CC BY) license (<http://creativecommons.org/licenses/by/4.0/>).

586

4.3 Capítulo 3: Fortalecimiento de los Giros Subtropicales: Variabilidad y Tendencias (1993-2018) (Manuscrito en Preparación)

The Strength of the Pacific Subtropical Gyres: Variability and Trends  
(1993-2018)

Freddy Hernández-Vaca<sup>a, b, c</sup> and Wolfgang Schneider<sup>\* b, d</sup>

<sup>a</sup> Programa de Postgrados en Oceanografía, Departamento de Oceanografía, Universidad de Concepción, Chile

<sup>b</sup> Instituto Milenio de Oceanografía (IMO), Universidad de Concepción. Proyecto IC 120019.

<sup>c</sup> Dirección Oceanografía Naval, Instituto Oceanográfico de la Armada, Apartado postal: 5940 Guayaquil-Ecuador. Email: freddy.hernandez@inocar.mil.ec

<sup>d</sup> Departamento de Oceanografía, Universidad de Concepción, Campus Concepción, Víctor Lamas 1290, Casilla 160-C, código postal: 4070043 Concepción, Chile

---

\* Corresponding author at: Departamento de Oceanografía, Universidad de Concepción, Campus Concepción, Víctor Lamas 1290, Casilla 160-C, código postal: 4070043 Concepción, Chile. E-mail addresses: wschneid@udec.cl (W. Schneider)

To be submitted to Journal of Geophysical Research Oceans

**Abstract**

Satellite-born altimetry estimates of absolute dynamic topography from 1993 to 2018 were employed to shed light on fluctuations and trends of the strength of the circulation of the subtropical gyres. Sea level dropped in the centers/cores of both subtropical gyres but amplified in the boundary systems of the California and the Humboldt currents, related to strong and moderate El Niño events. The opposite occurred during La Niña events. The Strength of the Subtropical Gyres was estimated as the difference in sea level between the centers of the Gyres and its respective eastern boundaries, divided by the distance between these two locations. As a consequence of this anti-cyclical behavior the Strength of the

Subtropical Gyres in both gyres weakened sharply (moderately), up to 25% during strong (moderate) El Niño events and increased in La Niña episodes. The circulation in the North Pacific responded to El Niño within one to two months of its occurrence, while in the South Pacific it did so after five to six months. Further, an inter-decadal mode was detected in the Strength of the Subtropical Gyres, which enhanced (weakened) their circulation during the first (second) half of the observational period. Sea level rise, during the satellite altimetry period, 1993 to 2018, exceeded the basin's mean in the centers/cores of the gyres but was below these means in its eastern boundaries, especially in the South Pacific. This yielded in an acceleration of the circulation of both gyres during this 26-year period.

### **Key Points**

- A new measure for the strength of the Pacific subtropical gyre circulations was introduced
- ENSO was the main cause of variability induced on the Strength of the subtropical gyres, with amplitudes exceeding the trend
- The circulation in the North Pacific responded to El Niño within one to two months of its occurrence, while in the South Pacific it did so after five to six months
- Sea level rise in the centers/cores of the subtropical gyres by far exceeded the gain in its eastern boundaries - - > Trend of Strength of the subtropical gyres
- Ongoing sea level rise contributes to the intensification of the subtropical gyres of the Pacific

### **Introduction**

Subtropical anti-cyclonic high atmospheric pressure systems that sit above the large-scale ocean basins of the Atlantic, Pacific and Indian Oceans in both hemispheres control the near ocean surface wind fields therein. Easterly and North- and South-Easterly trade winds dominate the tropical regions on both sides of the Equator, whereas westerly winds govern the subpolar zones; wind direction follows the continental coastlines at the eastern and western borders of the basins. Surface currents are induced by wind stress but are deflected by about 45° to the direction of the wind due to Earth rotation, to the right (left) in the northern (southern) hemisphere. Ekman transports within the Ekman layer of the upper ocean, in each of these ocean basins, give rise to the establishment of subtropical convergence zones between both zonal wind systems around latitudes between 20-30° N/S.

At these convergence zones sea surface height rises, water sinks, and the thermocline deepens significantly. Thus, horizontal pressure gradients are created which institutes geostrophic motion in the interior of the ocean perpendicular to the gradients, and Coriolis force combined with continental barriers induce an anti-cyclonic basin-wide circulation, the subtropical gyres. The centers of these gyres are shifted far to the west of the ocean basins, known as westward intensification, owing to an increase of the Coriolis force with latitude and the conservation of potential vorticity. Although the circulation of the subtropical gyres is controlled by geostrophy, the gyres are predominantly wind-driven since the horizontal pressure gradients would not exist without the winds.

Sea surface height in the centers of the gyres, located in the extreme western part of the ocean basins, exceeds sea surface height at its eastern and western limits by up to 1 m, this way forming distinct western and eastern boundary conditions. Sverdrup theory, in which the equatorward transport is induced by the curl of the wind stress at sea surface, holds in the interior of the ocean, east of the gyres' center, whereas strong and narrow poleward currents compensate this transport west of the centers. The western boundary currents are very intense and can surpass velocities of  $1 \text{ ms}^{-1}$ ; east of the centers of the gyres velocities are weaker, by one order of magnitude or less. The western boundary current of the North Pacific subtropical gyre is the Kuroshio Current; in the south Pacific it is the East Australian Current. The California Current system and the Humboldt Current system constitute the eastern boundary flows of the North and south Pacific subtropical gyres, respectively. The eastern and western boundary currents of both gyres are connected equatorward by the North and South Equatorial Currents, and poleward by the North and South Pacific Currents.

Here we introduce a robust and easy to compute measure for the estimation of the strength of the Pacific sub-polar gyres during times of accelerated sea level rise: 1993-2018, based on satellite altimetry only. This measure is based on the difference in Absolute Dynamic Topography between the centers/cores and the eastern boundaries of the gyres. Therefore, first, mean global and mean North and South Pacific sea level rise is addressed. Secondly, the evolution of sea surface height of the centers/cores of both subtropical gyres and their eastern boundaries is examined. Thirdly, the new measure for the strength of the gyres' circulation is applied and studied. Then these measures are decomposed by means of an Empirical Mode Decomposition (EMD), which allows separating the trend within the observational period, a

decadal mode and ENSO contributions. Finally, a mechanism for the growth of the South Pacific Subtropical Gyre is presented.

## **Data and Methods**

### Data: Absolute Dynamic Topography

Fields of Absolute Dynamic Topography (ADT) of the sea surface derived from satellite altimetry were extracted from the satellite multi-mission product of the Copernicus Marine Environment Monitoring Service (CMEMS) server “ftp://my.cmems-de.eu/Core/SEALEVEL\_GLO\_PHY\_L4\_REP\_OBSERVATIONS\_008\_047/dataset-duacs-rep-global-merged-allsat-phy-I4”, and employed in this study. The original measurements leading to fields of ADT were centered on radar pulses, which were emitted from the satellite antennas. The time taken by the radar pulses to travel from the satellite antennas to the surface of the ocean and back combined with precise satellite location data yielded Sea Surface Heights (SSH) (The Climate Data Guide: AVISO, 2016). Sea Level Anomaly (SLA) at a certain location of the ocean surface, defined by latitude and longitude, and time of the year, is the difference between the actual SSH and the long term or climatological mean of SSH for this particular location and this time of the year. The ADT products were obtained by adding a Mean Dynamic Topography (MDT) to the SLA field; the MDT used in the reprocessing is described in Mulet et al., 2013 (cited by QUALITY INFORMATION DOCUMENT CMEMS-SL-QUID-008-032-062). These ADT products merged data from all altimeter missions (Jason-3, Sentinel-3A, HY-2A, Saral/AltiKa, Cryosat-2, Jason-2, Jason-1, T/P, ENVISAT, GFO, ERS1) from 1993 to date (CMEMS, <http://marine.copernicus.eu/>). Quite a number of corrections were applied to the original data sets from instrumental errors (e.g. mispointing correction), environmental and sea state errors (e.g. presence of water vapor in the atmosphere) to geophysical corrections (e.g. geoid, ocean tides, effects related to inverse barometer, wind and pressure) (QUALITY INFORMATION DOCUMENT CMEMS-SL-QUID-008-032-062).

### Data: Oceanic Niño Index

The Oceanic Niño Index (ONI) is a 3 month running mean of Extended Reconstructed Sea Surface Temperature (ERSST.v5) anomalies in the Niño 3.4 region (5°N-5°S, 120°-170° W)], based on centered 30-year base periods updated every 5 years. An ONI value of above (below) the +0.5 °C (- 0.5°C) threshold for at least 5 consecutive months corresponds to an



El Niño (La Niña) event (National Oceanic and Atmospheric Administration, NOAA). ONI data from 1993 to 2018 were extracted from the NOAA website [http://origin.cpc.ncep.noaa.gov/products/analysis\\_monitoring/ensostuff/ONI\\_v5.php](http://origin.cpc.ncep.noaa.gov/products/analysis_monitoring/ensostuff/ONI_v5.php). The main contributions to ERSST stem from the International Comprehensive Ocean-Atmosphere Data Set (ICOADS) and include measurements made from ships as well as moored and drifting buoys, among others.

Data Processing: Absolute Dynamic Topography.

In this manuscript daily means from 1 January until 31 December 2018 have been used; continents and larger islands were blanked out by CMEMS. The horizontal resolution of the fields of ADT was  $\frac{1}{4} \times \frac{1}{4}^\circ$  on a regular latitude x longitude grid. Monthly means were computed from the daily means. For some grid points valid monthly means of ADT were not available for all months of the time series owing to the satellite mission or due to a complete or partial sea-ice coverage. In this analysis, grid points were only considered when valid monthly means of ADT existed for each month in the period 1993-2018. In addition, the polar oceans poleward of  $67^\circ$  N/S were excluded in this study resulting in a database of permanently ice-free ocean (Figure 1). In addition, annual mean ADT was calculated from the monthly means for all grid points.

In the course of the calculations of time series of mean ADT for specific areas, monthly or annual, like central/cores of subtropical gyres, whole ocean basins or the global ocean, area weighted means of ADT were computed owing to the fact that the area represented by any grid point depends on its latitude decreasing from the Equator to the poles. In the case of monthly area weighted means, the seasonal cycles from these time series of area weighted mean of ADT were removed through the application of a forward and backward 12 months running mean – the first and the last year of the time series were lost but the monthly resolution was sustained instead of working with the annual area weighted means alone. In particular, monthly mean area weighted times series of ADT were computed for global permanently ice-free ocean, the North and South Pacific oceans, the centers or cores of the Pacific subtropical gyres (NPG, central North and SPG, central South Pacific gyres) and their eastern boundaries (CCS, California Current System and HCS, Humboldt Current System) (Figure 1). The centers/cores of the Pacific subtropical gyres were identified according to the pattern of the mean ADT (1993-2018), i.e. the centers of maximum ADT, both were located on the western side of the respective basin occupying parts of the tropical and subtropical

zones, in line with the very well established westward intensification of the subtropical gyres in general (e.g. Miller et al., 1998). The eastern boundaries of the subtropical gyres corresponded to the California Current System in the northern hemisphere and to the Humboldt Current System in the southern one; both were located in about the same zonal bands as the center/cores of the gyres but extended somewhat more poleward.

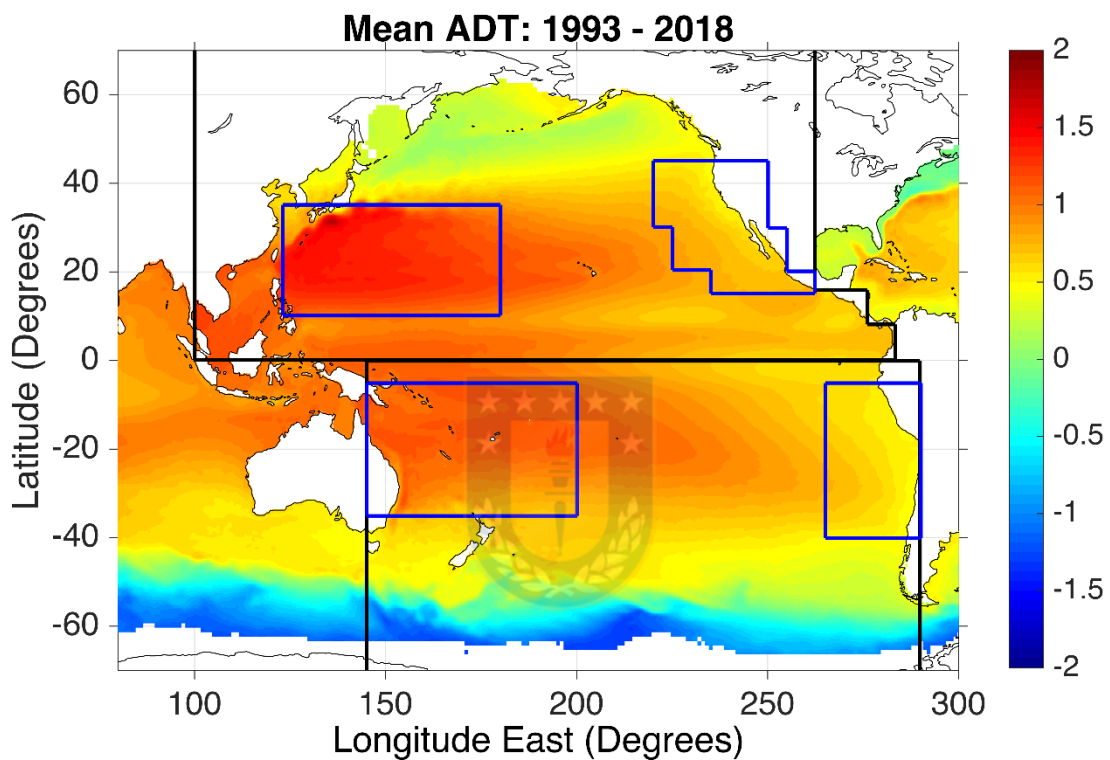


Figure 1: Mean ADT. Color-coded mean ADT 1993 – 2018. The color bar on the right hand side of the figure relates color to ADT in units of meters. The black “boxes” encompass the north and south Pacific Oceans, as defined in this study; the blue boxes mark the centers of the subtropical gyres in the West and their eastern boundaries (boundary currents) in the East.

#### Methods: A Measure for the Strength of the Subtropical Gyres (SoS)

Meridional geostrophic velocity,  $v$ , between two locations, in general, can be derived from the ADT, according to an algorithm put forward by Le Traon and Morrow (2001), using the geostrophic relationship:  $v = - (g \Delta \text{ADT}) / (f \Delta x)$ , where  $g$  is the acceleration due to gravity,  $f$  is the Coriolis parameter, and  $\Delta x$  is the eastward distance. When applied to the large scale oceanic circulation, the difference in sea level between the centers/cores of the subtropical

gyres (NPG and SPG) and its eastern boundaries (CCS and HCS) directly relates to the intensity of the gyres' circulation manifested by its geostrophic currents (e.g. Yu et al, 2014). The intensity of the circulation of the gyres was studied in more detail by constructing and scrutinizing a robust measure for the strength of the gyres' circulation. This measure for the strength of the circulation of the subtropical gyres, is the difference between the monthly mean ADT of its centers/cores minus the ADT of its eastern boundaries after the annual cycle was removed, and then divided by the zonal distance between both, here referred to "SoS" =  $\Delta \text{ADT} / \Delta x$ . This measure then was standardized to a change of ADT per 10.000 km in order to allow a direct comparison between both gyres. The SoS measure was applied to annual means and seasonally adjusted monthly means, as well.

#### Methods: Empirical Mode Decomposition

Empirical Mode Decomposition (EMD) is a method for analyzing nonlinear and non-stationary time series within the time domain and was developed by Huang et al., 1998. EMD decomposes the time series into a finite number of intrinsic mode functions based on the local characteristics of the data (Huang et al., 1998). The individual intrinsic mode functions are separated from the input signal by means of an iterative process. The envelope for local maxima and the one for local minima are estimated, their mean determined and subtracted from the input signal to obtain the first intrinsic mode function. This process then is repeated until the residuum contains not more than one local extreme. This residuum here is considered to stand for or represent the long-term (span of the time series) residual trend of the input time series (e.g. Wu et al., 2007).

#### Methods: Inter-annual components of the anomalies of volume estimates

In addition, for each valid grid point, the volume associated with its ADT was calculated by multiplying monthly mean ADT with the area each grid point represents according to its geographic location and the horizontal resolution of the ADT fields. For each grid point and all time steps then the monthly climatology of the volume estimates were subtracted from the individual volume estimates yielding the anomalies of the volume estimates. Finally, intra-annual fluctuations were removed from the anomalies of the volume estimates by applying a 12 months forward and backward moving average filter, which resulted in the inter-annual components of the anomalies of the volume estimates.

## Results

### Global and Pacific Ocean Sea Level Rise

The temporal evolution of area weighted monthly means of ADT for the permanently ice free global oceans illustrated an annual cycle with a slightly variable amplitude of about 1 cm which was superimposed by an unmistakable pronounced long-term trend (Figure 2). Global sea level in the permanently ice free ocean based on the area weighted annual means of ADT rose by 7.8 cm from 1993 to 2018 (Table 1), which corresponded to a mean annual rise of 3.12 mm per year. Nevertheless, differences in the annual rate of global sea level rise could be observed. Sea level increased by 3.6 cm from 1993 to 2006 (2.7 mm per year), with variable annual rates between 0.72 to 4.0 mm, but amounted to 4.2 cm between 2006 and 2018 (3.5 mm per year); in the latter period the annual rates fluctuated between -0.5 and 9.5 mm with > 9 mm registered during 2012/11 and 2015/14. The annual cycle was removed from the time series of the monthly means via the application of a forward and backward 12 months moving average filter and is displayed in Figure 2, the blue solid line. The filtered time series passed through all annual means and thus successfully removed the annual cycle present in the monthly means. The linear trend model explained more than 98% of the variance of the time series founded on the annual means of area weighted ADT and thus is a good estimation of the observed trend, however somewhat overestimated (underestimated) the monthly time series in which the annual cycle was removed, for the years 2007 – 2011 (2015 - 2018). The linear trend model resulted in a global sea level rise for permanently ice-free ocean of  $7.68 \pm 0.58$  cm (95% confidence interval) with  $p \ll 0.001$  for the 1993 to 2018 period (Figure 2 and Table 1). The computation of sea level rise still yielded 7.32 cm when employing the average ADT of the last and first 3-years of satellite altimeter observations.

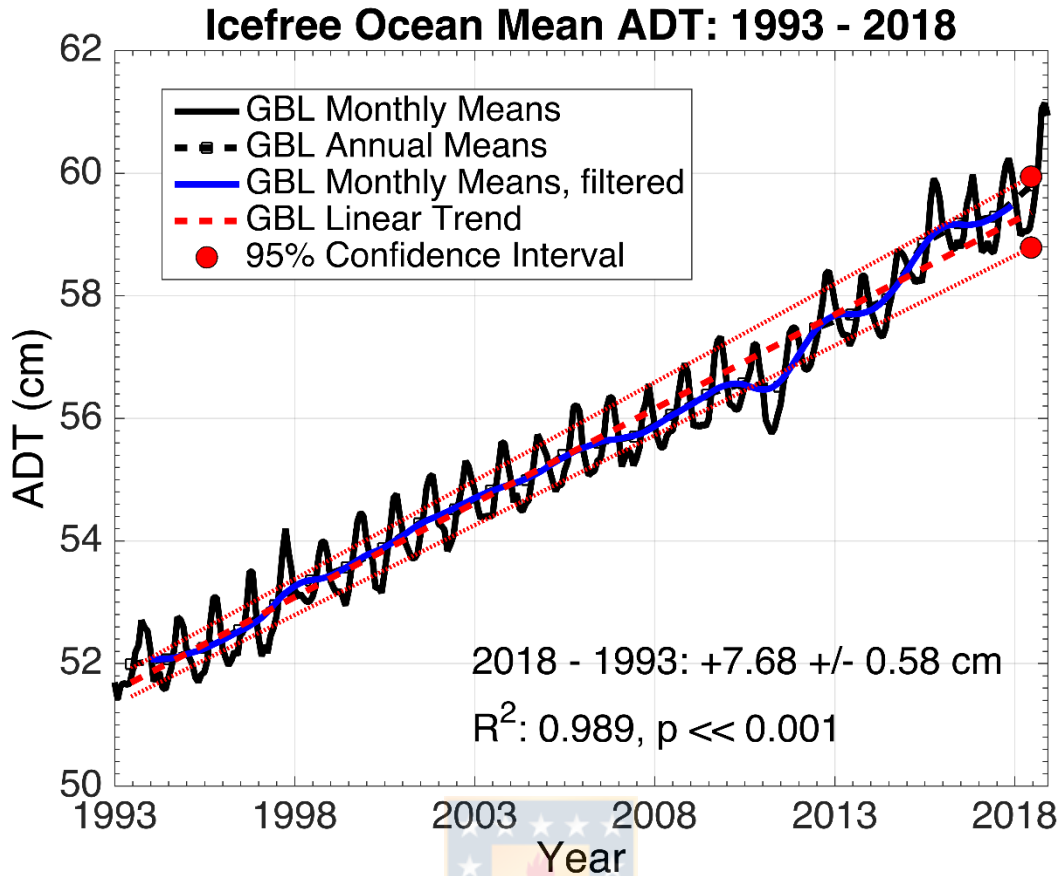


Figure 2: Global (GBL) Ocean Sea Level Rise. Evolution of monthly mean ADT in global permanently sea ice free ocean (black solid line): 1993-2018; the blue solid line stands for the 12-months forward/backward running mean of the monthly means: 1994-2017; the annual means are shown as black squares and are connected with a dashed black line – Global Ocean Sea Level rose by 7.8 cm from 1993 to 2018 based on the annual means. The dashed red line represents the linear regression model based on the annual means; sea level rise resulted in 7.68 +/- 0.58 cm applying 95% confidence bounds.

Table 1. ADT Sea Level Rise (cm) 1993 to 2018 founded on the area weighted annual means.

	Global	North P.	N.P.Gyre	CCS	South P.	S.P.Gyre	HCS
Mean	55.53	84.24	122.17	68.86	61.92	103.33	59.42
2018-1993	7.80	7.23	8.14	2.29	7.93	11.41	4.92
2016/17/18 - 1993/94/95	7.32	7.48	8.00	4.54	7.15	8.62	5.81
Lin. Trend 1993 to 2018	7.68	7.13	7.38	4.18	7.65	9.54	5.19
+/-	0.58	1.23	4.52	5.82	1.47	3.12	3.55
R <sup>2</sup>	0.989	0.942	0.565	0.201	0.930	0.821	0.511
p	< 0.001	< 0.001	< 0.001	0.022	< 0.001	< 0.001	< 0.001

Sea level rise in the North and South Pacific Oceans were in the order of the global oceans' sea level change considering all the three measures used in this study: the difference in annual means 2018 versus 1993, the difference of the average sea level of the last three years minus the first three years, 2016/17/18 versus 1993/94/95, and the linear regression models, although the North Pacific ocean fell short by about 0.5 cm in the first and third measure (Table 1). Regional sea level rise within the Pacific Ocean, however, was quite variable. First of all, sea level increased in as good the entire Pacific Ocean, despite a smaller region within the vicinity of the Antarctic Circumpolar Current between 50-60°S and 120-160°W (Figure 3). The rate of sea level increase though differed a lot; several “hot spots” with average sea level rise above 5 mm/year could be identified. The poleward boundaries of the cores of the subtropical gyres expanded the most, followed by their equator-ward boundaries, which correspond to the Indonesian warm water pool of the western equatorial Pacific, and then third in place the centers of the gyres as well. The Eastern Pacific Ocean, in both

hemispheres, in contrast, exhibited the lowest rates of sea level increase founded on the linear trend analysis.

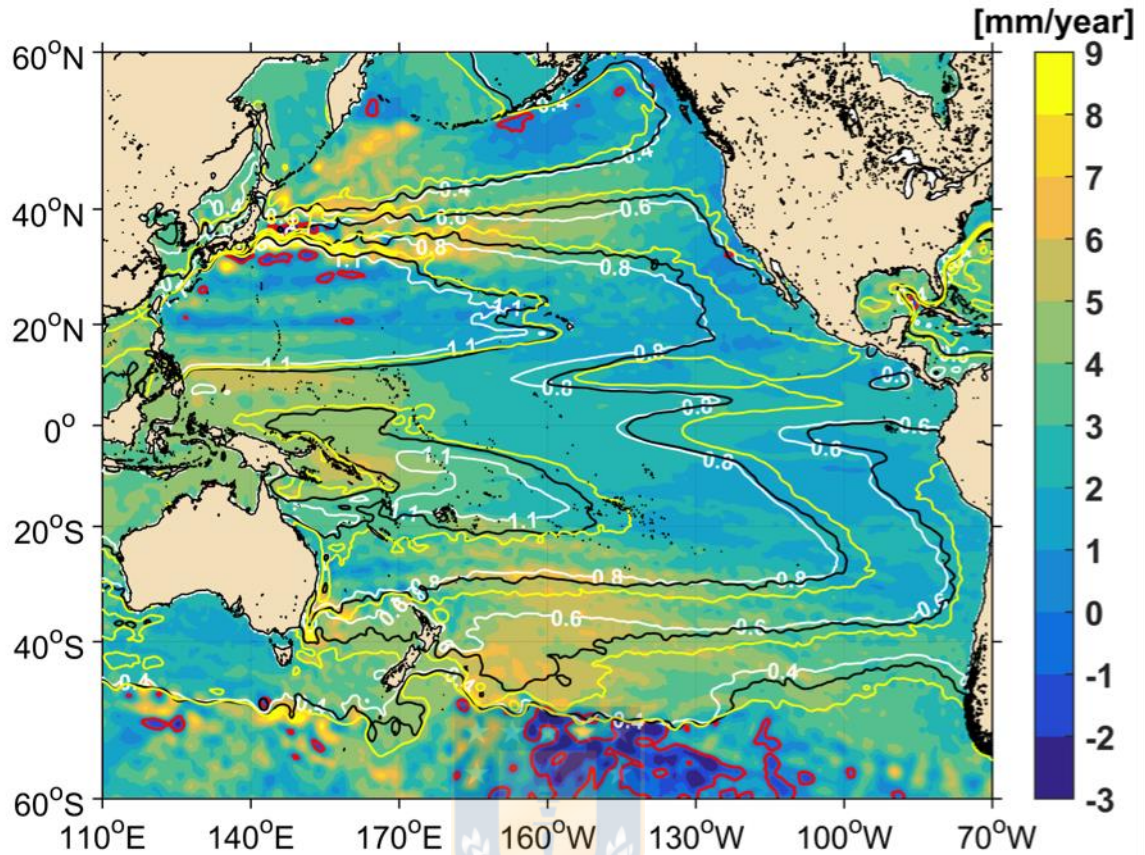


Figure 3: Sea level rise in the Pacific Ocean from 1993 to 2018. The linear trend in units of mm/year was calculated for all grid points within the field of ADT and is color-coded according to the colorbar displayed on the right hand side of the Figure. Contours refer to ADT in units of meters; the white contour lines correspond to average ADT for the years 1993-96, the black contour lines to average ADT for the years 2015-18, and the yellow contour lines to 2015-18. The red contour lines indicate no change in sea level.

### Sea level rise in the Centers/Cores and the eastern Boundaries of the Pacific Subtropical Gyres

The typical annual cycles in sea level time series (Figure 4a, thin solid lines) were removed from the time series of monthly mean ADT for the cores of the North and South Pacific Subtropical Gyres (Data and Data Processing, thick solid lines in Figure 4a) and the seasonally adjusted time series were studied together with the annual means derived from the monthly means (black squares connected with black dashed lines in Figure 4a).

Mean (1993-2018) sea level in the center/core of the North Pacific subtropical gyre was 122.2 cm (with a standard deviation of 3.0 cm) and thus about 20 cm higher than in the center/core of the South Pacific counterpart, which resulted in 103.3 cm (with a standard deviation of 3.2 cm). The evolution through time of the ADT of the centers/cores of both subtropical gyres underwent a significant trend in sea level rise. The linear regression model yielded a gain of 7.38 +/- 4.52 cm (95% confidence bounds) for the North Pacific and 9.54 +/- 3.12 cm for the South Pacific, more than 2 cm than in the core of the North Pacific subtropical gyre. Similar sea level rises were obtained when subtracting the annual mean of the first year (first 3 years) of the time series (1993 to 2018) from the last year's mean (last 3 years), namely 8.14 cm (8.0 cm) for the North Pacific subtropical gyre and 11.4 cm (8.6 cm) for the South Pacific (Figure 4a and Table 1). Sea level rises in the centers/cores of both subtropical gyres exceeded those of the basins' mean, by about 1 cm for the North Pacific and 2 cm for the South Pacific, slightly depending on the measure used (Table 1).

The linear regression model only could explain about 56% of the variance of the time series of annual means of the North Pacific but 82% of the South Pacific's time series, owing to substantial inter-annual fluctuations. Minima seasonal adjusted monthly mean ADT in the center/core of the North Pacific subtropical gyre were registered in the end of 1994, when a weak El Niño initiated, and around mid 1997, the onset of a strong El Niño. Then suddenly the most abrupt short-term increase in ADT, more than 7 cm, occurred from the mid 1997s to the end of 1998, i.e. during the strongest El Niño of the last century and the onset of the following strong La Niña. Sea level in the center/core of the subtropical gyre then remained relatively unchanged till the end of 2012, coinciding with the Hiatus period of global warming (Trenberth et al. 2014). It afterward dropped by 4 cm till the end of 2015, the peak of this decade's very strong El Niño, and subsequently re-bounced with a gain of 5 cm by the end of 2018. The monthly time series of ADT of the South Pacific subtropical gyre, after the annual cycle was removed, was like in the North Pacific not strictly monotonically increasing but performed some noteworthy dives (2-4 cm) related to the 1997/98 (strong), 2009/10 (moderate), and 2015/16 (strong) El Niño events after which the rising trend was restored just within two to three years. Sea level evolution in the center/cores of both subtropical gyres, hence, followed the same pattern, ENSO imposed fluctuations combined with a trend.



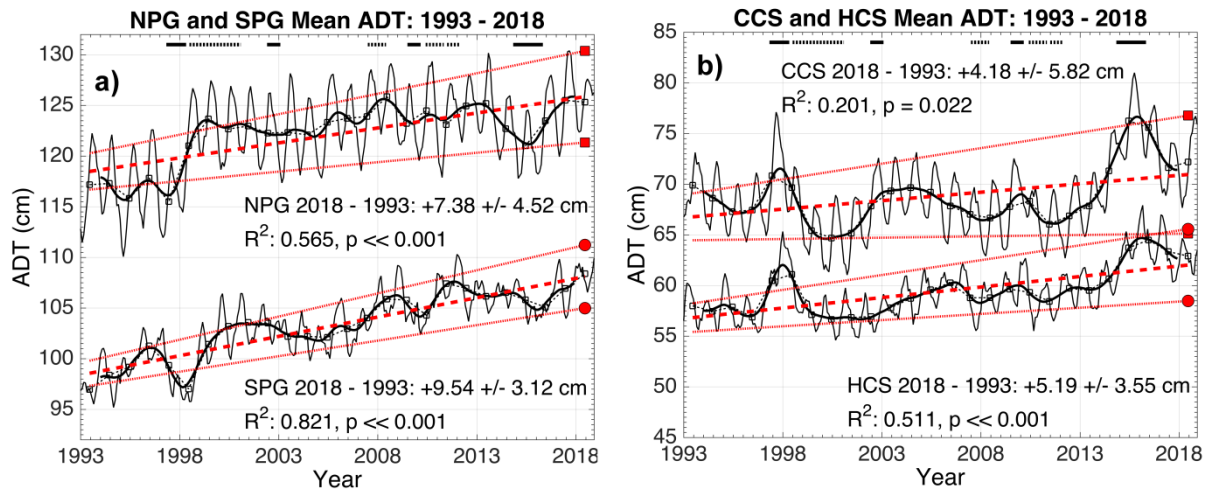


Figure 4: Evolution of ADT 1993-2018 within a) the North and South Pacific Central Subtropical Gyres and b) the California and Humboldt Current systems. Monthly mean ADT (black thin solid lines); 12-months forward/backward running mean of the monthly means (1994-2017, black thick solid lines); annual means (black squares connected with a dashed black thin line); linear regression model based on the annual means (red dashed thick line); lower and upper 95% confidence bounds for linear regression (dotted red lines). El Niño (La Niña) phase are underlined by solid (dotted) horizontal lines in the upper part of both panels.

Sea level was lower at the eastern boundaries of the subtropical gyres, following the nature of the gyres' dynamic. Mean sea level amounted to 69 cm with a standard deviation of 2.9 cm for the California Current System and mean ADT in the Humboldt Current system resulted in 49.4 cm with a standard deviation of 2.2 cm, being about 20 cm less than the North Pacific counterpart, similar to the cores of the gyres. Sea level in the California Current system (Figure 1), during the satellite altimetry period, rose by just 2.3 cm, close to 5 cm less than the core of the North Pacific subtropical gyre based on the annual means (Table 1 and Figure 4b). The difference in sea surface height rose to 4.5 cm when taking the first and last 3 years of the time series into account (Table 1). The linear trend model (+4.2 +/- 5.8 cm) was just slightly significant at the 95% confidence level, but only could explain about 20% of the variance of the time series of annual means, owing to large superimposed inter-annual fluctuations.

Sea level rise in the Humboldt Current system for the 1993-2018 period, 4.9 cm, fell shy from the global ocean's trend by about 3 cm based on the annual means, and was more than 6

cm less than the core's gain. Sea level rose by 5.8 cm when taking the first and last 3 years of the time series into account. The linear trend model yielded a gain of 5.2 cm (+/- 3.6 cm), was significant on the 95% level but only could explain 51% of the variance of the annual means compared to 82% for the core of South Pacific gyre.

The evolution of monthly mean ADT in the eastern boundary systems of the Pacific Ocean, after the removal of the annual cycle (solid thick black lines in Figure 4b), were not monotonically increasing as likewise noted for the centers/cores of the North and South Pacific gyres. The prominent observed features, however, were not dives, or relative minima, like in the centers of the Pacific gyres but short term (lasting for about two to three years) rises, or relative maxima, of up to 5 cm followed by subsequent falls in about the same order related to the occurrence of strong El Niño events of the last 25 years (1997/98 and 2015/16); for weak and moderate events (e.g. 2009/10) the rises and falls were in the order of up to 2 cm. The centers/cores of the Pacific gyres were characterized by a decline in sea surface height during El Niño events whereas the eastern boundary systems recorded a surge, especially related to strong events. In the temporal evolution of the ADT of the centers of the Pacific gyres and the ADT of the California and Humboldt Current Systems, in general, an anti-cyclical behavior has been noted. Relative maxima (minima) in the seasonal adjusted monthly mean ADT time series were associated with El Niño (La Niña) events, the stronger the events were the larger were the extremes (absolute 2-5 cm).

### **The Strength of the Subtropical Gyres (SoS): Fluctuations and Trends**

Any differential change in sea level in the centers/cores of the subtropical gyres versus in its eastern boundaries directly implies an adjustment of the gyres' circulation owing to an alteration of the zonal hydrostatic pressure gradients, which are proportional to geostrophic currents. This can result in acceleration or slowdown of the circulation of the gyres. The strength of the Pacific's gyres' circulation through time from 1993 to 2018 was studied in detail by applying the SoS measure as defined in the Data and Methods section and is depicted in Figure 5a. On average the SoS value for the North Pacific subtropical gyre exceeded with 62.5 cm per 10.000 km zonal distance the value for the South Pacific by about 50% (Table 2), meaning that the strength of the former one is by far more intense than the latter (Solid lines in Figure 5a). The northern hemisphere's subtropical gyre also surpassed its southern counterpart in the magnitude of fluctuations showing a range of 17 cm versus 13 cm

per 10.000 km zonal distance occurring during time spans of 3-5 years. These fluctuations were substantially larger than the variations in sea level observed for the centers/cores and the eastern boundaries of the gyres, as well, owing to the anti-cyclical behavior of ADT within both extremes, which amplified the fluctuations in the SoS measure. The evolution through time (periods of slow down and acceleration) of the SoS measure for both gyres, nevertheless, was surprisingly quite similar.

The strength of both gyres was weakest during the occurrence of El Niño events in the end/beginning of 1997/98 (very strong El Niño) and in the end/beginning of 2015/16 (strong El Niño). The circulation of both gyres was strong, otherwise, especially during the La Niña periods 2000/2002 and 2010/2012, but suffered some intensity related to periods of weak to moderate El Niño events, i.e. end of 2002 and in the end/beginning of 2009/10; ENSO obviously modulated the strength of the gyres.

### **Trends**

The SoS measure indicated that both gyres intensified from the onset of the satellite altimetry era, January 1993, till December 2018, in all three differencing schemes tested (Table 2). The SoS measure for the North Pacific subtropical gyre showed a gain of 6.8, 6.9, and 4.0 cm per 10.000 km, in the SoS difference between the means of the last and first year, the means of the last three and first three years, and December 2017 minus January 1993, respectively. For the South Pacific, applying the same schemes, the differences were 6.0, 2.6, and 3.9 cm per 10.000 km. A linear regression model, based on annual means, and operated on the SoS measures of both gyres, likewise, resulted in an intensification of the circulation of both gyres, of 3.7 cm per 10.000 km for the northern basin and 4.0 cm per 10.000 km for the southern one, from 1993 to 2018 (Table 2). However, in both regression analyses high uncertainties were involved and also the linear trend model could only explain 5% and 18% of the variance of the SoS measures for the North Pacific and South Pacific subtropical gyres, respectively.

Table 2. SoS estimates for both subtropical gyres of the Pacific (Units are in ( $\Delta$  cm per 10.000 km zonal distance) considering the averages of last minus first year, last three minus first three years, and the linear trend of the 1993 to 2018 satellite altimetry observations.

	North Pacific	South Pacific
Mean SoS $\Delta$ cm per 10.000 km	62.5	40.9
+ Range	6.5	4.5
- Range	10.4	8.2
Dec 2017 – Jan 1994	6.9	3.9
2018 – 1993	6.8	6.0
2016/17/18 - 1993/94/95	4.0	2.6
Linear Trend 1993 to 2018	3.7 +/- 11.2 $R^2 = 0.052, p = 0.263$	4.0 +/- 5.9 $R^2 = 0.186, p = 0.020$

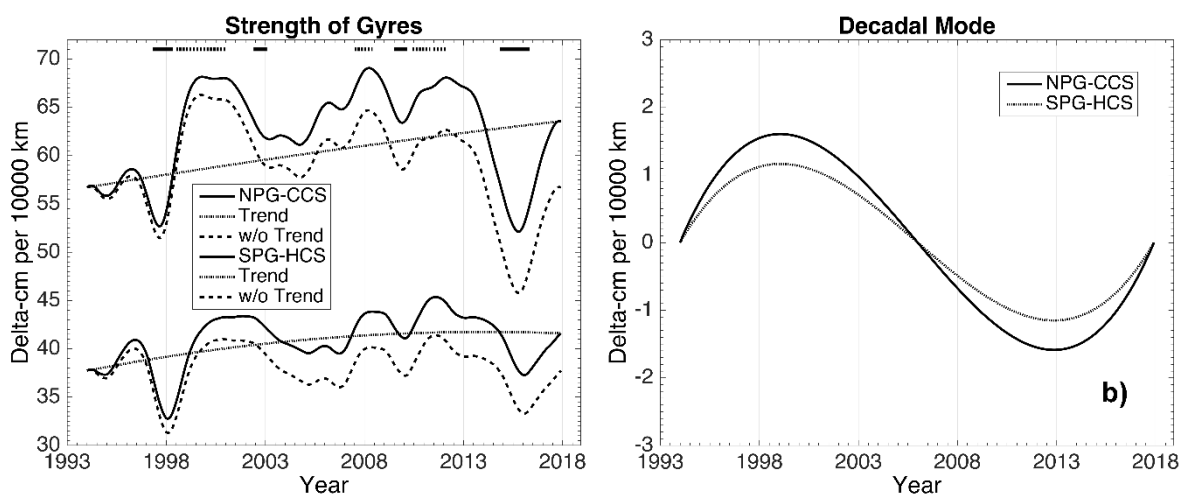


Figure 5: a) SoS measures for the North (upper) and South (lower) Pacific subtropical gyres (solid lines). The residuum or trends for the period of observation based on Empirical Mode

Decomposition, EMD, (last mode obtained) are shown as dotted lines. The dashed lines refer to the SoS measures having the trend removed. b) The second to last EMD modes for both gyres, which refer to a decadal oscillation. El Niño (La Niña) phase are underlined by solid (dotted) horizontal lines in the upper part of panel a).

### **Empirical Mode Decomposition**

The low percentage of variance the linear regression models only could explain of the variance of the SoS measures for both gyres suggested the presence of other modes of climate variability. Empirical mode decompositions were employed instead and were performed on the monthly mean SoS measures. The EMDs resulted in 5 intrinsic mode functions for the measure of strength of the North Pacific subtropical gyre and in 6 modes for the South Pacific counterpart. The last modes of both decompositions of the SoS time series were the residuum or trend within the time span of observation (Figure 5a, dotted lines). The residuum or trend for the North Pacific subtropical gyre resulted in an as good linear trend associated with a gain of 6.9 cm per 10.000 km from January 1993 to December 2017 (Table 2). For the South Pacific subtropical gyre the trend followed a slightly concave curve and reported a gain of 3.9 cm per 10.000 km from January 1993 to December 2017 (Table 2). To illustrate the impact the trend had on the strength of the gyres' circulation the trends were subtracted from the original SoS measure and are depicted as dashed lines in Figure 5a. The weakening of both gyres intensity during the last strong El Niño event 2015/16 without the trends in place would have been much more severe. In both EMDs the second last mode uncovered a decadal mode, which strengthened (weakened) both gyres during the first (second) half of the period of observation (Figure 5b) being with about 1.5 cm per 10.000 km more prominent in the North Pacific compared to approximately 1.0 cm per 10.000 km in the South Pacific.

### **ENSO and the Strength of the Subtropical Gyres (SoS)**

After the identification of the trends and the decadal modes in the SoS measures, these were subtracted from the SoS measures, and were further scrutinized. The synchronized behavior in the temporal evolution of both reduced measures just judging by eye is evident, e.g. the occurrence of the relative minima and maxima in time, the change in curvature or the rises and falls (Figure 6). Since our SoS measure was constructed upon the phase conserving 12-month forward/backward moving average of mean monthly ADT of the centers/cores and

eastern boundaries of the subtropical gyres the same filter was applied to Oceanic Niño Index. The presence of the ENSO mode in these reduced measures for the strength of the North and South Pacific subtropical gyres likewise was obvious, although some out of phase behavior could be noted. The most important observation was that the strength of both subtropical gyres weakened sharply (moderately), by up to 25% during strong (moderate) El Niño events, and were reinforced during La Niña episodes.

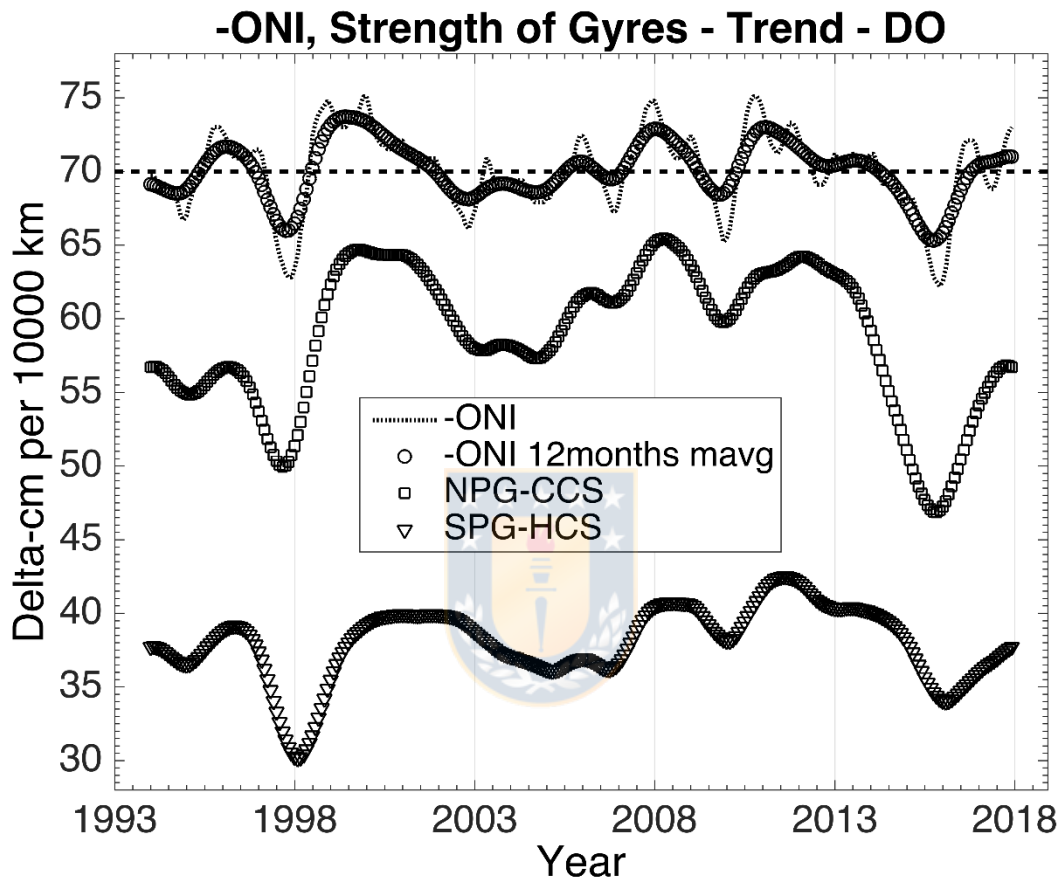


Figure 6: The upper time series are the reversed or negative ONI (dotted line) and its phase conserving 12-month forward/backward moving average (circles) expressed in  $^{\circ}\text{C} + 70$ . The time series in the middle is the SoS measure for the North Pacific subtropical gyre (squares), and the lower one corresponds to the South Pacific subtropical gyre (triangles).

Cross-correlation analysis between the time series of the filtered ONI and the reduced SoS measures were performed in order to shed light on this out of phase behavior. Extra care was taken in the computation of the confidence bounds. The classic confidence bounds (L) for a 95% and 68% significance level in cross-correlation analysis is  $L = \pm 1.96 / \sqrt{n}$  and  $\pm 1.0 / \sqrt{n}$ , respectively, where  $n$  is the number of elements in the time series minus the lag considered and were used in Figure 7 as dashed lines for the 68% significance level. These

confidence bounds imply an only weak positive auto-correlation present in the two time series to be analyzed which is not the case here. Spurious correlations can occur between auto-correlated series ( $> 0.8$ ) when the classic confidence bounds were applied (Cryer and Chan, 2008, cited by Dean and Dunsmuir, 2016). Cryer and Chan, 2008, proposed to adjust the classic confidence bounds by multiplying  $L$  with  $F$ ,  $F = \sqrt{(1+ab)/(1-ab)}$ , with  $a$  and  $b$  being the auto-correlation coefficients at lag 1 of the series involved in the computation of the cross-correlation; the new confidence bounds  $L \cdot F$  were drawn in Figure 7 as dotted lines for the 68% significance level for the North and South Pacific gyres

Cross correlation analysis was carried out between the reversed ONI after a phase preserving 12-month forward/backward moving average was applied, as depicted in the upper time series of Figure 6, and the reduced SoS measures, Figures 7a and 7b, respectively. Significant cross correlations could only be established on the 68% confidence level owing to the high degree of auto-correlation of all involved time series ( $L(68\%) = 0.059$ ,  $F(\text{North Pacific}) = 12.54$ ,  $F(\text{South Pacific}) = 12.06$ ). Nevertheless, the cross correlation analyses showed different results for the two ocean basins. The circulation in the North Pacific responded to ENSO within one to two month after its occurrence, whereas the South Pacific only after five to six months. ENSO could explain 65% and 56% of the variance of the strength of the North and South Pacific gyres at these lags, respectively.

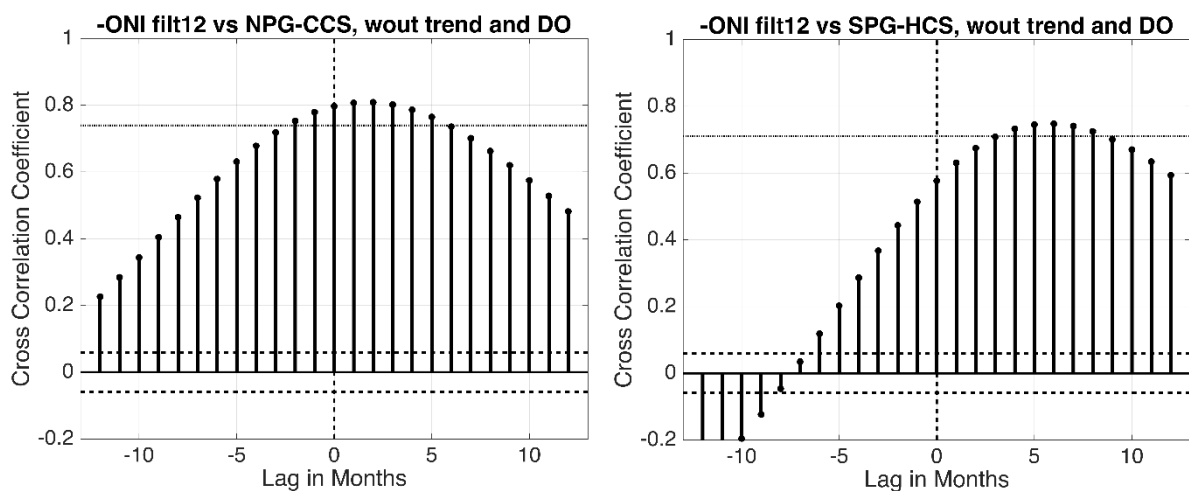


Figure 7: Cross correlation functions a) for the North Pacific subtropical gyre, between the Oceanic Niño Index (12-month moving average) and the SoS measure after the removal of the trend and the decadal oscillation. b) for the South Pacific subtropical gyre, between the Oceanic Niño Index (12-month moving average) and the SoS measure after the removal of the trend and the decadal oscillation. For both figures, the dashed lines are the classic

confidence bounds,  $L$ , for a 68% significance level; the dotted lines correspond to the recomputed confidence bounds  $L \cdot F$  taking the high degree of auto-correlation of the two time series into account.

### A mechanism for the growth of the South Pacific Subtropical Gyre

In order to shed light on the extreme growth of the South Pacific Subtropical gyre, the inter-annual components of the anomalies of the volume estimates (Data and Data Processing) were summed up from 150 – 225 °E for all 0.25° latitude bands from the Pacific Equator to 60°S, and from January 1993 to December 2018. This way, possible meridional transport of volume within the western South Pacific (general circulation and Ekman transport) could be monitored, although zonal displacements/motions/advections were depressed. A latitude/time presentation of these volume estimates was used to illustrate the swelling of the subtropical gyre and its poleward boundary (Figure 8). Volume and hence sea level in the western South Pacific gradually increased (color changed from blue [-15 e+9 m<sup>3</sup> per 0.25° latitude band] to green, yellow and red [15 e+9 m<sup>3</sup> per 0.25° latitude band]) as already has been seen in Figure 3 in terms of ADT rise. Volume increased most in the southern Indonesian Warm Pool, the equator-ward boundary of the gyre, followed by the subtropics, 20 – 50 °S, by the end of 2018. Water was injected over the years mainly from the Warm Pool into the latter region, e.g. 1994 – 1999 and 2005 – 2015 (white arrows in Figure 8), but also was imported from the sub-polar regions, e.g. 2003 – 2012, apparently owing to the melting of Antarctic Ice-sheet and/or the calving of glaciers.

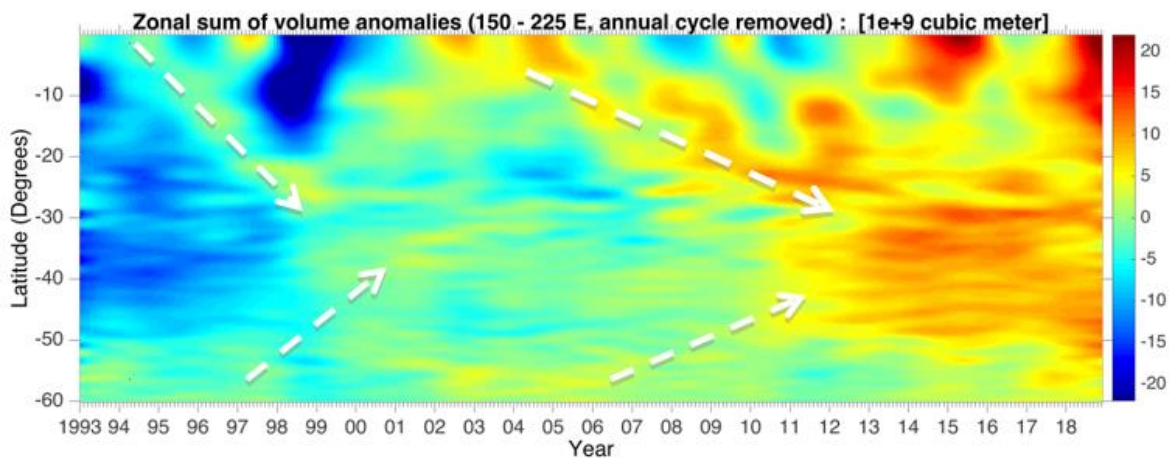


Figure 8: The inter-annual components of the anomalies of the volume estimates (Data and Data Processing) were summed up from 150 – 225 °E for all 0.25° latitude bands from the



Pacific Equator to 60°S, and from January 1993 to December 2018. The volume estimates are color coded according to the colorbar on the right hand side of the figure;  $1e+9$  m<sup>3</sup>.

## **Discussion**

The merit of the SoS measure to quantify the strength of the circulation of the Pacific subtropical gyres, which is proposed in this study, was tested against the findings which described an intensification in the circulation of the South Pacific subtropical gyre from 1993 to 2003/04, and a continuation of this trend till 2014, put forward by Roemmich et al., 2007 and 2016. In the first paper, the authors stated an increase of the circulation of the South Pacific subtropical gyre between 1993 and 2004, and an increase in sea surface height of 12 cm, which peaked in 2003, centered at about 40° S and 170° W, and which was collocated with the deep center of the gyre. This, as stated by the authors, corresponded to a 20 % increase in the counterclockwise circulation of the gyre. Our SoS measure, which has a monthly resolution in time, increased by 15% from 1993 to 2002, from where it slightly declined to 12 % in 2003 and to 7% in 2005, nevertheless being in good agreement with the analysis carried out by Roemmich et al., 2007; certain differences in both analyses might be due to averages over time.

Another hike, in the SoS measure, from 2005 on, was observed till 2012 from which on it declined to its 1993 strength till the end of 2015. Nevertheless, in the beginning of 2014, the SoS measure still was found above its 2005 level. Similarly, Roemmich et al., 2016, found the geostrophic circulation across 35° S, from 160° W to South America, being enhanced by 5 Sv.

## **Acknowledgements**

National Center for Atmospheric Research, NCAR, Boulder, Colorado, USA.

Copernicus Marine Environment Monitoring Service (CMEMS), EU.

Freddy Hernández-Vaca thanks the sponsorship of the scholarship contract No 20090315 between Secretaria de Educación Superior, Ciencia, Tecnología e Innovación (SENESCYT), Instituto Oceanográfico de la Armada (INOCAR); as well as the resolution INOCAR-RHU-2016-040-O.

## **References**

Cryer, J. D. and Chan, K., 2008. Time series analysis with applications in R. New York, NY: Springer.

Dean, R. T., and Dunsmuir, W. T., 2016. Dangers and uses of cross-correlation in analyzing time series in perception, performance, movement, and neuroscience: The importance of constructing transfer function autoregressive models. *Behavior research methods*, 48(2), 783-802.

Huang, N.E., Shen Z., Long S.R., Wu M.C., Shih, H.H., Zheng Q., Yen N.C., Tung C.C., and Liu H.H., 1998. The empirical mode decomposition and the Hilbert spectrum for nonlinear and non-stationary time series analysis. *Proc. R. Soc. Lond A* 454, 903-995.

Le Traon, P. Y., and R. Morrow (2001), Ocean currents and eddies, in *Satellite Altimetry and Earth Sciences*, edited by L. L. Fu, and A. Cazenave, pp. 171– 215, Elsevier, San Diego, Calif.

Miller, A. J., Cayan, D. R., and White, W. B., 1998. A westward-intensified decadal change in the North Pacific thermocline and gyre-scale circulation. *Journal of Climate*, 11(12), 3112-3127.

Mulet, S., Rio, M. H., Greiner, E., Picot, N., and Pascual, A. 2013: New global Mean Dynamic Topography from a GOCE geoid model, altimeter measurements and oceanographic in-situ data, OSTST Boulder USA 2013, available at: [http://www.aviso.altimetry.fr/fileadmin/documents/OSTST/2013/oral/mulet\\_MDT\\_CNES\\_CLS13.pdf](http://www.aviso.altimetry.fr/fileadmin/documents/OSTST/2013/oral/mulet_MDT_CNES_CLS13.pdf), 2013.

Roemmich, D., Gilson, J., Davis, R., Sutton, P., Wijffels, S., and Riser, S., 2007. Decadal spinup of the South Pacific subtropical gyre. *Journal of Physical Oceanography*, 37(2), 162-173.

Roemmich, D., Gilson, J., Sutton, P., and Zilberman, N., 2016. Multidecadal change of the South Pacific gyre circulation. *Journal of Physical Oceanography*, 46(6), 1871-1883.

Quality Information Document (CMEMS-SL-QUID-008-032-062)

<http://marine.copernicus.eu/documents/QUID/CMEMS-SL-QUID-008-032-062.pdf>

The Climate Data Guide: Aviso Satellite derived Sea Surface Height above Geoid, 2016. <https://climatedataguide.ucar.edu/climate-data/aviso-satellite-derived-sea-surface-height-above-geoid>. National Center for Atmospheric Research, NCAR, Boulder, Colorado, USA. Last modified 1 July 2016.

Trenberth, K. E., Fasullo, J. T., Branstator, G., and Phillips, A. S., 2014. Seasonal aspects of the recent pause in surface warming. *Nature Climate Change*, 4(10), 911-916.

Yu, Y., Wang, L., Zheng, Q. and Li, Z., Geostrophic current estimation using altimetric cross-track method in northwest Pacific, 2014. *IOP Conf. Series: Earth and Environmental Science* 17, 012105 doi:10.1088/1755-1315/17/1/012105.

Wu, Z., Huang, N. E., Long, S. R., and Peng, C. K., 2007. On the trend, detrending, and variability of nonlinear and nonstationary time series. *Proceedings of the National Academy of Sciences*, 104(38), 14889-14894.



## 5 DISCUSIÓN

El objetivo general de esta tesis era describir el impacto de la variabilidad climática en la circulación de los giros subtropicales así como impactos a propiedades físicas, masas de agua en la región del Sistema de Corriente de Humboldt. El tema fue cubierto con el análisis de información oceanográfica (superficial y subsuperficial) y meteorológica.

En escala global el nivel del mar, de las regiones sin cobertura de hielo, aumentó 7.8 cm entre 1993 y 2018, que corresponde a una razón anual promedio de 3.12 mm por año. Es interesante observar la diferencia entre regiones del Pacífico o sus respectivas subdivisiones del Norte, Sur, ambos giros subtropicales y sus respectivas regiones orientales; (Resultados Capítulo 1). La variabilidad regional es comparable con los resultados propuestos por Hamlintong et al. (2016), quienes mostraron que en la parte occidental del Pacífico Norte la tendencia es 1 cm/año y a lo largo de la costa oeste de Estados Unidos es cercana a cero. Resultados similares también fueron observados por Zhang y Church (2012), quienes demostraron que el aumento acelerado en la región occidental se debió en parte a la variabilidad climática mayor a diez años a escala de cuenca.

En la cuenca del Pacífico Sur también existen diferencias regionales en el aumento del nivel del mar, los mayores cambios están en la región occidental que la región oriental, Albrecht et al. (2019), en esta tesis la diferencia entre ambas regiones es de 2.81 cm entre 2016/17/18-1993/94/95.

El Niño y La Niña constituyen una fuente importante de variabilidad, con 14 eventos entre 1993 y 2006 que tuvieron una gran gama de amplitud, percosores, patrones espaciales, y diferentes duraciones, intensidades y estacionalidades (Resultados Capítulo 2); similar a lo propuesto por Capotondi et al. (2015). Otros investigadores han clasificado a El Niño y La Niña en Central y Oriental según la distribución geográfica de las anomalías de TSM (Jeong y Ahn, 2016); del material suplementario de estos autores, entre 1993 y 2014, se obtuvo que existieron 5 eventos El Niño con clasificación Oriental y 3 con clasificación Central y 4 con clasificación Oriental y 4 con clasificación Central para La Niña. La frecuencia y los tipos de eventos El Niño y La Niña estarían influyendo en los cambios y la variabilidad espacial en el nivel del mar presentado en el Capítulo 1. En el centro o núcleo de cada giro del Pacífico se caracterizó por una disminución en la altura del nivel del mar en Eventos El Niño mientras, en sus respectivas partes orientales fue un aumento, principalmente observado en los El Niño extraordinarios.

El fortalecimiento de los vientos alisios entre 2000 y 2012 es de tal magnitud que se lo relaciona con una desaceleración del calentamiento global (Merrifield y Maltrud, 2011, England, et al., 2014), pero existe una alternancia calentamiento/enfriamiento que representa la desaceleración/aceleración de los vientos alisios del Pacífico, Watanabe et al. (2014). Al

comparar los vientos en los dos escenarios, El Niño y La Niña (Resultados Capítulo 2), existen diferencias espaciales en ambos escenarios. Al norte de 30°S, durante El Niño, los vientos favorables a la surgencia se incrementan y al sur se debilitan, mientras que durante La Niña pasa lo contrario, en una escala interanual los cambios de los vientos alisios espacialmente en el Sistema de Corriente de Humboldt no son constantes.

En el lado oriental del Giro del Pacífico Sur, se reevaluaron los efectos de la variabilidad climática sobre el SCH. El análisis de correlación cruzada entre las anomalías de TSM y el INO mostró baja correlación (Resultados Capítulo 2), pero esta fue estadísticamente significativa, con retrasos positivos. En otras palabras, las anomalías de SST positivas o negativas ocurrieron primero en la región del SCH y luego en el Pacífico ecuatorial central, similar retraso al explicado por Hsu et al., (2018), quienes correlacionan las anomalías de TSM más al sur de nuestra área de estudio con anomalías en la región Niño 3.4, en un periodo mayor de estudio, 1870–2016. Estos autores indicaron, además, que las correlaciones están dadas por los cambios en la circulación de la Corriente Circumpolar Antártica, pues es esta corriente el principal aporte a la corriente de Humboldt.

En la subsuperficie de la región del SCH, en tres latitudes y en secciones zonales de aproximadamente 1500 km de longitud, las diferencias en el promedio ponderado de temperatura (vertical y horizontal) entre El Niño y La Niña (Resultados Capítulo 2) tuvieron su mayor amplitud hasta los 40 m de profundidad, con 0,7°C en la latitud 22,5°S y 32,5°S; en la latitud 27,5°S, sobre los 40 m las anomalías crecen y pueden y superar 1°C ; esto se debería a que se incluyó en la comparación el evento Fuerte El Niño del año 2015 con el evento moderado La Niña de 1999.

En el análisis de la tendencia del bombeo de Ekman, en la región y tiempo de formación del AIPSO, quedaron en evidencia dos periodos diferentes, 1991-2000 y 2000-2012, los que fueron desfavorables y favorables a la subducción de agua, respectivamente. Estos cambios en el bombeo de Ekman nos ayudaron a explicar los cambios en la distribución y geometría del AIPSO, la cual ha disminuido en salinidad 0,1 en promedio (Resultados Capítulo 3), por el contrario el Agua Tropical del Pacífico Sur ha tenido una disminución significativa de salinidad en su región norte y aumento en su límite sur, para el periodo 2000-2014, Zhang y Qu (2014), en otras palabras sería un movimiento hacia el sur de toda la masa de agua, movimiento que no es reflejado por el AIPSO.

## 6 CONCLUSIONES

Esta tesis colabora a nuestra comprensión del papel de la Variabilidad Climática en los Giros Subtropicales del Pacífico, con énfasis en la región oriental del giro del Pacífico Sur. Los aspectos clave de esta tesis se detallan a continuación:

El Agua Intermedia del Pacífico Sur Oriental presentó una expansión hacia el norte, al comparar el volumen ocupado en dos periodos de tiempo se obtuvo un aumento del mismo en un 53% respecto a los resultados anteriores.

En una visión completa de los Eventos ENOS en el dominio del Sistema de Corrientes de Humboldt; las condiciones físicas fueron diferentes (estadísticamente significantes) en resumen:

La variabilidad de la anomalía de TSM estuvo en el umbral de  $\pm 0.5$  ° C, El esfuerzo del viento aumentó 10% durante condiciones de La Niña en comparación con El Niño.

La corriente de Humboldt fue más fuerte en La Niña que el Niño entre las latitudes 20 y 45°S y en consecuencia la Energía Cinética fue más intensa en La Niña que en el Niño.

En el periodo total de análisis del nivel del mar, 1993-2018, globalmente en promedio existe una tendencia de 3mm/año; sin embargo, esta tendencia no es constante y se puede diferenciar periodos cortos con diferentes tendencias; de 3,6 mm/año entre 1993 y 2006 y 4,2 mm/año entre 2006 a 2018.

Los cambios temporales del nivel del mar en el centro de cada giro del Pacífico y en los sistemas de corriente de borde oriental respectivos mostraron un comportamiento anticíclico. Los máximos relativos (mínimos) en las series temporales, con ajuste estacional, se asociaron con eventos de El Niño (La Niña), cuanto más fuerte fueron los eventos, mayores fueron los extremos (2-5 cm absoluto).

El indicador del fortalecimiento de los giros subtropicales (SoS), sin el aporte de la tendencia y la variabilidad, mostró un debilitamiento brusco (moderado) hasta un 25% durante los evento fuerte (moderado) El Niño y un aumento en los episodios La Niña.

Finalmente, de acuerdo a las conclusiones mostradas, es posible aceptar la hipótesis planteada en esta tesis, la variabilidad climática dada por El Niño impacta la circulación oceánica de los Giros Subtropicales; las condiciones físicas y de masa de agua en la región oriental del Giro del Pacífico Sur. Mencionados impactos son opuestos así como lo es El Niño y la Niña.

Una limitación de este estudio radica en el hecho de no haber diferenciado el origen, periodo de inicio, duración o fin de los Evento Eventos El Niño o La Niña para establecer diferencias particulares sobre la física del Sistema de Corriente de Humboldt, se recomienda realizar esta diferencia para tener una mejor cuantificación de los impactos de la Variabilidad Climática sobre el Sistema de Corrientes de Humboldt.



## 7 REFERENCIAS

- Aiken, C. M., Castillo, M. I., and Navarrete, S. A. 2008. A simulation of the Chilean Coastal Current and associated topographic upwelling near Valparaíso, Chile. *Continental Shelf Research*, 28(17), 2371-2381.
- Albrecht, F., Pizarro, O., Montecinos, A., and Zhang, X., 2019. Understanding Sea Level Change in the South Pacific during the late 20th century and early 21st century. *Journal of Geophysical Research: Oceans*, 124(6), 3849-3858.
- Aronson, R. B., Precht, W. F., Macintyre, I. G., and Murdoch, T. J., 2000. Coral bleach-out in Belize. *Nature*, 405(6782), 36-36.
- Ashok, K., Behera, S. K., Rao, S. A., Weng, H., and Yamagata, T., 2007. El Niño Modoki and its possible teleconnection. *Journal of Geophysical Research: Oceans*, 112(C11).
- Barnston, A.G., Livezey, R.E., 1987. Classification, seasonality and persistence of low-frequency atmospheric circulation patterns. *Mon. Weather Rev.* 115, 1083-1126.
- Brönnimann, S., 2007. Impact of El Niño–southern oscillation on European climate. *Reviews of Geophysics*, 45(3).
- Cai, W., 2006. Antarctic ozone depletion causes an intensification of the Southern Ocean super-gyre circulation. *Geophysical Research Letters*, 33(3), 1–4. <https://doi.org/10.1029/2005GL024911>
- Cai, W., Lengaigne, M., Borlace, S., Collins, M., Cowan, T., McPhaden, M. J., and Ngari, A. 2012. More extreme swings of the South Pacific convergence zone due to greenhouse warming. *Nature*, 488(7411), 365-369.
- Capotondi, A., Wittenberg, A. T., Newman, M., Di Lorenzo, E., Yu, J. Y., Braconnot, P., and Jin, F. F., 2015. Understanding ENSO diversity. *Bulletin of the American Meteorological Society*, 96(6), 921-938.
- Carr, M. E., Strub, P. T., Thomas, A. C., and Blanco, J. L., 2002. Evolution of 1996–1999 La Niña and El Niño conditions off the western coast of South America: a remote sensing perspective. *Journal of Geophysical Research: Oceans*, 107(C12), 29-1.
- Cazenave A, Llovel W. 2010. Contemporary sea level rise. *Annu. Rev. Mar. Sci.* 2:145–73



- Chambers, D. P., Cazenave, A., Champollion, N., Dieng, H., Llovel, W., Forsberg, R., and Wada, Y., 2017. Evaluation of the global mean sea level budget between 1993 and 2014. In *Integrative Study of the Mean Sea Level and Its Components* (pp. 315-333). Springer, Cham.
- Chavez, F. P., Bertrand, A., Guevara-Carrasco, R., Soler, P., and Csirke, J., 2008. The northern Humboldt Current System: Brief history, present status and a view towards the future. *Progress in Oceanography*, 79, 95-105.
- Chen, D., Lian, T., Fu, C., Cane, M. A., Tang, Y., Murtugudde, R., and Zhou, L., 2015. Strong influence of westerly wind bursts on El Niño diversity. *Nature Geoscience*, 8(5), 339-345.
- Chen, L., Li, T., Behera, S. K., and Doi, T., 2016. Distinctive precursory air–sea signals between regular and super El Niños. *Advances in Atmospheric Sciences*, 33(8), 996-1004.
- Church JA y White NJ., 2011. Sea-level rise from the late 19th to the early 21st century. *Surv. Geophys.* 32:585– 602
- Di Lorenzo, E., Schneider, N., Cobb, K.M., Franks, P.J.S., Chhak, K., Miller, A.J., McWilliams, J.C., Bograd, S.J., Arango, H., Curchitser, E., Powell, T.M., Riviere, P., 2008. North Pacific Gyre Oscillation links ocean climate and ecosystem change. *Geophys. Res. Lett.* 35 L08607. doi:10.1029/2007GL032838.
- Enfield, D., Mestas-Nuñez, A., Trimble, P., 2001. The Atlantic Multidecadal Oscillation and its relation to rainfall and river flows in the continental U.S. *Geophys. Res. Lett.* 28, 2077-2080.
- England, M. H., and Huang, F., 2005. On the interannual variability of the Indonesian Throughflow and its linkage with ENSO. *Journal of Climate*, 18(9), 1435-1444.
- Escribano, R., Daneri, G., Farías, L., Gallardo, V. A., González, H. E., Gutiérrez, D., and Braun, M. 2004. Biological and chemical consequences of the 1997–1998 El Niño in the Chilean coastal upwelling system: a synthesis. *Deep Sea Research Part II: Topical Studies in Oceanography*, 51(20-21), 2389-2411.
- Glynn, P. W., and de Weerd, W. H., 1991. Elimination of two reef-building hydrocorals following the 1982–83 El Niño. *Science* 253, 69–71.
- Hamlington, B. D., Cheon, S. H., Thompson, P. R., Merrifield, M. A., Nerem, R. S., Leben, R. R., and Kim, K. Y., 2016. An ongoing shift in Pacific Ocean sea level. *Journal of Geophysical Research: Oceans*, 121(7), 5084-5097.

- Hill, E.A., Hickey, B.M., Shillington, F.A., Strub, P.T., Brink, K.H., Barton, E.D., Thomas, A.C., 1998. Eastern ocean boundaries coastal segment (E). In: Robinson, A.R., Brink, K.H. (Eds.). *The Sea*, 11. John Wiley and Sons, New York, pp. 29–67.
- Hormazabal, S., Shaffer, G., and Leth, O., 2004. Coastal transition zone off Chile. *Journal of Geophysical Research: Oceans*, 109(C1).
- Hsu, Y. C., Lee, C. P., Wang, Y. L., Wu, C. R., and Lui, H. K., 2018. Leading El-Niño SST Oscillations around the Southern South American Continent. *Sustainability*, 10(6), 1783.
- Hu, Z. Z., Kumar, A., Ren, H. L., Wang, H., L’Heureux, M., and Jin, F. F., 2013. Weakened interannual variability in the tropical Pacific Ocean since 2000. *Journal of Climate*, 26(8), 2601-2613.
- Huang, R. X., and B. Qiu, 1998: The structure of the wind-driven circulation in the subtropical South Pacific Ocean. *J. Phys. Oceanogr.*, 28, 1173–1186.
- Huang, R., R. Zhang, and B. Yan, 2001: Dynamical effect of the zonal wind anomalies over the tropical western Pacific on ENSO cycles. *Sci. China*, 44D, 1089–1098, <https://doi.org/10.1007/BF02906865>.
- Hurrell, J. W., Kushnir, Y., Ottersen, G., and Visbeck, M., 2003. An overview of the North Atlantic oscillation. *Geophysical Monograph-American Geophysical Union*, 134, 1-36.
- Imada, Y., Tatebe, H., Watanabe, M., Ishii, M., and Kimoto, M., 2016. South Pacific influence on the termination of El Niño in 2014. *Scientific reports*, 6, 30341.
- Jeong HI, Ahn JB., 2016. A new method to classify ENSO events into Eastern and Central Pacific types. *Int J Climatol* 37(4):2193– 2199. <https://doi.org/10.1002/joc.4813>
- Josey, S.A., Marsh, R., 2005. Surface freshwater flux variability and recent freshening of the North Atlantic in the eastern subpolar gyre. *J. Geophys. Res.* 110 C05008. doi:10.1029/2004JC002521.
- Kao, H. Y., and Yu, J. Y., 2009. Contrasting eastern-Pacific and central-Pacific types of ENSO. *Journal of Climate*, 22(3), 615-632.
- Larkin, N. K., and Harrison, D. E. 2005 a. Global seasonal temperature and precipitation anomalies during El Niño autumn and winter. *Geophysical Research Letters*, 32(16).
- Larkin, N. K., and Harrison, D. E. 2005 b. On the definition of El Niño and associated seasonal average US weather anomalies. *Geophysical Research Letters*, 32(13).

- Leth, O., Shaffer, G., Ulloa, O. 2004. Hydrography of the eastern South Pacific Ocean: results from the Sonne 102 cruise, May–June 1995. *Deep Sea Research Part II: Topical Studies in Oceanography*, 51(20-21), 2349-2369.
- Luther, D. S., Harrison, D. E., and Knox, R. A., 1983. Zonal winds in the central equatorial Pacific and El Niño. *Science*, 222(4621), 327-330.
- Mantua, N. J., and Hare, S. R., 2002. The Pacific decadal oscillation. *Journal of oceanography*, 58(1), 35-44.
- McPhaden, M. J. 1999. Genesis and evolution of the 1997-98 El Niño. *Science*, 283(5404), 950-954.
- McPhaden, M. J., Bahr, F., Du Penhoat, Y., Firing, E., Hayes, S. P., Niiler, P. P., and Toole, J. M., 1992. The response of the western equatorial Pacific Ocean to westerly wind bursts during November 1989 to January 1990. *Journal of Geophysical Research: Oceans*, 97(C9), 14289-14303.
- Meehl, G. A., Karl, T., Easterling, D. R., Changnon, S., Pielke Jr, R., Changnon, D., and Mearns, L. O. 2000. An introduction to trends in extreme weather and climate events: observations, socioeconomic impacts, terrestrial ecological impacts, and model projections. *Bulletin of the American Meteorological Society*, 81(3), 413-416.
- Merrifield, M. A., and Maltrud, M. E. 2011. Regional sea level trends due to a Pacific trade wind intensification. *Geophysical Research Letters*, 38(21).
- Miller, L., Cheney, R. E., and Douglas, B. C., 1988. GEOSAT altimeter observations of Kelvin waves and the 1986-87 El Niño. *Science*, 239(4835), 52-54.
- Montecinos, A., Leth, O., and Pizarro, O., 2007. Wind-driven interdecadal variability in the eastern tropical and South Pacific. *Journal of Geophysical Research: Oceans*, 112(C4).
- Montecinos, A., Purca, S., and Pizarro, O., 2003. Interannual-to-interdecadal sea surface temperature variability along the western coast of South America. *Geophysical Research Letters*, 30(11).
- Mosquera-Vásquez, K., Dewitte, B., and Illig, S., 2014. The Central Pacific El Niño intraseasonal Kelvin wave. *Journal of Geophysical Research: Oceans*, 119(10), 6605-6621.
- Morris, M., Roemmich, D., and Cornuelle, B. 1996. Observations of Variability in the South Pacific. *Journal of Physical Oceanography*.

National Research Council. 1998. Decade-to-Century-Scale Climate Variability and Change: A Science Strategy. Washington, DC: The National Academies Press. <https://doi.org/10.17226/6129>.

Ng, J. Y., Turner, S. W., and Galelli, S., 2017. Influence of El Niño Southern Oscillation on global hydropower production. *Environmental Research Letters*, 12(3), 034010.

OMM, 2018. Guía de prácticas climatológicas. Organización Meteorológica Mundial .

Philander, S. G. H., 1983. Meteorology: Anomalous El Niño of 1982–83. *Nature*, 305(5929), 16-16.

Pizarro, O., Shaffer, G., Dewitte, B., and Ramos, M., 2002. Dynamics of seasonal and interannual variability of the Peru-Chile Undercurrent. *Geophysical Research Letters*, 29(12), 22-1.

Qiu, B., y Chen, S. 2012. Multidecadal sea level and gyre circulation variability in the northwestern tropical Pacific Ocean. *Journal of Physical Oceanography*, 42(1), 193-206.

Ramos, M., Dewitte, B., Pizarro, O., and Garric, G., 2008. Vertical propagation of extratropical Rossby waves during the 1997–1998 El Niño off the west coast of South America in a medium-resolution OGCM simulation. *Journal of Geophysical Research: Oceans*, 113(C8).

Roemmich, D., and Cornuelle, B. 1990. Observing the fluctuations of gyre-scale ocean circulation: A study of the subtropical South Pacific. *Journal of Physical Oceanography*, 20(12), 1919-1934.

Rutllant, J. A., Rosenbluth, B., and Hormazabal, S., 2004. Intraseasonal variability of wind-forced coastal upwelling off central Chile (30 S). *Continental Shelf Research*, 24(7-8), 789-804.

Saji, N.H., Goswami, B.N., Vinayachandran, P.N., Yamagata, T., 1999. A dipole mode in the tropical Indian Ocean. *Nature* 401, 360e363.

Sasaki, Y. N., Minobe, S., Schneider, N., Kagimoto, T., Nonaka, M., and Sasaki, H. 2008. Decadal sea level variability in the South Pacific in a global eddy-resolving ocean model hindcast. *Journal of Physical Oceanography*, 38(8), 1731-1747.

Servain, J., 1991. Simple climatic indices for the tropical Atlantic Ocean and some applications. *Journal of Geophysical Research: Oceans*, 96(C8), 15137-15146.

- Shaffer, G., Hormazabal, S., Pizarro, O., and Salinas, S., 1999. Seasonal and interannual variability of currents and temperature off central Chile. *Journal of Geophysical Research: Oceans*, 104(C12), 29951-29961.
- Schneider, W., Donoso, D., Garcés-Vargas, J., and Escribano, R., 2017. Water-column cooling and sea surface salinity increase in the upwelling region off central-south Chile driven by a poleward displacement of the South Pacific High. *Progress in Oceanography*, 151, 38-48.
- Stammer, D., Cazenave, A., Ponte, R. M., and Tamisiea, M. E., 2011. Causes for Contemporary Regional Sea Level Changes. *Annual Review of Marine Science*, 5(1), 120928130849008. <https://doi.org/10.1146/annurev-marine-121211-172406>
- Stan, C., Straus, D. M., Frederiksen, J. S., Lin, H., Maloney, E. D., and Schumacher, C., 2017. Review of tropical-extratropical teleconnections on intraseasonal time scales. *Reviews of Geophysics*, 55(4), 902-937.
- Strub, P. T., and James, C., 2002. The 1997–1998 oceanic El Niño signal along the southeast and northeast Pacific boundaries an altimetric view. *Progress in Oceanography*, 54(1-4), 439-458.
- Su, J., Zhang, R., Rong, X., Min, Q., and Zhu, C., 2018. Sea surface temperature in the subtropical Pacific boosted the 2015 El Niño and hindered the 2016 La Niña. *Journal of Climate*, 31(2), 877-893.
- Thomas, A. C., Carr, M. E., and Strub, P. T., 2001. Chlorophyll variability in eastern boundary currents. *Geophysical Research Letters*, 28(18), 3421-3424.
- Thompson, D.W.J., Wallace, J.M., 2000. Annular modes in the extratropical circulation. Part I: Month-to-month variability. *J. Clim.* 13, 1000e1016.
- Timmermann, A., An, S. I., Kug, J. S., Jin, F. F., Cai, W., Capotondi, A., and Stein, K. 2018. El Niño–southern oscillation complexity. *Nature*, 559(7715), 535-545.
- Toyama, K., Iwasaki, A., and Suga, T. (2015). Interannual variation of annual subduction rate in the North Pacific estimated from a gridded Argo product. *Journal of Physical Oceanography*, 45(9), 2276-2293.
- Toyama, K., Iwasaki, A., and Suga, T., 2015. Interannual variation of annual subduction rate in the North Pacific estimated from a gridded Argo product. *Journal of Physical Oceanography*, 45(9), 2276-2293.

- Trenberth, K. E. 1997. The definition of El Niño. *Bulletin of the American Meteorological Society*, 78(12), 2771-2778.
- Trenberth, K. E., and Stepaniak, D. P., 2001. Indices of El Niño evolution. *Journal of climate*, 14(8), 1697-1701.
- Trenberth, K. E., Caron, J. M., Stepaniak, D. P., and Worley, S., 2002. Evolution of El Niño–Southern Oscillation and global atmospheric surface temperatures. *Journal of Geophysical Research: Atmospheres*, 107(D8), AAC-5.
- Troup AJ. 1965. The Southern Oscillation. *Quarterly Journal of the Royal Meteorological Society* 91: 490–506.
- Tsuchiya, M., 1982. On the Pacific upper-water circulation. *J. Mar. Res.*, 40, Suppl., 777-799.
- Tsuchiya, M., and L. D. Talley , 1996, Water-property distributions along an eastern Pacific hydrographic section at 135°W, *J. Mar. Res.*, 54, 541–564, doi:10.1357/0022240963213583.
- Visbeck, M., Chassignet, E.P., Curry, R.G., Delworth, T.L., Dickson, R.R., Krahnmann, G., 2003. The ocean's response to North Atlantic Oscillation variability. In: *The North Atlantic Oscillation: Climate significance and environmental impact*. Geophys. Monogr. Ser. 134, 113e146.
- Wang, C., 2002. Atlantic climate variability and its associated atmospheric circulation cells. *Journal of climate*, 15(13), 1516-1536.
- Watanabe, M., Shiogama, H., Tatebe, H., Hayashi, M., Ishii, M., and Kimoto, M., 2014. Contribution of natural decadal variability to global warming acceleration and hiatus. *Nature Climate Change*, 4(10), 893-897.
- Weng H, Behera SK, Yamagata T., 2009. Anomalous winter climate conditions in the Pacific rim during recent El Niño Modoki and El Niño events. *Clim Dyn* 32:663–674
- Wilhite, D. A., Wood, D. A., and Meyer, S. J., 1987. Climate-related impacts in the United States during the 1982-83 El Niño.
- Woods, J. D., and Barkmann, W., 1986. A Lagrangian mixed layer model of Atlantic 18 C water formation. *Nature*, 319(6054), 574-576.
- Wyrski Klaus and Wenzel Jan. 1984. Possible gyre–gyre interaction in the Pacific Ocean. *Nature* (309) 538–540

Wyrтки, K. 1984. The slope of sea level along the equator during the 1982/1983 El Niño. *Journal of Geophysical Research: Oceans*, 89(C6), 10419-10424.

Wyrтки, K., 1967. Equatorial Pacific Ocean1. *Int. J. Oceanol. and Limnol.* Vol, 1(2), 117-147

Wyrтки, K., 1975. El Niño—the dynamic response of the equatorial Pacific Ocean to atmospheric forcing. *Journal of Physical Oceanography*, 5(4), 572-584.

Wyrтки, K., 1985. Water displacements in the Pacific and the genesis of El Niño cycles. *Journal of Geophysical Research: Oceans*, 90(C4), 7129-7132.

Yu, J. Y., Kao, H. Y., and Lee, T., 2010. Subtropics-related interannual sea surface temperature variability in the central equatorial Pacific. *Journal of Climate*, 23(11), 2869-2884.

Zhang, L., and Qu, T., 2014. Low-frequency variability of South Pacific Tropical Water from Argo. *Geophysical Research Letters*, 41(7), 2441-2446.

Zhang, X., and Church, J. A., 2012. Sea level trends, interannual and decadal variability in the Pacific Ocean. *Geophysical Research Letters*, 39(21).

